

# A high-energy ion channeling facility and its applications

**Citation for published version (APA):**

Dijk, van, P. W. L. (1997). *A high-energy ion channeling facility and its applications*. [Phd Thesis 1 (Research TU/e / Graduation TU/e), Applied Physics and Science Education]. Technische Universiteit Eindhoven. <https://doi.org/10.6100/IR476730>

**DOI:**

[10.6100/IR476730](https://doi.org/10.6100/IR476730)

**Document status and date:**

Published: 01/01/1997

**Document Version:**

Publisher's PDF, also known as Version of Record (includes final page, issue and volume numbers)

**Please check the document version of this publication:**

- A submitted manuscript is the version of the article upon submission and before peer-review. There can be important differences between the submitted version and the official published version of record. People interested in the research are advised to contact the author for the final version of the publication, or visit the DOI to the publisher's website.
- The final author version and the galley proof are versions of the publication after peer review.
- The final published version features the final layout of the paper including the volume, issue and page numbers.

[Link to publication](#)

**General rights**

Copyright and moral rights for the publications made accessible in the public portal are retained by the authors and/or other copyright owners and it is a condition of accessing publications that users recognise and abide by the legal requirements associated with these rights.

- Users may download and print one copy of any publication from the public portal for the purpose of private study or research.
- You may not further distribute the material or use it for any profit-making activity or commercial gain
- You may freely distribute the URL identifying the publication in the public portal.

If the publication is distributed under the terms of Article 25fa of the Dutch Copyright Act, indicated by the "Taverne" license above, please follow below link for the End User Agreement:

[www.tue.nl/taverne](http://www.tue.nl/taverne)

**Take down policy**

If you believe that this document breaches copyright please contact us at:

[openaccess@tue.nl](mailto:openaccess@tue.nl)

providing details and we will investigate your claim.

# **A High-Energy Ion Channeling Facility and its Applications**

PROEFSCHRIFT

ter verkrijging van de graad van doctor aan de Technische Universiteit Eindhoven, op gezag van Rector Magnificus, prof.dr. M. Rem, voor een commissie aangewezen door het College van Dekanen in het openbaar te verdedigen op maandag 3 februari 1997 om 16.00 uur

door

**Paulus Wilhelmus Leonardus van Dijk**

geboren te Tilburg

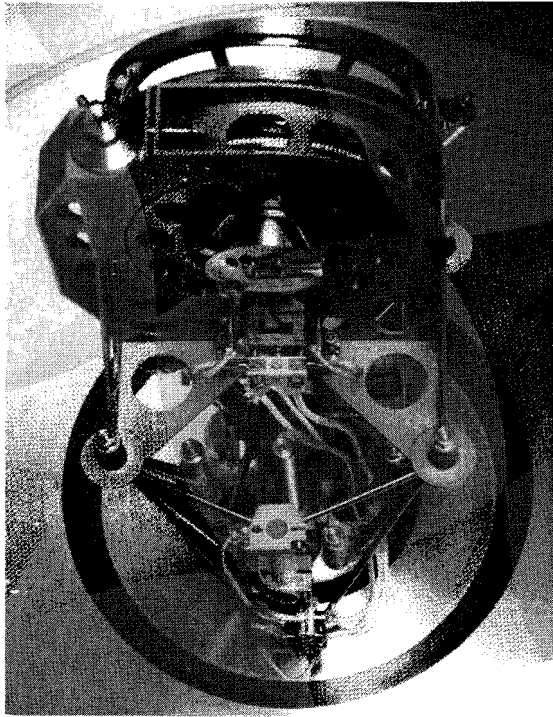
Dit proefschrift is goedgekeurd door de promotoren:

prof.dr. M.J.A. de Voigt  
en  
prof.dr. H.H. Brongersma

Copromotor:  
dr. L.J. van IJendoorn

Druk: Universiteitsdrukkerij TU Eindhoven

A High-Energy Ion Channeling Facility and its Applications /  
Paulus Wilhelmus Leonardus van Dijk. - Eindhoven:  
Eindhoven University of Technology  
Thesis Technische Universiteit Eindhoven. - With ref. -  
With summary in Dutch  
ISBN 90-386-0309-6



*Top view of the 3-axis goniometer, the heart of the high-energy ion channeling facility.*

# Contents

<b>1.</b>	<b>General introduction</b>	<b>1</b>
1.1	History of ion scattering	1
1.2	Development of ion-source and accelerator	2
1.3	Ion scattering experiments	3
1.4	Discovery and interpretation of channeling	4
1.5	Characteristics of channeling with high-energy ions	6
1.6	Outline of this thesis	8
<b>2.</b>	<b>Channeling setup</b>	<b>13</b>
2.1	General description of the setup	13
2.2	Vacuum-system properties	15
2.2.1	Load lock	16
2.2.2	Scattering chamber	17
2.2.3	Beam line	18
2.3	Vacuum control	20
2.4	Data acquisition	21
2.5	Goniometer characteristics	22
2.5.1	Goniometer control unit	24
2.5.2	Goniometer calibration	25
2.5.2.1	Calibration of the rotation axis	26
2.5.2.2	Calibration of the tilt axis	26
2.5.2.3	Calibration of the spin axis	28
2.5.2.4	Calibration of the vertical displacement	30
2.5.3	Hysteresis of goniometer axes	30
2.5.4	Accuracy of the rotation axis	31
2.5.5	Summary	32
2.6	Detector-disk characteristics	33
2.7	Experiments and procedures	34
2.7.1	Absolute dose calibration	36
2.8	Conclusions	38
<b>3.</b>	<b>Ion scattering and channeling experiments</b>	<b>41</b>
3.1	Monitoring of spectra and normalized angular scans	42
3.2	Incident-ion energy and angular-scan width	44
3.2.1	Simulation of angular scans	45
3.2.2	Angular-scan measurement	48
3.3	Conclusions	51

<b>4.</b>	<b>Strain in Si<sub>1-x</sub>Ge<sub>x</sub>/Si heterostructures measured with high-energy ion channeling</b>	<b>53</b>
4.1	Introduction	54
4.2	Coherency strain in commensurately grown thin films	56
4.3	Requirements for the analysis of SiGe thin films with high-energy ions	60
4.4	Coherency strain in a hetero-epitaxial Si <sub>1-x</sub> Ge <sub>x</sub> (x=0.05) top layer grown on silicon (100)	64
4.5	Coherency strain in a hetero-epitaxial Si <sub>1-x</sub> Ge <sub>x</sub> (x=0.25) buried layer	66
4.6	Coherency strain in a hetero-epitaxial Si <sub>1-x</sub> Ge <sub>x</sub> (x=0.175) buried layer	68
4.7	Angular-scan simulations with Monte Carlo trajectory calculations	70
4.8	Beam-induced strain relaxation	73
4.9	Conclusions	74
<b>5.</b>	<b>Applications of high-energy ion channeling</b>	<b>77</b>
5.1	Theory of defect analysis	78
5.2	Defect depth profiling of a 4 micron Si <sub>1-x</sub> Ge <sub>x</sub> multi-layered structure	79
5.2.1	Experimental details	81
5.2.2	Quantification of defect density	83
5.2.3	Discussion	85
5.2.4	Summary and conclusions	85
5.3	Characterisation of Si <sub>1-x-y</sub> Ge <sub>x</sub> C <sub>y</sub> strained layers	86
5.3.1	Applications of the characterized structures in electronic devices	87
5.3.2	Experimental details for characterization of Si <sub>1-x-y</sub> Ge <sub>x</sub> C <sub>y</sub> structures	88
5.3.3	Characterization of composition and sample structure	89
5.3.4	Strain analysis of Si <sub>1-x-y</sub> Ge <sub>x</sub> C <sub>y</sub> samples without a capping layer	95
5.3.5	Strain analysis of Si <sub>1-x-y</sub> Ge <sub>x</sub> C <sub>y</sub> samples with a silicon capping layer	97
5.3.6	Summary and conclusions	99
5.4	Defect analysis of plasma etched GaAs/Al <sub>y</sub> Ga <sub>1-y</sub> As/In <sub>x</sub> Ga <sub>1-x</sub> As/GaAs hetero-structures	101
5.4.1	Characteristics of the heterostructure and applications in electronic devices	102
5.4.2	Experimental details	
5.4.3	Measurements on GaAs/Al <sub>0.25</sub> Ga <sub>0.75</sub> As/In <sub>0.15</sub> Ga <sub>0.85</sub> As/GaAs with RBS and channeling	105
5.4.4	Conclusions	108
5.5	Summary and conclusions	109

<b>6.</b>	<b>Analysis of InP with Channeling Nuclear Reaction Analysis; Vibrational amplitudes of In and P</b>	<b>113</b>
6.1	Introduction	114
6.2	Experimental details	117
6.3	Results	118
6.4	Minimum yield and critical angle for a diatomic lattice	121
6.5	LAROSE modifications	123
6.6	Angular scan properties obtained from LAROSE trajectory simulations	124
6.7	Conclusions	127
<b>7.</b>	<b>Stopping power of channeled He ions</b>	<b>131</b>
7.1	Introduction	131
7.2	Energy loss in theoretical scope	135
7.3	Ion-trajectory simulations	137
7.4	Target preparation and sample thickness	142
7.5	Energy distribution of channeled ions measured in transmission	143
7.6	Angular dependence of energy-loss components	146
7.7	Conclusions	149
	<b>Publications</b>	<b>152</b>
	<b>Summary</b>	<b>153</b>
	<b>Samenvatting</b>	<b>155</b>
	<b>Dankwoord</b>	<b>158</b>
	<b>Curriculum Vitae</b>	<b>160</b>

# 1

## General introduction

*This chapter contains a brief introduction to ion-beam-analysis techniques (IBA) and some of their applications. The scope of this thesis is the applicability of high-energy (3-30 MeV) ions for scattering techniques in combination with ion channeling. A brief overview of the early history of ion scattering, development of the charged-particle accelerators and application of the technique in materials analysis will be presented. Subsequently an outline of the contents of this thesis will be summarized that involves the realisation of a new experimental setup and various analytical results of applications of high-energy ion channeling in materials analysis.*

### 1.1 History of ion scattering

The history of ion scattering starts in the beginning of this century. The framework of alpha scattering was set by Geiger and Marsden (1911-1913) [1]. They built an apparatus to test and confirm the model of an atom as conceived by Ernest Rutherford in 1911. In their experiment a beam of monoenergetic and collimated alpha particles from a natural source impinged perpendicularly on a 2  $\mu\text{m}$  thick metal foil. Almost all of the incident particles reappeared at the far side of the target with only slightly altered direction. Only few alpha particles did undergo large changes in energy and direction which were attributed to close encounters of the incident particles with the nucleus of a single target atom. Rutherford derived the differential scattering cross-section assuming that Coulomb interaction was responsible for the classical collision between the alpha particles and the atomic nucleus and was able to explain the angular dependence of the scattering intensity. The energy of the scattered alpha particle could be derived from conservation laws of energy and momentum of the projectile and of the target nucleus. The classical nature of the collisions implied that a measurement of the energy of the scattered ions at a given backscattering angle allowed identification of the mass of the atomic nuclei in the target. A new analytical technique *Rutherford Backscattering Spectrometry* (RBS) was born.



Only during the last four decades ion-scattering has developed as a valuable technique for materials analysis. A large contribution to the success was the development of accelerators (section 1.2) that produced well-defined and mono-energetic ion beams. The advantage of an accelerator over the natural source-and-diaphragm apparatus is that higher particle fluxes can be obtained and that beam parameters can be varied over a wider range. The rapid evolution of MeV ion beams into powerful probes for surface and near-surface analysis can be traced to three major events that occurred roughly 35 years ago: namely the appearance of the solid-state detector around 1960, the discovery of channeling in 1962-1963 and the industrial application of ion implantation to semi conductors, starting around 1965. The first widely publicized application of RBS was the in-situ analysis of the lunar soil, carried out as part of the scientific mission of Surveyor V after its soft landing on the moon on September 9, 1967. Six  $^{242}\text{Cm}$  alpha sources that emit alpha particles of 6.1 MeV were used for the measurements.

Pioneers of the early days of ion beam analysis (IBA) that contributed to the primal developments in the field have presented their personal reminiscences of these events during the 10th conference on IBA held in Eindhoven [2] in an attempt to record some of the excitement they experienced in witnessing the 'birth' of a new analytical tool. A handbook on ion beam analysis recommended for detailed study which describes ion beam analysis in great detail is *Backscattering Spectrometry* by Chu et al. [3].

## 1.2 Development of ion-sources and accelerators

The most important aspect of the technology of electrostatic accelerators consists in establishing and maintaining a high-voltage to accelerate the charged particles from the ion source. The earliest development of this type of accelerator stems from Cockroft and Walton in 1932, who built a device that was eventually to reach a potential of 800 kV [4]. The most common type of electrostatic accelerator in use today in nuclear physics laboratories is based on the Van de Graaff generator (1934) which provides various kinds of ions and energies. Charge is sprayed at low potential on an isolated charge-transmitting belt, which conveys it to an upper electrode. Enclosing the components in high-pressure ( $\sim 7$  atm.) inert gas ( $\text{SF}_6$ ) enables MV's to be sustained at the upper electrode where the particle source is located. The Van de Graaff

### *General introduction*

accelerator became the workhorse of low-energy nuclear physics in the 1960s and several dozen facilities have been constructed at U.S. universities and research laboratories. The successor of this machine was the *tandem* Van de Graaff accelerator [5]. A beam of negative ions is accelerated from ground potential toward the high-voltage terminal in the centre of the pressure tank. There they enter a foil or gas stripper which removes  $n+1$  electrons, resulting in an ion carrying a net positive charge of  $ne$ . As the ion exits the accelerator it is not necessarily fully stripped ( $n \leq Z_2$ ). The ion energy is the product of  $(n+1)$  and the terminal voltage.

An alternative to the linear electrostatic accelerators is the cyclotron in which the beam makes many cycles. The ions receive a small voltage (energy) increment in each, near circular, orbit until they reach the MeV range. The first practical cyclotron for accelerating particles has been built by Lawrence and Livingston at Berkely in 1931 [6]. The concept of the cyclotron allows to increase the ion energy further since it avoids the need of a high-voltage terminal. The Eindhoven Azimuthally Varying Field (AVF) cyclotron has been built in 1963 at the Philips Research Laboratories and was designed to accelerate protons or alpha particles up to energies between 3 MeV and 30 MeV. In 1968 the cyclotron was moved to the Eindhoven University of Technology and it has been operational for nuclear physics, for analytical purposes and for the production of radio isotopes. Due to the relatively limited brightness and a typical energy spread of 0.2% of the ion beam, a cyclotron is not common used in ion-scattering experiments. The advantage of the use of a cyclotron, the production of low  $Z_2$  ions with relatively high energy (3-30 MeV), has been used to demonstrate that application of this type of accelerator is profitable for ion-scattering experiments as will be reported in this thesis.

### **1.3 Ion scattering experiments**

Analytical techniques that use ion beams can be distinguished by the ion energy. Our experiments are carried out using alpha particles or protons with energies of 3-30 MeV. In this energy region three typical groups of analytical techniques can be indicated. The first group concerns energy spectrometry, that consists of techniques in which the energy of the scattered particle (RBS or Nuclear Reaction Analysis) or induced photon is measured (Proton Induced X-ray Emission, Proton Induced Gamma Emission). Energy resolved spectra are obtained that give

information on the elemental composition of the target in the bulk and in the near-surface region. Of these techniques RBS and NRA provide depth resolution while PIXE (typical ppm) and PIGE are specifically suited for trace elements analysis. The second group involves mass-dispersive ion beam techniques based on Elastic Recoil Detection Analysis (ERD or ERDA). Several mass discrimination techniques can be used to characterise elemental or isotopical composition in the near-surface region up to a depth of several microns. The third group contains angular-dispersive ion beam experiments such as channeling and blocking that provide target characteristics such as crystallographic orientation and crystalline quality. The channeling and blocking technique is of general validity and can be applied in combination with all techniques mentioned above. This thesis focuses on the use of RBS in combination with ion channeling and exploits the advantages of the use of high-energy He ions (3-30 MeV) in materials analysis. Developments and improvements of the new experimental facility at the EUT will be extensively discussed.

#### **1.4 Discovery and interpretation of channeling**

Channeling is now known to exist for all positive particles (from positrons and protons to uranium ions) extending from 100 eV to over 400 GeV. In the year 1910 Bragg [7] initially interpreted von Laue's diffraction spots as "kanalizierung" of X-ray corpuscles through the open channels of the crystal lattice. Stark published a paper in 1912 [8] and predicted that similar channeling effects would also occur with proton beams. In those years these suggestions were overshadowed by the prevailing interest in the new and powerful technique then becoming available with X-ray diffraction (XRD). Bragg recognized the wave nature of X-rays and formulated his diffraction law. Obsessed by the particle-wave duality the interpretation of many interactions has been attempted to understand with the wave-like behaviour of the probing projectiles (photons, electrons and even neutrons). However, since the wavelength of a 2 MeV He<sup>+</sup> ion is only  $\sim 10^{-4}$  Å, diffraction effects will be negligible in a crystal where the atomic spacing is typically several Ångstroms. For this reason ion-scattering processes can be treated as classical collisions.

Ion channeling in crystals can be treated as a long-range steering mechanism. The incident ions experience the Coulomb repulsion of the nuclei in the atomic strings and are deflected over small

### *General introduction*

angles away from the atomic strings towards the centre of the channel. In 1957 Bredov [9] observed that 4 keV radioactive  $^{137}\text{Cs}$  had an anomalously long range when injected into crystalline germanium. The experiments were repeated in 1962 by Davies et al. [10] who used amorphous germanium films but a far smaller range of the ions was observed. Only three years later, Davies and coworkers reported anomalously long ranges for heavy ions slowed down in polycrystalline aluminum and tungsten targets (and eventually silicon), observing ranges ten times longer than the mean range [11]. In 1963 Robinson and Oen [12] proposed that the observed tail be attributed to some sort of Coulomb-like steering process, occurring in those polycrystalline grains which by chance had a major axis aligned with the incident beam direction. These results played the key role in the (accidental) discovery of ion channeling. Much of the basic theory of the channeling process can be found in the treatment published by Lindhard in 1965 in his Notes on Atomic Collisions [13] where he makes a careful distinction between violent collision processes resulting in large angle scattering or a nuclear reaction and collisions with electrons that contribute to the energy loss of the ions. These notes became well known as the Lindhard continuum theory of channeling in which deflection of an atomic string is described with a continuum potential associated with the string of atoms. The incident ions will channel in a main axial or planar direction when they enter the crystal within the critical angle for channeling  $\Psi_c$ . Lindhard's theory correlates the critical angle  $\Psi_c$  for planar and axial directions to the characteristic angle  $\Psi_1 = (Z_1 Z_2 e^2 / Ed)^{1/2}$ , where  $Z_1$  and  $Z_2$  are the atomic numbers of incident ion and target atom, respectively,  $E$  the energy of the incident ion and  $d$  the atomic spacing along the atomic string. This implies that the critical angle decreases for ions with higher energy, that will be utilized fully in this work.

Apart from analytical treatments of the channeling theory the use of Monte-Carlo simulations for the study of ion-atom interactions has now become common practice. Already in 1963 Robinson and Oen developed a Monte-Carlo computer code and performed calculations on the slowing down of 1-10 keV Cu atoms in various crystals. They found abnormally large penetrations for those ions with initial directions coinciding closely with those of the principal axes. In 1967 Morgan and Van Vliet [14] evaluated the critical angle for axial and planar channeling and the distance of closest approach for Cu atoms in the energy range 5-500 keV

entering a perfect crystal. They observed that the values obtained from their MC calculations compare well with the predictions of the continuum model as developed by Lindhard. In 1971 Barrett developed the MC program LAROSE [15] which provided detailed information on the flux distribution of the channeled ions in the crystal and the close-encounter probability which can be related to the probability for a large-angle scattering event or nuclear reaction. Barrett compared the calculated values for the minimum yield for axial channels with experimental data of Davies [16] and found an analytical expression for the minimum yield. A description of these results is given in section 6.1 where this theory is used for the interpretation of angular scans obtained from an InP crystal. We modified Barrett's program and incorporated calculation of the ion energy loss in the program (chapter 7). Comparable MC programs have been developed by Smulders and Boerma [17], Dygo and Turos [18] and Murthy and Srinivasan [19]. Some of these programs incorporate a detailed energy-loss model that enables the study of the anomalously low energy loss of channeled ions.

### 1.5 Characteristics of channeling with high-energy ions

The channeling effect can occur when a well-collimated beam of particles is incident upon a monocrystalline target mounted on a goniometer. Channeling measurements usually determine the yield of a close-encounter processes (such as large angle scattering, nuclear reaction or excitation) as a function of the angle  $\Psi$  of the beam with respect to some axial or planar direction in the crystal. The typical orientation dependence of the yield of a close-encounter process measured in a channeling experiment is the so-called angular scan. The scan-width observed in the experiment ( $\Psi_{1/2}$ ) is closely related to the critical angle for channeling as defined by Lindhard. Picraux and coworkers [20] measured the critical angle for a variety of atomic systems and for a broad energy range. They confirmed the energy dependence of the critical angle i.e.  $\Psi_c \sim E^{-1/2}$ . The energy dependence of the critical angle promises an increased angular resolution in lattice-deformation studies where the tetragonal distortion of a strained layer is measured from the shift of a non-normal crystalline axis of this strained layer with respect to the position of the corresponding crystalline axis of the substrate.

A second application of the channeling technique is the determination of crystal damage or

### *General introduction*

disorder from channeling-RBS measurements. The spectrum obtained after alignment of the beam with a crystallographic direction is compared with the spectrum obtained from a random (non-channeled) orientation. The measured normalized backscattering yield  $\chi$ , the ratio of the observed channeled yield to the random yield, can be compared to the ratio of a defect-free crystal. Subsequently the disorder in the crystal can be quantified. The RBS channeling technique is used in this way to analyse implantation profiles, implantation induced disorder and to monitor effects of anneal treatments and recrystallisation [21][22]. The profitability of the use of high-energy ions in damage depth profiling is that a larger depth interval can be analysed, apart from the improved angular resolution.

A third class of experiments involves transmission through thin targets and the analysis of the energy distribution of the transmitted ions. This can be done directly, with the detector in a 'bright field' directly placed behind the target, or indirectly 'dark field' [23][24]. In the latter case the energy distribution of the ions that scattered from (deposited) atoms at the reverse side of the sample is monitored. These types of transmission experiments can provide information of the surface location of atoms when an orientation-dependent scan is measured [25][26][27][28].

The availability of high-energy ions in RBS-channeling and ERD is profitable to enhance the sensitivity of the detection of light elements (C,N,O) when the beam energy is near a resonance in the scattering cross-section and can be applied in NRA and Charged Particle Activation Analysis (CPAA) when the beam energy is near a resonance in the reaction cross-section. Quantification of the measurements requires the availability of reliable scattering and reaction-cross-section data. A compilation of nuclear-reaction data, originally collected by R.A. Jarjis, has come available in the recently published Handbook of Modern Ion Beam Materials Analysis [29]. However, since the cross-sections highly depend on ion energy and detection angle additional measurement of the cross-sections are necessary. Recent applications use resonant scattering cross sections for oxygen and carbon depth profiling with 3.05 MeV [30][31][32] and 4.28 MeV  $^4\text{He}^{++}$  ions [33][34], respectively. An example of nitrogen depth profiling using the nuclear reaction  $^{14}\text{N}(\alpha,p)^{17}\text{O}$  at 3.9 MeV is given by McIntyre Jr. [35]. Applications of resonant ERDA for carbon and oxygen depth-profiling with high-energy 12.6 and 13.6 MeV  $^4\text{He}^{++}$ RBS

have earlier been reported by Rijken [36][37][38], and by Van IJzendoorn [39] and Maas [40][41]. Due to the decreasing stopping power of  $\text{He}^{++}$  ions with energies above the stopping-power maximum ( $\sim 2\text{MeV}$ ) depth resolution is limited unless recoil detection is exploited, thereby profiting from the enhanced stopping power of the heavy recoil. Reviews of existing channeling theory, experiments, and applications are published in several review articles [42][43][44][45] and proceedings of several conferences on channeling, ion-beam analysis and ion-beam modifications. A handbook for channeling is *Materials analysis by ion channeling* by Feldman Mayer and Picraux [46].

## 1.6 Outline of this thesis

The analytical facility at the Eindhoven cyclotron research laboratory encompasses four experimental stations: a micro-beam facility, a PIXE chamber, a recoil-detection station and the new UHV channeling facility. A detailed description on the realisation of the channeling facility is presented in chapter 2 of this thesis. The setup has been build to develop analytical techniques that profit from the use of relatively high-energy (3-30 MeV) ions. The setup contains a 3-axis goniometer with superior accuracy ( $\sim 0.001^\circ$ ) and large flexibility in the choice of detection geometry. The design of the goniometer and scattering chamber enable transmission experiments, backscattering experiments and ion-scattering experiments that require two independent movable detectors (such as used in coincidence techniques).

Chapter 3 presents the first results with the new setup proving the feasibility of the concept. Silicon  $\langle 100 \rangle$  angular scans have been measured in an RBS experiment using 4 MeV, 12.6 MeV and 25 MeV He ions. Furthermore details on the monitoring and off-line analysis program COLUMBUS will be presented to illustrate the data-acquisition facility.

The main advantage of ion channeling with high-energy ions is the decrease of the critical angle for channeling. It will be demonstrated in chapter 4 that strain analysis of  $\text{Si}_{1-x}\text{Ge}_x$  single-layer heterostructures can be carried out extremely accurately using 12.6 MeV  $\text{He}^{++}$  ions. A variety of samples has been analysed with typical Ge fractions between 0.05 and 0.25. Furthermore the influence of a Si capping layer on the interpretation of the angular scans, obtained from the

### *General introduction*

buried  $\text{Si}_{1-x}\text{Ge}_x$  layer will be discussed. A close resemblance of the measured angular scans is obtained using Monte Carlo trajectory calculations. It is shown that these simulations are very helpful for a correct interpretation of the measured scans since they incorporate steering effects of ions at the interfaces of adjacent layers.

High-energy He ions allow profiling of larger depth ranges in defect depth studies. Measurement of the normalized yield  $\chi$  of a 4  $\mu\text{m}$  thick  $\text{Si}_{1-x}\text{Ge}_x$  relaxed multi-layer will be demonstrated in chapter 5. The normalized yield  $\chi$  has been determined as a function of depth and the amount of disorder in the structure has been determined. The depth dependence of this property will be used to quantify crystal damage in  $\text{Si}_{1-x}\text{Ge}_x$ -based structures. To broaden the application of high-energy ion channeling to a variety of targets, analysis of  $\text{Si}_{1-x-y}\text{Ge}_x\text{C}_y$  and  $\text{In}_x\text{Ga}_{1-x}\text{As}$  heterostructures will be presented in chapter 5. Characterisation of these structures involves both defect density and strain analysis.

In chapter 6 a detailed study will be presented on the use of NRA- and RBS-channeling for the determination of the vibrational amplitude of In and P atoms in a diatomic InP crystal. The phosphorus signal was obtained from detected protons, created by the exothermal  $^{31}\text{P}(\alpha, \text{p})^{34}\text{S}$  nuclear reaction. The yield of elastically scattered alpha particles from the indium target atoms serve as a probe for those atoms. Resulting vibrational amplitudes of the individual atoms are obtained from a combination of  $\langle 110 \rangle$  and  $\langle 111 \rangle$  angular-scan measurements and Monte-Carlo trajectory calculations.

In chapter 7 a study will be presented on the energy loss of 4 MeV He ions in a silicon crystal at channeling conditions. In case the crystal is sufficiently thin, the incident beam will be transmitted and ions will only have lost part of their energy. For the transmitted particles the energy distribution is strongly dependent on the crystallographic orientation with respect to the incident ion beam. The energy loss of the 4 MeV He ions has been subject of study in both Monte-Carlo simulations and transmission experiments. With the introduction of the spatial valence-electron-density distribution in Monte-Carlo trajectory calculations we are able to obtain average stopping-power differences in the axial  $\langle 111 \rangle$ ,  $\langle 110 \rangle$  and  $\langle 100 \rangle$  directions for sample



thicknesses of several hundreds of nanometres. Transmission-channeling experiments have been carried out to measure energy distributions of transmitted ions for many different orientations resulting in angular scans which reveal the orientation dependence of the ion stopping. Energy-loss distributions for planar channeled, axial channeled and non-channeled ions are identified and qualitatively compared with the simulations.

## References

1. H. Geiger and E. Marsden, *Phil. Mag.* 25 (1913) 606.
2. J.A. Davies, G. Amsel and J.W. Mayer, *Nucl. Instr. and Meth.* B64 (1992) 12.
3. W.K. Chu, J.W. Mayer, M.A. Nicolet, *Backscattering Spectrometry*, Academic Press inc. London Ltd. (1978).
4. J.B.A. England, *Techniques in Nuclear Structure Physics*, Wiley and sons, New York (1974).
5. R.J. Van de Graaff, *Nucl. Instr. and Meth.* 8 (1960) 195.
6. M.S. Livingston, review article: 'Early History of Particle Accelerators', *Adv. Electron. Electron Phys.* 50 (1980) 1.
7. W.H. Bragg, *Philos. Mag.* 20 (1910) 38.
8. J. Stark, *Z. Phys.* 13 (1912) 973.
9. M.M. Bredov and I.M. Okuneva, *Sov. Phys. Dok.* 113 (1957) 795.
10. J.A. Davies, J.D. McIntyre and G.A. Sims, *Can. J. Chem.* 40 (1962) 1605.
11. G.R. Piercy, F. Brown, J.A. Davies and M. McCargo, *Phys. Rev. Lett.* 10 (1963) 399.
12. M.T. Robinson and O.S. Oen, *Phys. Rev.* 132 (1963) 2385.
13. J. Lindhard, *K. Dan. Vidensk. Selsk. Mat.-Fys. Medd.* 34 No. 14 (1965).
14. D.V. Morgan and D. Van Vliet, *Can. J. Phys.* 46 (1968) 503.
15. J.H. Barrett, *Phys. Rev.* B3 (1971) 1527.
16. J.A. Davies, J. Denhartog and J.L. Whitton, *Phys. Rev.* 161 (1967) 345.
17. P.J.M. Smulders and D.O. Boerma, *Nucl. Instr. and Meth.* B29 (1987) 471.
18. A. Dygo and A. Tuross, *Phys. Lett.* A127 (1988) 281.

*General introduction*

19. C.S. Murthy and G.R. Srinivasan, Phys. Rev. B 47 (1993) 1256.
20. S.T. Picraux, J.A. Davies, L. Eriksson, N.G.E. Johansson and J.W. Mayer, Phys. Rev. 180 (1969) 873.
21. J.W. Mayer, L. Eriksson, S.T. Picraux and J.A. Davies, Can. J. Phys. 46 (1968) 663.
22. E. Bøgh, Can J. Phys. 46 (1968) 653.
23. B.R. Appleton, C. Erginsoy and W.M. Gibson, Phys.Rev. 161 (1967) 330.
24. M.A. Boshart, A. Dygo and L.E. Seiberling, Phys. Rev. A 51 (1995) 2637.
25. L.C. Feldman P.J. Silverman, J.S. Williams, T.E. Jackman and I. Stensgaard, Phys Rev. Lett. 41 (1978) 1396.
26. I. Stensgaard, Nucl. Instr. and Meth. B 15 (1986) 300.
27. W.R. Wampler, Phys. Rev. B 51 (1995) 4998.
28. M.A. Boshart, A.A. Bailes III, A. Dygo and L.E. Seiberling, J. Vac. Sci. Technol. A 13 (1995) 2764.
29. J.R. Tesmer and M. Nastasi, *Handbook of Modern Ion Beam Materials Analysis*, Materials Research Society, Pittsburg, USA. (1995).
30. B. Blainpain, P. Revesz, L.R. Doolittle, K.H. Purser and J.W. Mayer, Nucl. Instr. and Meth. B 34 (1988) 459.
31. W. de Coster, B. Brijs, R. Moons and W. Vandervorst, Nucl. Instr. and Meth. B66 (1992) 283.
32. G. Vizkelethy, P. Revesz, J. Li, L.J. Matienzo, F. Emmi and J.W. Mayer (1990) in "*High Energy and Heavy Ion Beams in Materials Analysis*" J.R. Tesmer, C.J. Maggiore, M. Nastasi, J.C. Barbour and J.W. Mayer, eds. p 235, Materials Research Society, Pittsburg, Pennsylvania.
33. M. Ostling, C.S. Peterson, and G. Possnert, Nucl. Instr. and Meth. 218 (1983) 439.
34. P. Revesz, J. Li, Gy. Vizkelethy, J.W. Mayer, L.J. Matienzo and F. Emmi, Nucl. Instr. and Meth. B58, (1991) 132.
35. Z. Lin, L.C. McIntyre Jr., J.A. Leavitt, M.D. Asbaugh and R.P. Cox, Nucl. Instr. and Meth. B 79 (1993) 498.
36. H.A. Rijken, S.S. Klein, and M.J.A. de Voigt, Nucl. Instr. and Meth. B64 (1992) 395.

37. H.A. Rijken, S.S. Klein, L.J. van IJzendoorn and M.J.A. de Voigt, Nucl. Instr. and Meth. B 79 (1993) 532.
38. H.A. Rijken, PhD thesis, Eindhoven University of Technology, Eindhoven, The Netherlands (1993).
39. L.J. van IJzendoorn, J.W. Niemantsverdriet, R.J. Severens, P.W.L. van Dijk and M.J.A. de Voigt, Nucl. Instr. and Meth. B 89 (1994) 114.
40. A.J.H. Maas, S.S. Klein F.P. Rademakers, A.W.E. Minnaert and M.J.A de Voigt, IBA 12 Conference proceedings Nucl. Instr. and Meth. B 118 (1996) 588.
41. A.J.H. Maas, S.S. Klein, D.P.L. Simons, M.J.A. de Voigt, IBA 12 Conference proceedings Nucl. Instr. and Meth. B 118 (1996) 268.
42. A.F. Tulinov, Usp. Fiz. Nauk 87 (1965) 585; Sov. Phys. Usp. 8 (1965) 864.
43. S. Datz, C. Erginsoy, G. Liebfried and H.O. Lutz, Ann. Rev. Nucl. Sci. 17 (1967) 129.
44. M.W. Thompson, Contemp. Phys. 9 (1968) 375.
45. D.S. Gemmell, Rev. of Mod. Phys. 46 (1974) 129.
46. L.C. Feldman, J.W. Mayer and S.T. Picraux, *Materials Analysis by Ion Channeling*, Academic Press inc. London ltd. (1982).

# 2

## Channeling setup

*A detailed description of the new channeling setup is presented in this chapter. This setup has been built to accomplish ion scattering experiments combined with ion channeling. In section 2.1 the general design criteria for the scattering chamber will be discussed. The vacuum requirements for this UHV system are treated in section 2.2. A description of the vacuum controls is given in section 2.3. The experiments are carried out using the PhyDAS data acquisition system as described in section 2.4. A detailed description of the goniometer steering, its calibration, accuracy and hysteresis are covered in section 2.5. Details on the detector displacement are presented in section 2.6. Finally, experiments are described that have been carried out for absolute dose calibration. In this perspective two different methods of the measurement of the beam current are discussed. Section 2.8 will summarize the results presented in this chapter.*

### 2.1 General description of the setup

A scattering chamber has been designed to explore Rutherford Backscattering Spectrometry and channeling experiments using high energy (3-30 MeV) protons and He ions from the Eindhoven AVF cyclotron. The combination of the channeling technique and high energy ions is the key to a high angular resolution in materials analysis thanks to the reduction of the characteristic angle for channeling at increased energies. Therefore, these experiments require a high precision goniometer for proper target alignment. For this purpose a goniometer was designed and constructed at the Eindhoven University of Technology. This goniometer has three axes of rotation and three of translation. In order to utilize RBS, ERDA and transmission experiments a high flexibility concerning detector position had to be obtained. Therefore, two independent stepper-motor controlled detector disks are available in the scattering chamber. Detectors mounted on these disks can be positioned at a chosen scattering angle in the horizontal scattering plane (section 2.6).

RBS-channeling analysis requires an ion beam with an angular spread small compared to the characteristic angle for channeling  $\Psi_1$ . Using high energy (3-30 MeV) particles the characteristic angle for channeling will be a tenth to several tenths of a degree i.e:  $\Psi_1=0.09^\circ$  for 30 MeV protons in  $\langle 100 \rangle$  Si. To obtain a beam with small angular spread the beam line is equipped with two sets of collimator slits, 7.68 m apart. Neither focussing nor bending elements are placed between the two slit sets. Each individual set of slits consists of horizontal and vertical adjustable jaws, mounted on a micrometer. The distance between the jaws is adjustable in the range of 0-20 mm. Each set of slits results in a rectangular shaped diaphragm. The use of these slit sets allows a good definition of the position of the beam and limits the angular spread (beam divergence) of the ions incident on the sample to typical value of  $0.08^\circ$ . This results in a well-defined parallel beam which is indispensable for channeling experiments.

The beam line is equipped with a rotating vane used for dose calibration in the experiments. This

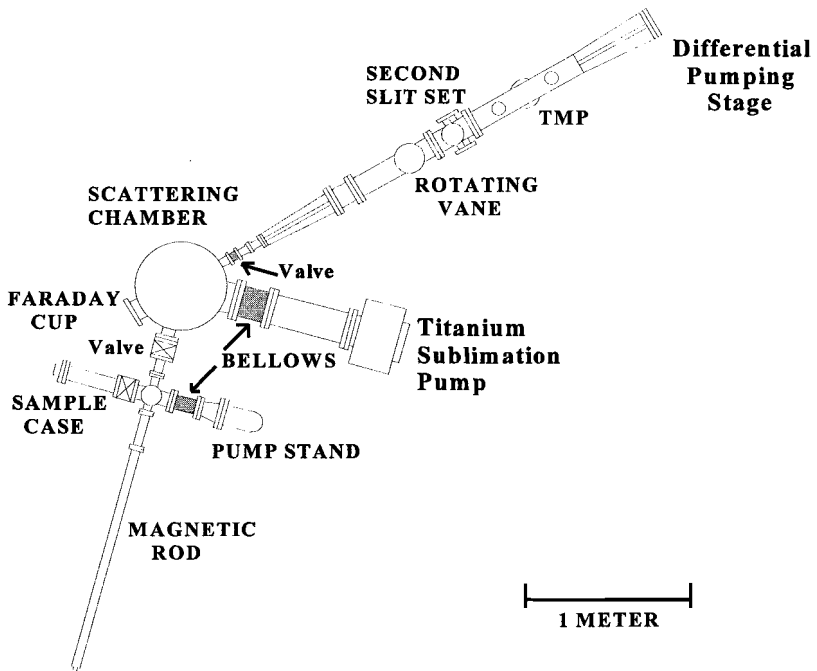


**Figure 2.1:** Top view of the scattering chamber, beam line and load lock. The magnetic rod, necessary for sample transfer, is indicated in the figure.

### *Channeling setup*

rotating vane is located between the second slit set and the scattering chamber.

The scattering chamber operates at Ultra High Vacuum (UHV) conditions. The requirements needed to achieve this determine the choices of vacuum pumps, the design of the chamber and the choices of material used for construction (section 2.2). A small chamber, further referred to as load lock, is connected to the scattering chamber. The load lock is used for sample transfer and enables the exchange of samples in the goniometer head without the need of venting the UHV scattering chamber. A small case containing up to five samples is mounted to the load lock to enable multiple sample changes without venting the load lock. Sample transport from the load lock to the scattering chamber is accomplished with a magnetic rod.

Figure 2.1 shows the top view of the scattering chamber, beam line, load lock and the sample case. The different sections are separated by vacuum valves and can be evacuated independently. A multi-sector Faraday cup is used to indicate the position of the incident beam and to measure the beam current. The propagation of high-frequency vibrations towards the scattering chamber and the sensitive goniometer head is suppressed by the use of bellows between the different sections. Additional bellows are applied to separate the pump stands from the beam line, scattering chamber and the load lock to suppress the propagation of vibrations from the turbomolecular pumps and the rotary vane pumps.

## **2.2 Vacuum-system properties**

The base pressure in a vacuum system depends on the effective pump speed, the gas flow into the section and the outgassing rate of the walls and material present in the system. The design of a UHV system requires the use of materials with a small outgassing coefficient. Materials with a smooth surface that can be cleaned, polished and baked out are preferred. Regarding these requirements the components of the beam line, scattering chamber and load lock are made out of stainless steel. This material has a typical outgassing coefficient between  $10^{-8}$  and  $10^{-7}$  mbar  $\text{ls}^{-1}\text{cm}^{-2}$  when degreased and polished. Cleaning the components with trichloroethylene or alcohol and subsequent baking out for a long time further decreases the coefficient ultimately down to  $10^{-12}$  mbar  $\text{ls}^{-1}\text{cm}^{-2}$  [1]. Gaseous nitrogen is used for venting of the vacuum system to reduce moisture and water vapour on inner surfaces of the components which would deteriorate the

vacuum. The base pressure in the section can be calculated by multiplication of the outgassing coefficient with the total area (cm<sup>2</sup>) in the vacuum divided by the effective pumping speed (ls<sup>-1</sup>). The effective pumping speed,  $S_{\text{eff}}$  is calculated using the pumping speed of the pump,  $S$ , and the conductance,  $C$ , of the connecting part between the pump and the system using the equation:

$$S_{\text{eff}} = \frac{SC}{S+C} \quad 2.1$$

The expression for the conductance ( $C_{\text{pipe}}$ ) of a pipe with radius  $r$  and length  $L$  is:

$$C_{\text{pipe}} = \frac{\frac{1}{4} \pi c r^2}{1 + \frac{3}{8} L/r} \quad 2.2$$

where  $c$  the velocity of the gas atoms i.e. 475 m/s for nitrogen [2]. The base pressure in the different sections can be calculated for given pumping speeds using these equations.

The second contribution to the base pressure is the gas flow into a section resulting from leaks and pressure differences between sections. The latter is of concern since the Beam Guiding System from the cyclotron operates at a base pressure of  $3 \times 10^{-5}$  mbar while the base pressure in the scattering chamber should be of the order of  $10^{-10}$  mbar. This pressure drop is realised by the application of differential pumping stages in the beam line. An overview of the used vacuum pumps, system design and calculated base pressures is given below for the load lock, scattering chamber and beam line.

### 2.2.1 Load lock

The purpose of the load lock is mainly to act as a sample transfer chamber. The  $1 \times 1 \text{ cm}^2$  sample holders are transported from the sample case into the goniometer head by means of a magnetic rod which moves in a tube with a length of 160 cm. The load lock is pumped by a Leybold Turbovac CSV 150 ls<sup>-1</sup> turbomolecular pump (TMP) and a Leybold Trivac D8B rotary vane pump. To avoid back streaming of small amounts of water vapour and hydrocarbons, originating from the pump oil, a foreline sorption trap filled with activated alumina ( $\text{Al}_2\text{O}_3$ ) or zeolite adsorption material is installed in the inlet line of the rotary vane pump. The pumps are installed

### *Channeling setup*

next to the load lock and are mounted on a separated pump stand. The pressure gauges installed in the load lock are a Pirani TR205 thermal conductivity gauge with a Leybold Thermovac TM200 used in the range of  $10^{-3}$ - $10^3$  mbar and a cold cathode Penning PR45 ionisation gauge with a Leybold Penningvac PM310 used in the range of  $10^{-6}$ - $10^{-2}$  mbar.

The resulting outgassing from the  $4800 \text{ cm}^2$  surface area is  $5 \times 10^{-5} \text{ mbar ls}^{-1}$  using an outgassing coefficient of  $10^{-8} \text{ mbar ls}^{-1} \text{ cm}^{-2}$ . The effective pumping speed in the centre of the chamber is calculated from the conductance of pipe between pump and chamber and the pumping speed of  $150 \text{ ls}^{-1}$  and is reduced to  $100 \text{ ls}^{-1}$ . This results in a base pressure in the load lock of  $5 \times 10^{-7} \text{ mbar}$ . The measured pressure in the load lock is better than  $10^{-6} \text{ mbar}$  indicating that the calculation of the base pressure is correct within a factor of two.

### **2.2.2 Scattering chamber**

The scattering chamber, 50 cm high and 50 cm in diameter, is pumped by a Leybold Turbovac 340M turbomolecular pump with magnetic bearings and a Leybold Trivac D16B rotary vane pump. A foreline sorption trap is installed at the inlet line of the rotary vane pump. The pumping speed of the turbomolecular pump is  $400 \text{ ls}^{-1}$  for  $\text{N}_2$ . In addition, a Leybold V150-2 titanium sublimation pump is installed to reach the  $10^{-10}$  mbar range. The getter screen of the pump is cooled with liquid nitrogen thus resulting in a pumping speed of  $1200 \text{ ls}^{-1}$  for  $\text{N}_2$ . Vacuum gauges used in the scattering chamber are a Pirani TR201 gauge with a Leybold Thermovac TM 200 used in the range of  $10^{-3}$ - $10^3$  mbar and a Bayard-Alpert IE211 ionization gauge with a Leybold Ionivac IM 210 used in the range  $2 \times 10^{-10}$ - $10^{-2}$  mbar. A Leybold QUADRUVAC Q200 quadrupole mass spectrometer is installed for rest gas analysis and leak testing.

The base pressure in the chamber is calculated from degassing of the surface area of the vessel and the present detector disks. The inner area of the vessel and vacuum pipes is approximately  $22500 \text{ cm}^2$  and the detector disks have an area of  $3000 \text{ cm}^2$ . Compared to this area the goniometer area is negligible. The effective pumping speed at the chamber entrance is reduced to  $200 \text{ ls}^{-1}$  through application of the T-piece on the pump stand. Using an outgassing coefficient of  $10^{-8} \text{ mbar ls}^{-1} \text{ cm}^{-2}$ , the calculated base pressure is  $10^{-6} \text{ mbar}$ . In order to reach the UHV condition



cleaning of the inner surface of the vessel, preferentially with trichloroethylene or alcohol, is necessary and has been carried out. When the lowest achievable outgassing coefficient of  $1.3 \times 10^{-11}$  mbar  $\text{ls}^{-1}\text{cm}^{-2}$  is used in the calculation the base pressure will reach  $10^{-9}$  mbar using only the Turbo Molecular pump and  $4 \times 10^{-10}$  mbar with the titanium sublimation pump in operation. Baking out of the vessel and the components might consequently even result in a base pressure of the order of  $5 \times 10^{-11}$  mbar.

The goniometer itself, the detectors and the wires will also contribute to the degassing. The high base pressure of the beam line section introduces a continuous leak. The expected leak from the goniometer feed-through is reduced by application of a differentially pumped feed-through using a Leybold Trivac D8B rotary vane pump.

The measured base pressure in the vessel is  $9 \times 10^{-9}$  mbar when the liquid nitrogen cooled titanium sublimation pump is in operation. This base pressure is sufficient for application of scattering experiments. When required, further decrease of the base pressure can be reached by baking out the vessel. The contribution of the leak from the beam line which operates at a higher pressure can be calculated from the base pressure in that section and the conductance of the connecting pipe. This connection of the beam line vacuum section with the scattering chamber is a pipe of 40 cm length and 2 cm diameter which acts as a differential pumping stage with a conductance of  $2 \text{ ls}^{-1}$  according to equation 2.2. The diameter of the pipe is large enough to allow the ion beam to pass and sufficiently small to assure a pressure drop. The base pressure obtained in that section is calculated in the next paragraph.

### 2.2.3 Beam line

The beam line serves as a differential pumping stage between the UHV scattering chamber and the cyclotron and its Beam Guidance System (BGS) which operate at  $3 \times 10^{-5}$  mbar. The UHV conditions in the scattering chamber can only be obtained when a pressure drop from  $3 \times 10^{-5}$  mbar to  $10^{-10}$  mbar is accomplished. This is realised by the introduction of two additional differential pumping stages in the beam line each with a length of 40 cm and a diameter of 2 cm. Figure 2.2 depicts the side view of the beam line. The scattering chamber is located at the left-hand side.

## Channeling setup

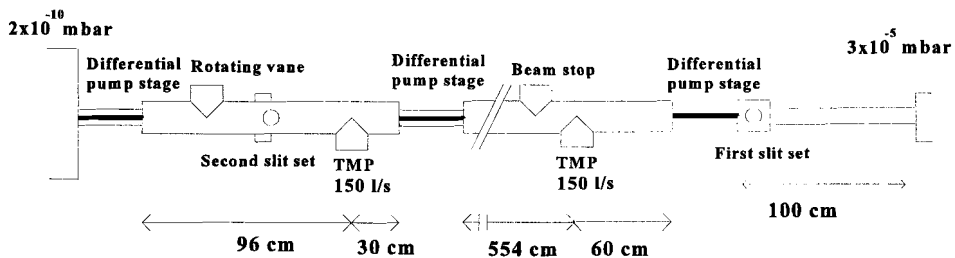


**Figure 2.2:** Side view of the beam line. Location of the rotating vane, beam stop, slit sets, turbo molecular pumps (TMP), and differential pumping stages are indicated in the figure.

The location of the turbomolecular pumps, the differential pumping stages, slit sets and rotating vane are indicated in the figure. The beam line is sub-divided in two sub-sections separated by a differential pumping stage. Vacuum valves separate the beam line section from the scattering chamber and from the beam guidance system. Each beam line sub-section is pumped by a Leybold Turbovac CSV 150  $\text{ls}^{-1}$  turbomolecular pump and a Leybold Trivac D8B rotary vane pump which is equipped with a sorption trap installed at the inlet line. A Pirani TR201 vacuum gauge with a Leybold Thermovac TM 200 and a Leybold Penning PR45 gauge with a Leybold Penningvac PM410 are used to control the vacuum.

The base pressure in each sub-section is calculated from the outgassing ratio and surface area of the beam line and the net gas flow through the differential pumping stages into the section. Contributions have been calculated for each sub-section. The outgassing of the beam stop, the slits and the rotating vane are negligible factors in the calculation of the outgassing due to the small surfaces. The surface areas of the two sub-sections of the beam line are 20000  $\text{cm}^2$  and 3200  $\text{cm}^2$  resulting in a gas flow of  $2 \times 10^{-4}$   $\text{mbar ls}^{-1}$  and  $3 \times 10^{-5}$   $\text{mbar ls}^{-1}$  respectively when an outgassing coefficient of  $10^{-8}$   $\text{mbar ls}^{-1} \text{cm}^{-2}$  is chosen. Cleaning of the components is necessary to obtain UHV conditions in the beam line sub-sections since the 150  $\text{ls}^{-1}$  turbomolecular pumps

limit the base pressure to  $1 \times 10^{-6}$  mbar and  $2 \times 10^{-7}$  mbar for the used outgassing coefficient. The second contribution to the base pressure is the leak flow rate from the BGS into the beam line section in case the valve is opened. This is derived from the pressure difference, the effective pumping speed and the conductance of the differential pumping stages. The effective pumping speed behind the first differential pumping stage is  $80 \text{ ls}^{-1}$ . From the pressure difference of  $3 \times 10^{-5}$  mbar over the differential pressure stage and its conductance of  $2 \text{ ls}^{-1}$  a permanent leak rate of  $6 \times 10^{-5} \text{ mbar ls}^{-1}$  into the first section of the beam line is calculated. This contribution will limit the best achievable vacuum in this section to  $8 \times 10^{-7}$  mbar in case the outgassing coefficient of the walls becomes smaller than  $5 \times 10^{-9} \text{ mbar ls}^{-1} \text{ cm}^2$ . In this case the leak rate into the second sub-section equals  $2 \times 10^{-6} \text{ mbar ls}^{-1}$ . This results in a base pressure of  $2 \times 10^{-8}$  mbar for this sub-section. Consequently the leak rate into the scattering chamber is limited to  $3 \times 10^{-8} \text{ mbar ls}^{-1}$  which results in a best achievable base pressure of  $2 \times 10^{-10}$  mbar which is Ultra High Vacuum. The measured base pressure in the second sub-section of the beam line is  $2 \times 10^{-7}$  mbar and is in agreement with the calculated base pressure.

### 2.3 Vacuum control

The electrical control of the valves, venting valves, turbomolecular pumps and rotary vane pumps of the setup is managed by a Siemens S5-115U Programmable Logic Controller (PLC). The purpose of this PLC is twofold. Prevention from damage of one of the vacuum components and secondly automation of venting and evacuation procedures. The PLC hardware components are designated as input and output units each with 8 to 32 contacts to which a 24 Volt DC voltage can be applied. Analog components are used for the base-pressure read out in a section or sub-section and components with relay connections are used for the control of power-consuming devices such as rotary vane pumps. The PLC software program treats the electrical in and output levels and takes action if a combination of input levels is a request for action. For example the operation of the button on the central control panel requesting the opening of a vacuum valve is treated as a logic input. This request is only carried out if certain conditions, such as a minimum base pressure and running vacuum pumps in both sections, are fulfilled. Only then the vacuum valve is opened. The variety of input signals and control signals allow the programming of automatic routines such as venting and evacuation procedures. When all sections are evacuated

and the ion beam enters the scattering chamber experiments can be carried out.

## 2.4 Data acquisition

The Physics Data Acquisition System (PhyDAS) controls the acquisition and transport of data generated in an experiment and its storage to disk. This system consists of both commercially VME interfaces and home made PHYBUS interfaces that are designed for specific experiments. In the VME bus a processor print (MPS030) built around a 25MHz Motorola 68030 microprocessor is present. The control unit contains a 16Mbyte RAM memory module. The operating system of an MPS030 system is PEP030 [3] which is related to PASCAL. PEP030 has the possibility to add shells around the operating system. These shells contain user defined commands (procedures) and variables. The PEP030 libraries and procedures are loaded from a  $\mu$ VAX fileserver using the Physics Local Area Network (PhyLAN). A more detailed description of PhyDAS has been given by Mutsaers [4].

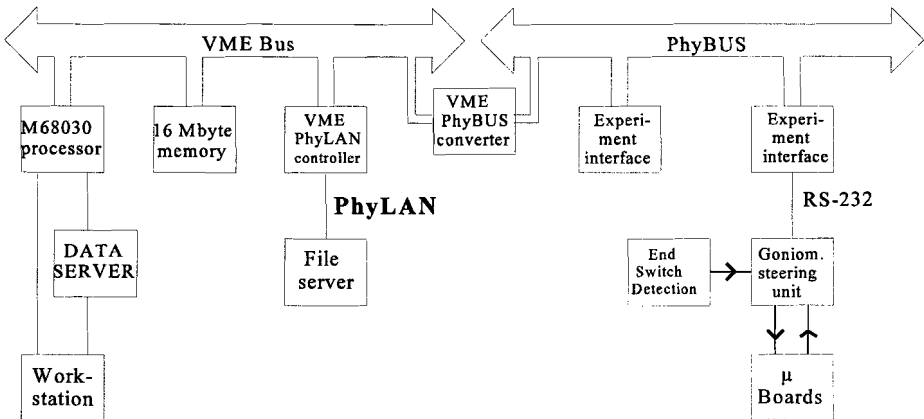


**Figure 2.3:** Schematic view of the computer system. The experimental interfaces such as graphics display controller (GDC), scaler, preset scaler and multi channel analyser are located in the PhyBUS part. The  $\mu$ -boards control the stepper-motors and the decoders.

The generated software procedures used for the control of channeling experiments manage the acquisition of the data; the read out of the MCA memories and the communication with the goniometer steering unit. Some routine measurements that are used in channeling analysis are the measurement of an angular scan and the measurement of an azimuthally averaged RBS spectrum. These measurements are fully automatised using the PEP030 procedures. The data transport to the DEC-AXP 3300 workstation is controlled by means of a link between the MPS030 and a personal computer. The PC disk is a 'remote' disk of the workstation which enables writing the data directly to the disk of the workstation. This system of PC, link controller and its software is called the dataserver. The effective datatransport speed between PhyDAS and the DEC-AXP workstation is about 120 kbyte/s. Figure 2.3 depicts a schematic of the computer system and its periphery indicating the VME part and the PhyBUS part. One of the interfaces used in a channeling experiment is the dual 4048 channel Multi Channel Analyser (MCA) which acquires RBS, ERDA and 'rotating vane' spectra. The current setup permits the use of 6 independent detectors. A Graphics Display Controller (GDC), a scaler and a precision counter provide monitoring of the countrate in the RBS detector as a function of the goniometer position. This is used for alignment of the incident ion beam with respect to a principal crystal axis of the sample. The decreased countrate in a given direction points to channeling of the ion beam in the crystal. The goniometer stepper-motor control is provided by the goniometer-steering unit which communicates with PhyBUS by means of a serial RS-232 interface.

## 2.5 Goniometer characteristics

The goniometer has three axes of rotation; rotation, tilt and spin, and three translation motions and has been built by the central technical workshop at Eindhoven University of Technology. The rotation axis is defined as the vertical axis. The use of the tilt axis will move the top of the sample towards or away from the incident beam and the spin axis coincides with the beam at normal incidence. These three axes and the vertical translation of the goniometer are stepper-motor driven. These stepper motors are located outside the UHV vacuum and are remotely controlled by the goniometer control unit. This unit also controls the stepper-motor driven detector disks. A detailed discription is given in section 2.5.1. The goniometer calibration is described in section 2.5.2. A front view of the goniometer head is shown in figure 2.4.

### *Channeling setup*

The goniometer is mounted underneath the scattering chamber by three points of suspension with leaf springs. These springs are mounted on a sound triangularly shaped frame which is connected to the bottom of the scattering chamber by means of three steel bars and allow the goniometer to move in a vertical direction without losing the horizontal alignment. The possibility of small elastic deformation of the steel bars helps to position the frame in the horizontal plane and allows accurate positioning of the centre of the goniometer head in the centre of the scattering chamber. This horizontal motion is realised with the two in plane translation motions which are adjusted

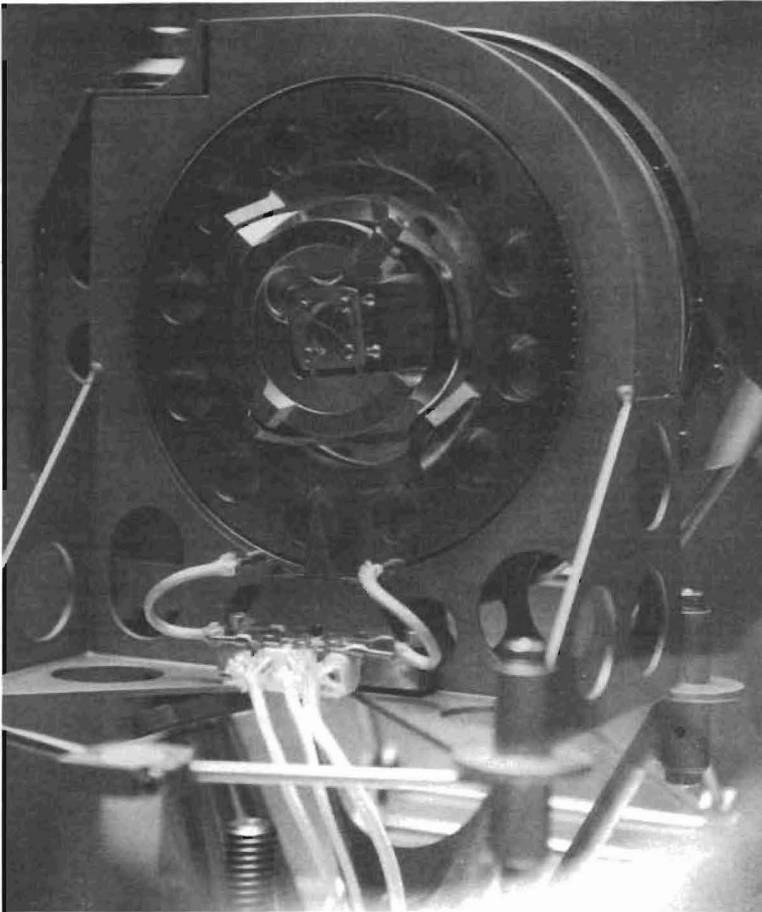


**Figure 2.4:** *Frontview of the goniometer. A  $1 \times 1 \text{ cm}^2$  transmission sample holder with a cross-wire has been inserted in the goniometer head. The vertical axis is the goniometer rotation axis. The tilt axis is in the horizontal axis. The clockwise and counter-clockwise movement of the sample is defined as the sample spin direction.*

with use of a wrench. The goniometer head is designed to contain a 1x1 cm<sup>2</sup> sample holder which is slid in from the side. The sample is fixed in the head by a small clamping spring. The reverse side of the goniometer is shaped as a cone with an apical angle of 90 degrees allowing detection of transmitted and forward scattered ions.

### 2.5.1 Goniometer control unit

The goniometer and the detector disks are controlled by a stand-alone goniometer steering unit. This unit controls 6 stepper motors. The position of each stepper motor is read out by means of a decoder. Furthermore, each motion has a related switch used as a reference and as an end switch. This is a hardware limitation of the range of each axis. The goniometer steering unit has been programmed in a way that the steppermotor is stopped, the motion is reversed and the steppermotor is stopped in case the corresponding end-switch is hit, hereby preventing the goniometer from damaging.

The internal commands that control the goniometer axes are all written in assembly language. The command size varies from 2 to 8 byte. The first four bits of the first byte of the command block concern the identification of the stepper motor. The second byte refers to the command that has to be carried out and the other bytes are optional databytes. These bytes define the direction, speed, steppermotor mode and the number of positions the motor has to take. A command accepted by the goniometer steering unit is carried out and a response command is sent to the master computer.

The commands STOP and GO will stop and start movement of an axis in a defined direction. The command POSITION reads the position of the decoder. The command INIT is a combination of the previous commands. It will start to move the stepper motor until the end switch has been hit. At that point the motion is reversed. During this reverse motion the end switch will restore contact. The stepper motor continues its motion till a reference on the decoder is detected. This reference is taken as a zero setting for the decoder and the stepper motor is stopped at this position. This initialisation procedure is carried out for each axis and for both detector disks and guarantees an accurate, reproducible and unambiguous definition of the reference position. If the

## Channeling setup

end switch is hit during normal operation of the goniometer the corresponding stepper motor is stopped immediately and the axis needs to be reinitialized.

### 2.5.2 Goniometer calibration

This section covers the determination of the conversion factors required to convert decoder position into actual absolute angular position for the three goniometer axes. The calibration of the rotation and of the tilt axis was accomplished using a He-Ne laser. The laser beam was reflected in a double sided mirror that had been mounted on the sample holder in the goniometer head as shown in figure 2.5. The reflected laser beam shows a spot on the wall just behind the laser. A steel ruler was mounted on the wall in order to determine the spot position with an accuracy better than 1 mm. This results in an angular accuracy of  $0.03^\circ$ . The conversion of the spin axis has been performed using the ion channeling technique by determining the location of four identical  $\langle 112 \rangle$  axes of a silicon  $\langle 100 \rangle$  oriented sample.

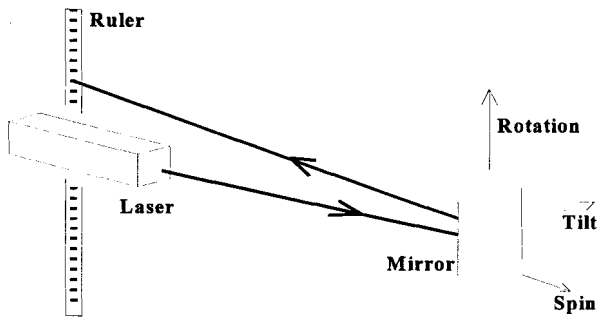


**Figure 2.5:** Setup for calibration of the goniometer axes. The He-Ne laser beam reflects from the double sided mirror and shows a spot on the wall. The spot moves when the position of rotation and tilt axis are changed.



### 2.5.2.1 Calibration of the rotation axis

Movement of the rotation axis shifts the light spot in the horizontal direction. The position of the spot on the wall remains the same after rotation of the sample over 180 degrees. The knowledge that the number of displaced decoder positions is proportional to the angular displacement of the rotation axis suggests that determination of the conversion factor can be carried out by measuring the number of decoder positions for this case. The displacement needed to achieve perfect matching of the reflected spot with its previous marked position on the wall was  $216000 \pm 8$  decoder positions for rotation over 180 degrees. This results in a conversion factor for the rotation axis of 1200 decoder positions per degree and consequently limits the read-out accuracy to  $1/1200$  of a degree. The absolute rotation angle in the laboratory frame of reference is defined with respect to a direction perpendicular to the beam direction. The rotation axis can be positioned within the range of -85 degrees to 257 degrees. The latter sample orientation is used to hit the sample from the rear side. This is enabled by the transmission design of the goniometer head.

The accuracy of the goniometer calibration using the spot location depends on the perception of the naked eye for perfect matching of the two reflected spots. It was experienced that a difference of 0.3 mm could still be distinguished. This corresponds to an angular displacement of  $0.01^\circ$  for the rotation axis which is equivalent with 8 decoder positions.

It is important to note that the calibration of the rotation axis by this “two point-method” is merely possible for a linear transmission, such as a gear wheel transmission, where the amount of displaced decoder positions is directly proportional to the angular displacement of the axis. This proportionality does not hold for the goniometer tilt axis which is moved by a lever construction. Therefore, a more time consuming method had to be used in that case.

### 2.5.2.2 Calibration of the tilt axis

A change of the goniometer tilt axis will move the spot up and down. The tilt axis calibration is carried out measuring the position of the laser spot on wall as a function of the tilt axis decoder position. Note that this function is an uneven function with respect to the tilt axis position at

Channeling setup

normal incidence. At perpendicular incidence the decoder position,  $\delta_{\perp}$ , corresponds to the spot position  $\Delta_{\perp}$  on the steel ruler. This position is called the symmetry point. The best symmetry point was determined from the best third-order polynomial fit through the measured data points. The tangent of the angle between incident and reflected beam corresponds to twice the sample tilt angle. An expression for the sample tilt angle is:

$$\tau = -0.5 \left( \frac{180}{\pi} \right) \text{atan}(\Delta/1942) \tag{2.3}$$

where 1942 (mm) is the distance of the mirror to the wall. The displacement  $\Delta$ (mm) is the spot

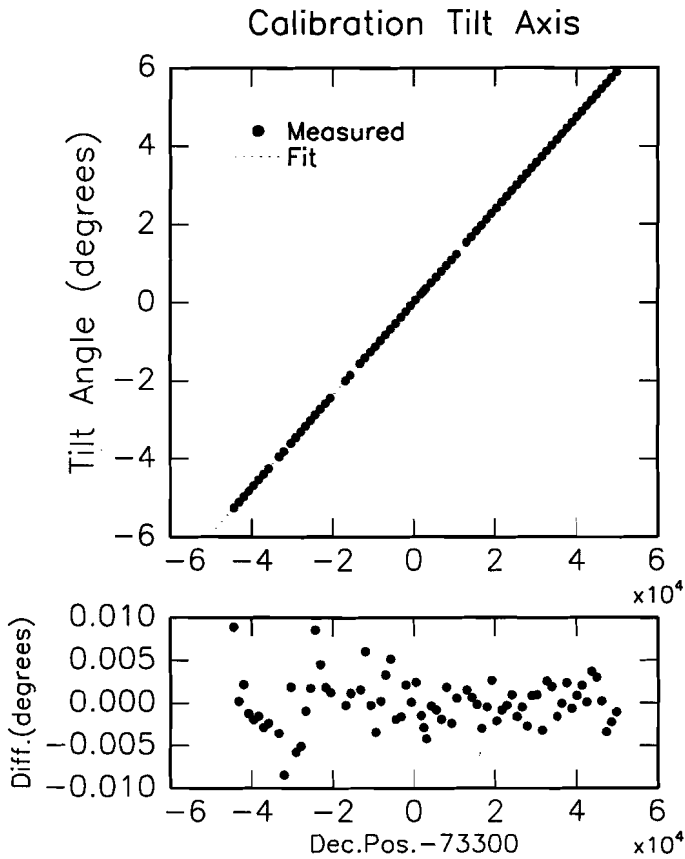


**Figure 2.6:** Calibration of the goniometer tilt axis. The best fit of the tilt angle as a function of the decoder read out. The deviation of the data from the fit is depicted in the figure. The standard deviation of the population is 0.003 °.

position with respect to the spot position  $\Delta_{\perp}$  at perpendicular incidence. The tilt angle sign is chosen positive for the sample normal moving upwards.

Figure 2.6 depicts the sample tilt angle as a function of the decoder position for the best third order polynomial fit using  $\delta_{\perp} = 73300$  decoder positions. This reference position is defined as a tilt angle of zero degrees. The angular deviation of the points from the fit is also depicted in the figure. The standard deviation of the population is  $0.003^{\circ}$ . This value is taken as the calibration accuracy of the tilt axis. The coefficients of the best polynomial fit are listed in table 2.1. These coefficients show that the linear conversion factor is close to 8660 decoder positions per degree.

	$a_0$	$a_1$	$a_2$	$a_3$
<b>value</b>	824.58	-8.0389E-3	3.6212E-10	-4.3299E-14

**Table 2.1** Fit coefficients of the third order polynomial fit. The position on the ruler is given as a function of the tilt axis decoder position.

The range of the goniometer tilt axis is 9 degrees both ways with respect to perpendicular incidence of the beam. Both begin and end point are limited by end switches.

### 2.5.2.3 Calibration of the spin axis

Calibration of the goniometer spin axis is not possible with the use of the laser beam. Therefore, the calibration was carried out in an alternative way using a channeling experiment with 12.6 MeV  $\text{He}^{++}$  ions impinging on a crystalline  $\langle 100 \rangle$  oriented Si crystal. After alignment of the  $\langle 100 \rangle$  axis with respect to the incident ion beam the rotation axis was moved 35.26 degrees away. Spinning of the goniometer was started until a minimum in the backscattering yield, corresponding to the position of a  $\langle 112 \rangle$  axis, was found. The rotation axis was used to relocate the position of the crystalline  $\langle 100 \rangle$  axis which would be changed due to the use of the goniometer spin axis. This change is a result of the fact that the  $\langle 100 \rangle$  crystalline axis does not necessarily coincide with the goniometer spin axis so that slight differences in its position can be expected. Subsequently the tilt axis is used for proper positioning of the  $\langle 100 \rangle$  crystalline axis. Subsequently the angular difference between the location of the  $\langle 100 \rangle$  axis and of the

Channeling setup

$\langle 112 \rangle$  axis was redetermined using the rotation axis. This iterative procedure was repeated and the angular difference was noted. The entire procedure was carried out for the four  $\langle 112 \rangle$  directions. The positions of all four  $\langle 112 \rangle$  minima with their corresponding  $\langle 100 \rangle$  position are listed in table 2.2 and marked as A, B, C and D. The different spin positions for the  $\langle 112 \rangle$  axes are tabulated. Note that opposite  $\langle 112 \rangle$  directions should be exactly 180.00 spin degrees separated, while rotation and tilt axes position differ for these successive sample positions. The measured difference between opposite directions is 179.9317 and 180.0541 degrees, respectively.

$\langle 001 \rangle$		$\langle 112 \rangle$			
Rotation	Tilt	Rotation	Spin	$\Delta(\text{rot})$	
1.4317	2.0068	-33.8267	4.2454	35.2584	A
2.5033	-1.1609	-32.7500	94.2008	35.2533	B
-0.7258	-2.0196	-35.9867	184.1771	35.2609	C
-1.7242	1.0930	-36.9825	-85.8533	35.2583	D

**Table 2.2:** Goniometer spin axis calibration. Values are in degrees. The measured angular difference between the different  $\langle 001 \rangle$  and  $\langle 112 \rangle$  axes is depicted as  $\Delta$ . The mean value is:  $\Delta = 35.2577 \pm 0.003^\circ$ .

This results in a mean value of 179.9929 degrees. The drive mechanism of the spin axis is based on a gear wheel transmission and therefore justifies the assumption of a proportional relation between the decoder position and the actual angular position of the axis. The measured angular difference corresponds to 432000 decoder positions for a 180 degree displacement of the spin axis, which corresponds to 2400 decoder positions per degree. The spin-axis displacement ranges from -135 degrees to 226 degrees.

Apart from the spin-axis positions the angular differences between the  $\langle 100 \rangle$  and  $\langle 112 \rangle$  crystalline axes, as measured with the goniometer rotation axis, are also tabulated in table 2.2. Theoretically a 35.264 degree difference is expected. The measured mean angular difference is  $35.258 \pm 0.003$  degrees. The standard deviation in this value is a measure for the accuracy reached in the experiment where 12.6 MeV  $\text{He}^{++}$  ions are used. This value confirms the accuracy of the goniometer rotation axis over a large range.

### 2.5.2.4 Calibration of the vertical displacement

The vertical displacement of the goniometer is stepper-motor driven and further referred to as the z-axis. It is used to align the goniometer centre with respect to the incident beam. A calliper rule is used to measure the vertical displacement as a function of goniometer decoder position. This results in a conversion factor of 43600 decoder positions per millimetre. The range of this translation stage is 8.2 mm.

### 2.5.3 Hysteresis of goniometer axes

Although the mechanical properties of the goniometer are designed to have a superior angular accuracy, hysteresis is inherent in a mechanic drive such as a gear wheel transmission where always some backlash or torsion is present. The hysteresis in both goniometer rotation and tilt axis has been measured in an RBS-channeling experiment using 25 MeV He<sup>++</sup> ions impinging on a silicon <100> oriented crystal. Since high-energy ions result in relatively small angular scans, it will be easier to detect hysteresis. The angular scans are acquired with increasing and decreasing angle. Present hysteresis in the goniometer axis results in a different position of the goniometer head for the identical decoder position depending on the approach from the different directions. The hysteresis has been determined from the angular shift of the successive angular scans.

The axial minimum of a silicon <100> oriented crystal is aligned with the 25 MeV He<sup>++</sup> beam using the goniometer rotation and tilt axis. A series of energy spectra is acquired for different target orientations. Selection of the backscattering yield in an interval in these spectra results in an angular scans as depicted in figure 2.7. The figure shows the measured angular scans through the <100> minimum using the goniometer rotation and tilt axis. Note that the starting point for each scan is also approached from the same direction as the direction in which the scan is measured. The measured angular shift is  $0.030 \pm 0.001$  degrees for both goniometer axes. This shift is clearly visible thanks to the narrow angular scans. The obtained value for the hysteresis is used as a correction on the measured angular difference of two crystalline axes in case these positions are determined using opposite scan directions. Measurement of connected angular scans using identical scan direction makes correction unnecessary and is, therefore, more practical.

### Channeling setup

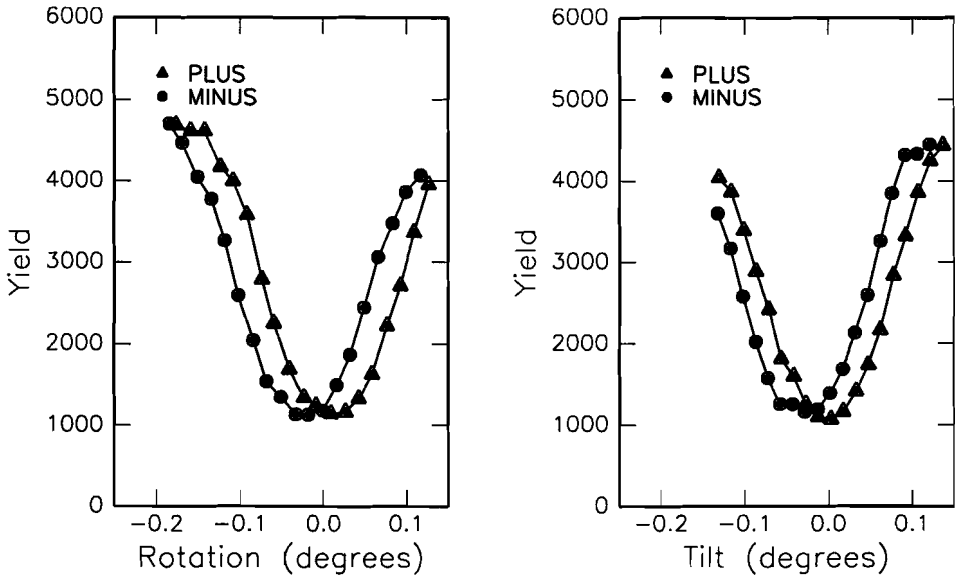


**Figure 2.7:** Measurements of the hysteresis of rotation and tilt axis with a 25 MeV  $\text{He}^{++}$  beam on (100)Si. Angular scans were obtained in two directions. Both rotation and tilt axis show a  $0.03^\circ$  shift of the subsequent angular scans.

#### 2.5.4 Accuracy of the rotation axis

The last property of the goniometer that had to be determined was the accuracy of the rotation axis. How accurate can the absolute position of the goniometer be determined and how reproducible is that position independent of hysteresis effects? This quantity differs from the read-out accuracy and has been determined by measuring the slope of the Si  $\langle 100 \rangle$  angular scan using 12.6 MeV  $\text{He}^{++}$  ions. The best fit through the measured points is referred to as the expectation value. The angular accuracy has been derived from deviations using the expectation value. The  $\langle 100 \rangle$  crystalline axis was aligned with respect to the incident beam and the slope was measured using the goniometer rotation axis. To enhance statistics a  $900 \text{ mm}^2$  detector was used with an opening angle of 63 msr. An accuracy in the normalised backscattering yield of better than 1% was realised when an acquisition time of 5 minutes was used. Figure 2.8 shows the measured backscattering yield from an energy window in the RBS spectrum as a function of the detected sample position. The selected window corresponds to a sample slice close to the

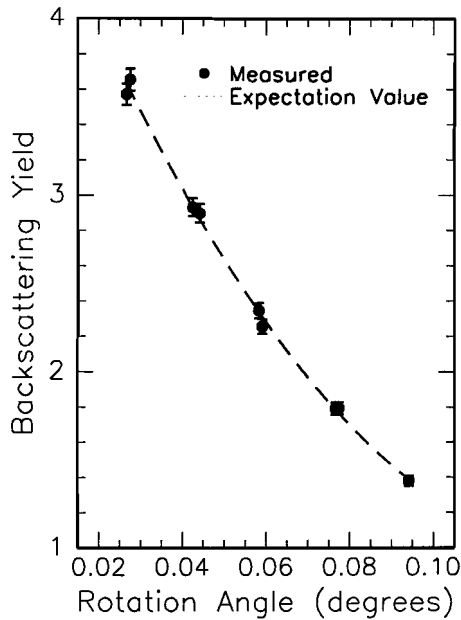


**Figure 2.8:** Measurement of the accuracy of the goniometer rotation axis. The edge of a 12.6 MeV  $He^{++}$   $\langle 100 \rangle$  angular scan is depicted in the figure. The fit through the data points is treated as the expectation value. Deviations from the fit are smaller than 1/1200 of a degree.

sample surface. After the sample was repositioned with the goniometer rotation axis at a position one degree ahead of its starting position, the angular scan was repeated. The angular deviations from the expectation value have been calculated for each data point. The mean difference of this deviation was equal to *one* decoder position. This implies that the read-out accuracy limits proper measurement of the exact accuracy of the rotation axis. We conclude therefore that the accuracy is better than or equal to 1/1200 of a degree.

### 2.5.5 Summary

The conversion factors of the goniometer axes determined in the previous section are summarized in table 2.3 The exact ranges of the subsequent axes are also depicted in the table. Remember that the absolute position of the goniometer axes is defined with respect to perpendicular incidence of the beam. The hysteresis of the goniometer rotation and tilt axis is  $0.03^\circ$ . Hysteresis is avoided when related angular scans are measured in the identical direction.

## Channeling setup

The accuracy of the goniometer rotation axis is better than 1/1200 of a degree.

Axis	Conversion (DECPOS/°)	Range
Rotation	1200	-85° - +257°
Tilt	8660	-9° - +9°
Spin	2400	-136° - +226°
Z-axis	43600 DECPOS/mm	8.2 mm

**Table 2.3:** Summary of the conversion factors of all goniometer axes. The angular range of each goniometer axis is depicted in the third column.

## 2.6 Detector-disk characteristics

Two independent stepper-motor driven detector disks are present in the channeling scattering chamber. End switches limit the range of each detector disk and are used as a reference position for the initialisation procedure. Both the RBS and recoil detector disks are equipped with detector holders in which the detectors are placed. These detectors are electrically isolated from the scattering chamber. The angular dimensions and detector ranges are 180 degrees and 90 degrees, respectively. For convenience an angular scale is engraved on the disks. This simplifies the

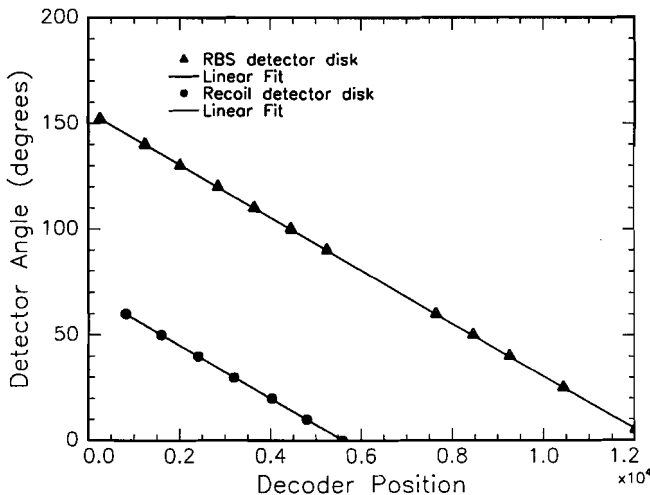


**Figure 2.9:** The figure shows the detector angle as a function of the read out decoder position for the two present detector disks. This results in a calibration of 0.0125° per decoder position. (80 dec.pos per degree)



determination of the location of the detector on the disk. The actual detector angle in the scattering chamber is determined by the position of the detector on the disk and the disk position with respect to the end switch. The latter is read out as a decoder position equivalent to the goniometer axes read out. Calibrations of the detector angle versus the read out decoder position have been carried out and are shown in figure 2.9. The angular detector position is defined with respect to the direction of the incident beam. The calibration results in a conversion factor of 80 decoder positions per degree for each disk.

## 2.7 Experiments and procedures

In RBS experiments the energy of the ions scattered from the atoms in the sample is measured and stored in an MCA. Combination of RBS with channeling will result in a decreased backscattering yield with respect to the target orientation. An accurate measure for the decline is the ratio of the random yield and the backscattering yield in the case a main crystalline axis of the sample is aligned with respect to the incident beam. Determination of the ratio requires an accurate dose measurement which is independent of the sample orientation. In this section three methods for beam dose measurement will be discussed. Prior to the RBS-channeling experiments a channel-to-energy-calibration is carried out with use of an AmCm source which emits  $\text{He}^{++}$  with energies of 5.443 MeV, 5.486 MeV, 5.764 MeV and 5.805 MeV. The source is mounted on a sample holder that fits in the goniometer head. These acquired energy spectra are furthermore used for determination of the energy resolution.

After successful alignment of the beam on the goniometer centre, the sample is mounted in the goniometer head. The Graphic Display Controller monitors the backscattering yield as a function of the target orientation and is used to align the sample with respect to a principal crystal axis. For the analysis of backscattering spectra quantities such as differential cross section, detector solid angle, stopping power and the number of incident projectiles on the sample (dose) are essential [5] and need to be accurately known. The dose can be measured in three ways. First the number of ions can be determined from the ion charge state and the measured accumulated charge on the sample. This requires insulation of the sample from the scattering chamber. A second possibility is measurement of the charge incident on an isolated beam chopper located

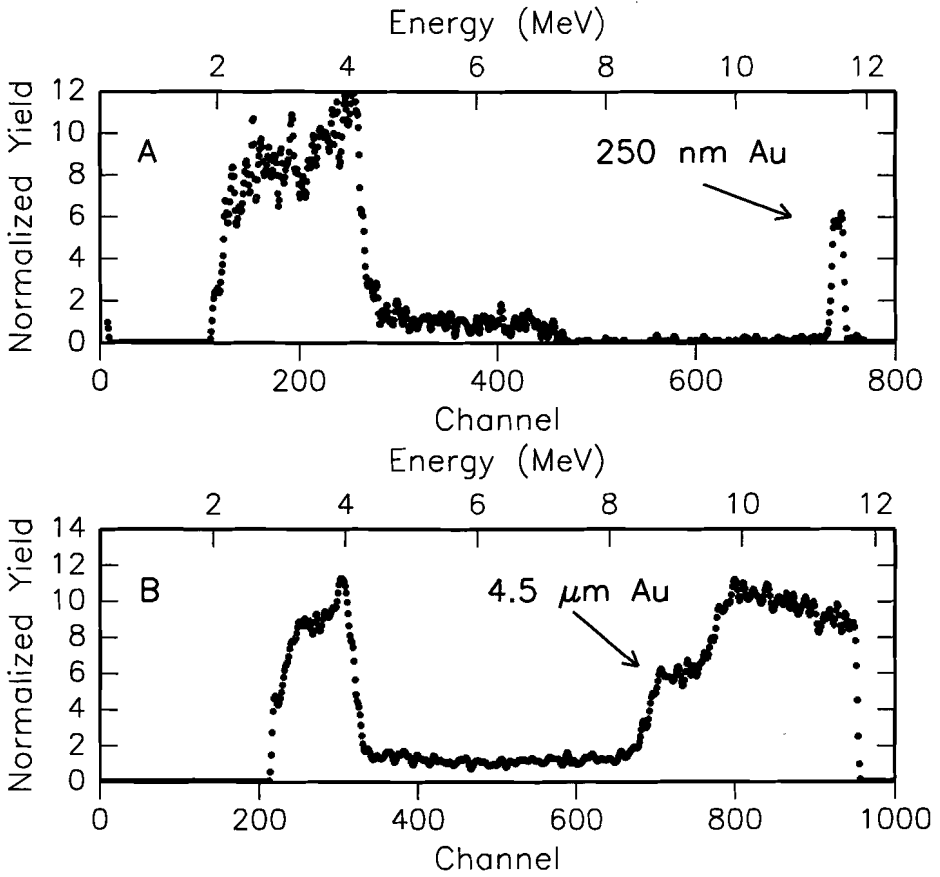


**Figure 2.10:** Backscattering energy spectra from the rotating vane using a 12.6 MeV  $\text{He}^{++}$  incident ion beam. The detector is positioned at a  $150^\circ$  backscattering angle. The thickness of the gold top layer is 250 nm for figure 2.9 A and  $4.5\mu\text{m}$  for figure 2.9 B.

ahead of the scattering chamber. This would be a fixed fraction of the charge incident on the sample. Generally charge measurement on the sample or on a wire is complicated because of the occurrence of secondary electron emission. Suppression of this effect is realised by the placement of a suppression shield surrounding the sample. A negative voltage applied to this shield results in a repulsive force on the emitted electrons, hereby suppressing the emission. However, installation of a suppression shield in the present chamber would drastically limit the freedom of movement of the goniometer. A third possibility is the use of a signal proportional to the

number of incident ions. We use the number of ions backscattered from a beam chopper that is located ahead of the scattering chamber. This chopper is further referred to as the rotating vane. The vane consists of an aluminum propellor with a deposited gold layer. The energy of the scattered ions is measured with a detector located at a 150 degree backscattering angle. The number of counts in the gold peak is proportional to the number of incident ions and is therefore used as a measure of the incident ion dose. Typical energy spectra from ions with an energy of 12.6 MeV are depicted in figure 2.10. The first energy spectrum is acquired using a vane with a top layer of 250 nm of gold and the second one is acquired using a vane with a top layer of 4.5  $\mu\text{m}$ . The vane with the thick gold top layer is favourable for its higher count rate in the gold peak which results in better statistics for the very same ion dose. However the use of the vane in a 4 MeV  $\text{He}^{++}$  experiment will result in an energy spectrum where no separate gold peak is visible. The top layer is too thick and ions backscattered at the interface will be fully stopped before they exit the sample. In that case the counts in a limited region of the spectrum are used as a measure for the incident ion dose.

### 2.7.1 Absolute dose calibration

The relation between the number of counts in the gold peak and the absolute number of incident ions on the sample is determined from measurement of the accumulated charge on the Faraday cup and the simultaneously measured rotating vane spectrum. This allows derivation of the incident beam dose from the area of the gold peak in the rotating-vane spectrum. The multi-sector Faraday cup is surrounded by a tube to which a voltage can be applied for the suppression of secondary electron emission. In an experiment the ion current on the Faraday cup has been measured as a function of the voltage applied to the suppression tube. The voltage applied to the suppression tube ranged from 0 Volts to -100 Volts. Figure 2.11 shows the measured integrated beam current as a function of the applied voltage on the suppression tube. It is noticed that the measured beam current is higher in case no voltage is applied. This increase is expected since emission of electrons induces a positive current since secondary electrons have only 0-20 eV energy. An applied voltage will suppress the emission and thus reduce the measured current. The suppression effect is limited to the region where the applied voltage ranges from 0 till -40 Volts and corrects the measurement by almost a factor of seven. Analysis of backscattering spectra

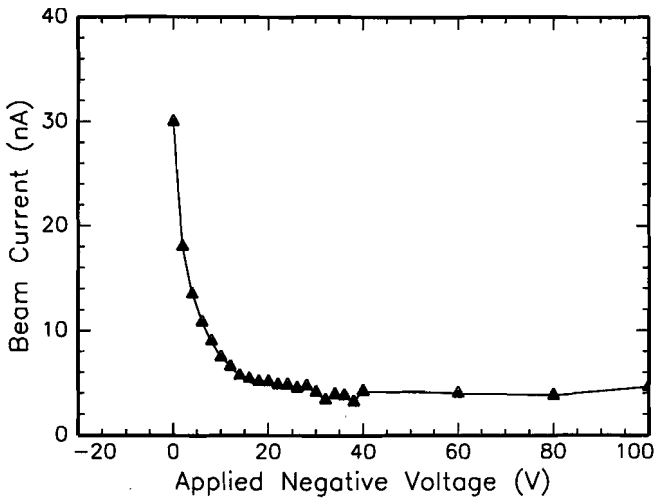


**Figure 2.11:** Faraday cup charge measurement as a function of the applied voltage to the electron suppression tube.

show that the absolute number of ions derived from the determined conversion factor is still underestimated by a factor of four. The origin of this discrepancy has not been found yet. The possibility that the ion beam hits the suppression tube should be considered.

Alternatively the charge measurement can be carried out on the sample holder as long as the sample is a conductor. However, it is known that the measured current strongly depends on the target orientation. Therefore, the effect of the sample orientation on the charge measurement is examined.

Figure 2.12 shows the ratio of charge, measured on the faraday cup, and the counts in the rotating-vane energy spectrum as a function of the sample rotation angle. The charge conversion factor is near 100 pC per count in the acquired rotating vane spectrum. The incident angle on the sample is measured with respect to the sample normal. For glancing incidence on the sample the effect of the increased secondary electron emission is noticed as an increased beam current. A difference of a factor of five is noticed for glancing angle incidence. The deviation exceeds the 10 percent systematic error for 35 degree glancing angle already and increases rapidly for larger

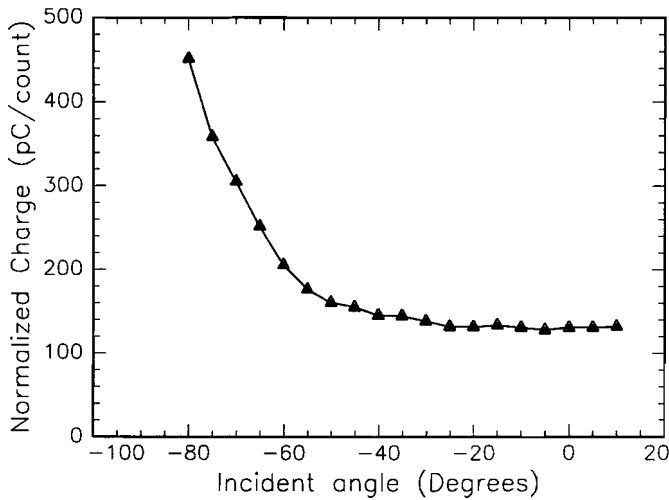


**Figure 2.12:** Charge measurement on the sample as a function of sample orientation with respect to the incident ion beam. The  $0^\circ$  incident angle refers to a perpendicular incidence on the target.

angles. The measured current drops to zero for angles close to 90 degrees since at this orientation the beam spot will not hit the sample anymore. The measured current is still overestimated by a factor of two for perpendicular incidence. This suggests that if a proper absolute charge measurement is required either the Faraday cup needs improvements or a different charge measurement on the sample should be proposed.

## 2.8 Conclusions

The construction of a scattering chamber for channeling experiments is successfully accomplished and a base pressure of  $8 \times 10^{-9}$  mbar is obtained in the scattering chamber. This base pressure has already been reached without baking-out of the vessel. The calibration of the custom made goniometer is applied and measurement of the accuracy confirm its superior angular precision, around  $0.001^\circ$  for the three rotations. A hysteresis of  $0.03^\circ$  is observed for the rotation axes. Ion beam analysis experiments have been carried out successfully using a simultaneously measured RBS spectrum from a rotating vane as a relative reference for the ion dose acquired in a measurement. When high energy ions are used a rotating vane with thick ( $4.5 \mu\text{m}$ ) gold layer is necessary to obtain sufficient statistics. The absolute calibration of the acquired rotating vane counts versus the collected dose is still complicated due to production of secondary electrons in

### *Channeling setup*

the target. The electron production rate depends significantly on the orientation of the target with respect to the incident ion beam.

### **References**

1. L. Wolterbeek Muller, *Vacuümtechniek beginselen en toepassingen*, Kluwer Technische Boeken B.V. Deventer (1989).
2. A. Roth, *Vacuum Technology*, North-Holland Publishing Company, Amsterdam (1982).
3. W.M. Dijkstra, *PEP programmeertaal voor de microgiant*, internal report Eindhoven University of Technology FTI/BA 87-02 (1987) (in dutch).
4. P.H.A. Mutsaers, *Design and realisation of the Eindhoven Scanning Proton Microprobe*, PhD Thesis (1995)
5. W.K. Chu, J.W. Mayer, M.A. Nicolet, *Backscattering Spectrometry*, Academic Press Inc. (1978)

# 3

## Ion scattering and channeling experiments

*This chapter presents some of the early channeling experiments measured in the new UHV scattering chamber that were carried out to test the setup and the data-acquisition system for ion-channeling and scattering experiments for materials analysis. The purpose of this chapter is to summarize the computerized measuring system and to summarize experimental procedures, monitoring of data and a brief outline of sorting and post-processing of data. The in-home-made data monitoring program COLUMBUS is introduced. This relational data base facilitates presentation of acquired data and is used to have a first glance at the experimental results and select angular scans from energy intervals in the obtained spectra. After a first impression of the measured data quantification and detailed analysis can be carried out off-line.*

*In order to prove the feasibility of the concept of an enhanced angular resolution obtained with high-energy ions the energy dependence of the angular-scan width has been studied. Therefore ion-trajectory simulations have been carried on (100) oriented silicon using He ions with energies between 3 and 30 MeV. The effect of the fractional beam divergence on the shape of the angular scans has been examined using the MC trajectory calculations for angular-scan simulations. In this respect two characteristic features of the angular scans have been studied: i.e. the scan width and the minimum yield. Restrictions of the beam divergence of the incident ion beam are given in terms of a fraction of the characteristic angle for channeling;  $\Psi_1$ .*

*Subsequently three angular scans have been measured using 4 MeV, 12.6 MeV and 25 MeV He ions. The characteristic features of these measured angular scans are discussed and restrictions with respect to experimental parameters are evaluated.*

### 3.1 Monitoring of spectra and normalized angular scans

In an RBS ion-channeling experiment the energy of the backscattered ions is measured and stored in a multi channel analyser (MCA) as described in section 2.4 and 2.7. The energy spectra are monitored using the program COLUMBUS, which allows to plot the data obtained from the three multi-channel analysers (MCA) and sort this data with one-minute intervals, thus creating a pseudo-on-line measurement. The data-monitoring program permits creation of multiple user-defined windows on the screen: i.e. energy spectra and scatter plots. The data-sets have a unique data-format and are read from disk and thus available for post-processing. Post-measurement data processing such as channel-to-energy calibration, selection and monitoring of angular scans can be implemented. A typical angular-scan experiment will be described in this section to show the features of the monitoring program and the goniometer control.

Figure 3.1 depicts the setup of the computer screen such as available in an angular-scan experiment using 4 MeV He<sup>+</sup> ions. This example is obtained from a <111> angular scan of an MBE-grown heterostructure of GaAs/AlGaAs/InGaAs/GaAs as is described in detail in chapter 5. The detector in the scattering chamber is the 50 mm<sup>2</sup> PIPS detector and is located at a backscattering angle of  $\Theta=170^\circ$ . The beam impinges the sample near  $54^\circ$  with respect to the sample normal. The beam exit angle is  $44^\circ$  with respect to the sample normal. The measured energy spectra are denoted as ‘Chamber hist.’ and ‘Rotating Vane hist’. These windows depict the integrated data of all measured energy spectra of an angular scan. The energy spectrum obtained in the scattering chamber shows a small peak near channel 600. This peak originates from ions that scattered from the In atoms in the buried InGaAs layer. The Ga and As surface positions in the RBS spectrum are near channel 550. Each window reports the measured time (~3.5 hours), accumulated ion dose (~1.4 mC) and integrated number of detected ions (counts). The beam current indicated in the spectra has been measured from the goniometer head and is overestimated due to the glancing angle incidence of the ion beam on the sample (section 2.7.1). This value is therefore not used for quantification of the accumulated ion dose. Alternatively the integrated number of counts in the rotating vane spectrum is taken. In this experiment the rotating vane with the 4.5  $\mu\text{m}$  gold top layer is used (section 2.7). The ions backscattered at the Au/Al interface will be fully stopped before they exit the Au layer, which explains the lack of a



separated Au peak in the rotating-vane spectrum. The 'Microbeam Phydas' window, in the upper right corner of the figure, lists the goniometer position for the three rotation axes (tilt, spin and rotation) and the stepper-motor-controlled transverse motion (z-axis). The actual position of the goniometer in this example is the sample load position. The decoder positions listed in the right column are converted to the axial position of each axis (second column) using the calibration functions as determined in chapter 2. The 'status' reports that the stepper motor has been initialized. The stepper-motor speed is indicated in the third column.

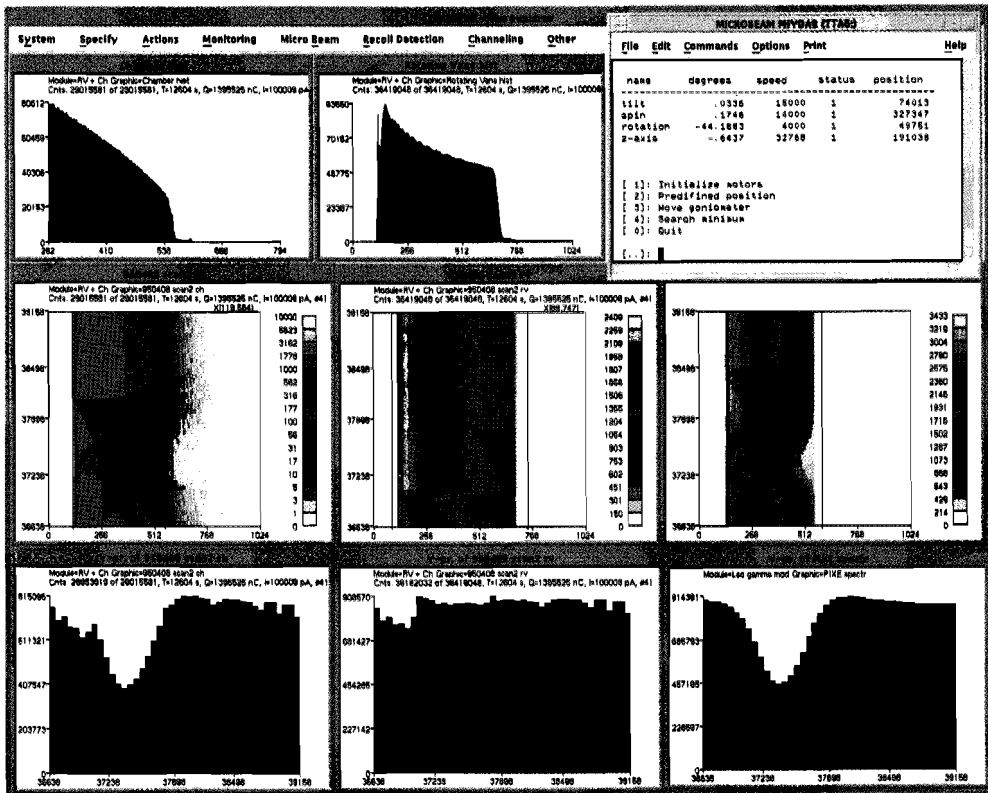


**Figure 3.1:** Representation of the monitoring screen as obtained in an angular scan experiment. The goniometer position is given in the 'Microbeam Phydas' window as plotted in the upper right corner. The angular scans are sorted from the three-dimensional representations of an angular scan. The lower right corner depicts the angular scan that is corrected for variations in accumulated ion dose and is referred to as normalized angular scan.

In case of an angular-scan measurement a three-dimensional representation can be obtained from the dataset of measured spectra. These scatter plots show the channel numbers, corresponding to the energy of the detected particles, along the horizontal axis and the decoder position of the rotation axis along the vertical axis. The data set depicted in figure 3.1 has 42 spectra. The full width of the angular-scan interval is 2520 decoder positions which corresponds to 2.1 degrees and this corresponds to one energy spectrum obtained at every 0.05 degree. The number of counts in the scatter plots is represented by a color. By selecting an interval along the horizontal energy axis, which corresponds to a certain depth interval in the sample, an angular scan can be obtained by the projection of the number of counts on the vertical axis. A non-normalized angular scan can be monitored during the measurement and give an estimate on the progression of the experiment (lower left corner of the figure). A similar scattering plot is subsequently obtained from the rotating vane (RV) detector as is depicted in the centre of figure 3.1. The integrated RV counts are plotted as a function of the sample position and depicted in the window next to the angular scan. This rotating-vane plot depicts the accumulated dose for each spectrum. A slight variation of the integrated charge per measured spectrum is observed. The rotating-vane plot is used to normalize the 'raw' angular scan with respect to the collected beam-dose per position. The normalized angular scan is depicted in the lower-right corner of the figure. As shown in the figure this beam-dose correction affects the shape of the angular scan significantly and is therefore unavoidable when conclusions on the shape of the scan are drawn. In this experiment sufficient statistics of the In signal, that has been used to determine the strain of the InGaAs layer, was crucial to obtain a relevant angular scan. Therefore the accumulated charge per sample position must be typical some micro coulombs before normalised angular scans can be obtained with sufficient statistics.

### 3.2 Incident-ion energy and angular scan width

The energy dependence of the angular-scan width has been studied to prove the feasibility of the concept of an enhanced angular resolution as obtained with high-energy ions. Therefore ion-trajectory simulations and measurements have been carried on (100) oriented silicon using He ions with energies between 3 and 30 MeV. Two characteristic features of the angular scans have been studied: i.e. the scan width and the minimum yield. We use the simulation program

LAROSE, developed by Barrett [1], that provides the study of the angular scans using different beam and sample parameters. An important parameter in channeling experiments is the angular spread of the incident ion beam, i.e. the beam divergence. Ion-channeling experiments require a parallel ion beams, thus the beam divergence must be sufficiently small with respect to the characteristic angle for channeling. The actual beam divergence used in a channeling experiment will always compromise between limited beam divergence and sufficient beam current because the latter determines the count rate and statistics in an experiment. Since the use of high-energy ions results in a reduction of the critical angle for channeling (typical with  $\Psi_c \sim E^{-1/2}$ ), the beam divergence must be more restricted when high-energy ions are used. Reduction of the angular spread of the incident ion beam is experimentally accomplished by the slits in the beam line as is described in chapter 2. To comprehend the effect of an angular spread of the incident ion beam on the shape of the measured angular scans simulations of angular scans are carried out with different beam divergence.

### 3.2.1 Simulation of angular scans

To investigate beam-divergence effects, a series of angular scans have been calculated with the

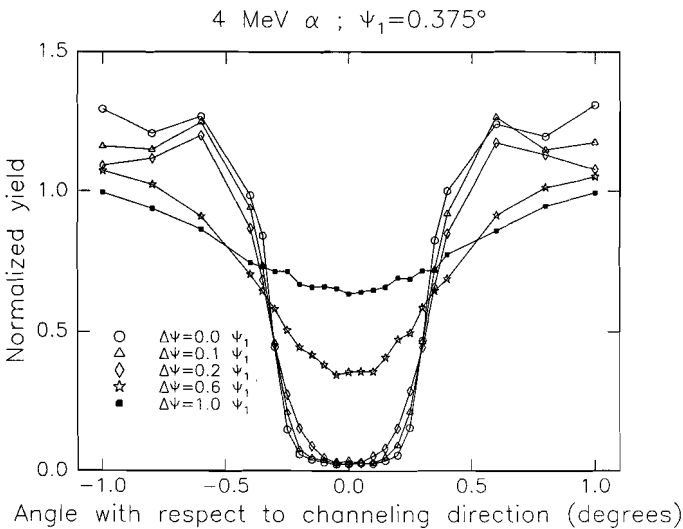


**Figure 3.2:** Angular scans for 4 MeV alphas.

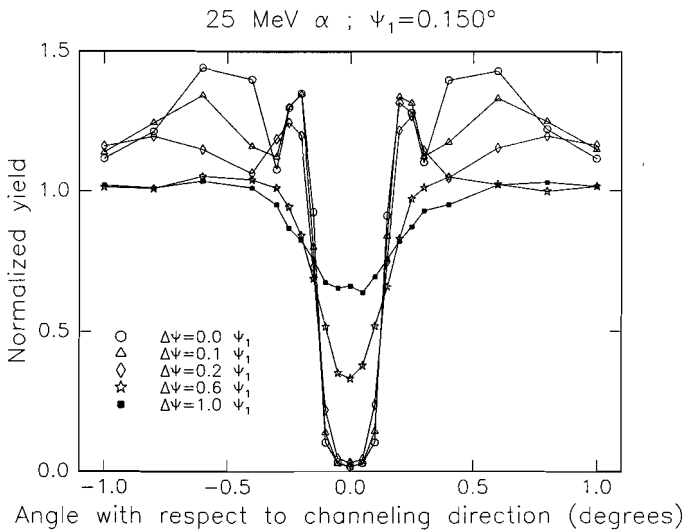


**Figure 3.3:** Angular scans for 25 MeV alphas.

channeling simulation program LAROSE. The series consists of scans computed for the  $\langle 111 \rangle$  axial direction in silicon while scanning in a plane  $6^\circ$  out of the (110) plane. Angular scans were obtained for alpha particles of various energies. To eliminate oscillatory behaviour, the normalized nuclear encounter probabilities, appearing in the angular scans, were obtained by averaging the values over 260 atomic layers (thickness 122.2 nm), situated at a depth of 3950 Å below the surface of the silicon crystal. For each set, representing a specific case concerning one particular ion energy, 6 angular scans have been computed in which the beam divergence  $\Delta\Psi$  was varied according to fixed fractions of the characteristic angle  $\Psi_1$ . (the average atomic spacing  $d$  in  $\langle 111 \rangle$  silicon is 4.70314 Å). The fractions were 0.0, 0.1, 0.2, 0.3, 0.6, and 1.0 respectively. The value of the beam divergence  $\Delta\Psi$ , used in the MC program, is the RMS value of a Gaussian distribution of the angular spread of the incident ion beam.

In figures 3.2 and 3.3, calculated angular scans for 4 MeV and 25 MeV alphas as functions of beam divergence are presented. No error bars have been indicated in the plots since they are smaller than the symbols used for plotting the points. First of all, we see the decrease of the angular width using higher ion energies, as expected. Furthermore, both plots clearly show the

effects of a finite beam divergence on axial angular scans. It is clear that a beam divergence results in an increase of the minimum yield which in fact can be quite substantial for relatively large divergences. Furthermore, the scans are stretched out with increasing beam divergence, which is reflected by larger values for the half-width at half-minimum,  $\Psi_{1/2}$ , with respect to the zero-divergence scan.

The angular scans shown here give an overall impression of the distortion of angular scans by the beam divergence. In the following we will more explicitly specify these effects by investigating the behaviour of the minimum yield  $\chi_{\min}$  and half-angle  $\Psi_{1/2}$  that characterize each angular scan, as functions of the beam divergence. The half-angle is defined as the angle away from the channeling direction at which the normalized yield is midway between the minimum value along the channeling direction and 1 (the value in a random direction). In figure 3.4 the minimum yields as functions of the fractional beam divergence are shown for the angular scans computed for alpha particles with different energies. In figure 3.5 the angular-scan widths as functions of the fractional beam divergence are shown for these angular scans. The conclusion that may be drawn based on figure 3.4 is that the minimum yield increase as a function of the fractional beam divergence does not show any energy dependence. Consequently, effects of a finite beam divergence on the minimum-yield behaviour for a given channeling direction can be regarded to be a universal function of the fractional beam divergence only. Considering the

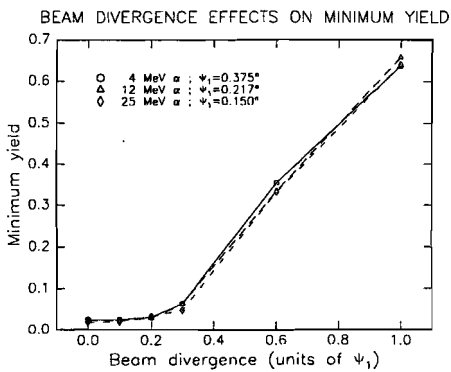


**Figure 3.4:** *Minimum-yield behaviour.*

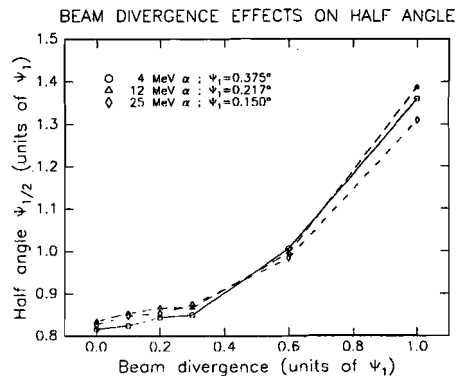


**Figure 3.5:** *Angular-width behaviour.*

behaviour of this function, we see that the minimum yield increases rather slowly for fractional beam divergences smaller than 0.3. For larger divergences, the minimum yield starts increasing more rapidly approaching 70% of the random yield near a fractional divergence of 1. Considering figure 3.5, we recognize a similar behaviour as that of the minimum yield.

From the results of the angular-scan calculations obtained with 4 MeV, 12.6 MeV and 25 MeV alphas, we conclude that the distortion of angular scans by a finite beam divergence depends only on the fractional beam divergence. Energy dependent effects have not been observed. With respect to the tuning of beam divergence in an experimental situation we conclude that when fractional beam divergences are kept below 0.2, measured angular scans exhibit only a small distortion from the ideal zero divergence scan. It is to be expected that defect profiling (chapter 6) will require fractional beam divergences below 0.2. In case of well separated angular scans, strain determination (chapter 4) will not be influenced by beam divergence effects since absolute angular positions of angular scans are not affected.

### 3.2.2 Angular-scan measurement

The simulations show that channeling with high-energy ions can successfully be carried out when the beam divergence is carefully controlled and kept small enough with respect to the characteristic angle. In an attempt to obtain an angular scan with high-energy ions and to show the feasibility of the concept of the use of an improved angular resolution, we measured angular scans of a (100) oriented silicon crystal using different ion energies. In order to cover a broad range of available energies three angular scans through the  $\langle 100 \rangle$  axis were measured using 4 MeV, 12.6 MeV and 25 MeV He ions. The 900 mm<sup>2</sup> PIPS detector was located at an angle of  $\theta=135^\circ$  with respect to the incident ion beam. Because of the rapidly decreasing cross-section for elastic scattering with increasing energy, a large detector (900 mm<sup>2</sup>) has been used to enhance the observed scattering yield. However, the use of this detector with a large solid angle limits depth resolution. The crystal orientation, where the main crystallographic axis coincided with the incident beam, was found using a rate meter that monitored the backscattering yield in the detector. Minimalisation of the backscattering yield by moving the crystalline orientation with respect to the incident ion beam resulted in the goniometer position for perfect alignment of the

$\langle 100 \rangle$  main crystalline axis with the He ion beam. Subsequently the energy spectra were obtained using the rotation axis of the goniometer. The angular scans were sorted from an energy interval in the acquired backscattering spectra and the observed yields were plotted as a function of target orientation. For detailed comparison and quantification of the change of the observed half-width at half-maximum,  $\Psi_{1/2}$ , scans should be sorted from identical near-surface depth intervals, and they should be measured in identical planes (i.e. in the (100) or (110) plane through the  $\langle 100 \rangle$  axis) and normalized to the random yield. Furthermore, the maximum angular spread of the incident ion beam,  $\Delta$ , (beam divergence) must be kept small with respect to the characteristic angle for channeling  $\Psi_1$ .

Figure 3.6 shows the 3 angular scans, through the  $\langle 100 \rangle$  axis in the (100) plane, obtained with 4 MeV, 12.6 MeV and 25 MeV He ions. The trend of decreasing scan width with increasing ion energy is clearly observed. We determined the half-width at half-minimum from the measured

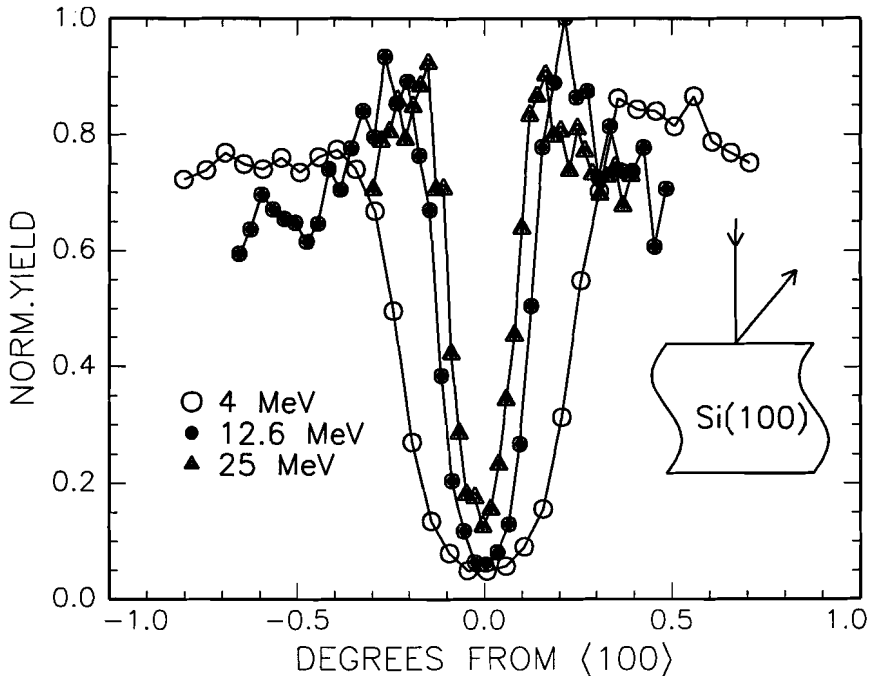


**Figure 3.6:** Angular scans through the  $\langle 100 \rangle$  axis of a silicon crystal. The angular scans have been obtained using 4 MeV, 12.6 MeV and 25 MeV He incident ions. The narrowing of the scan-width with increasing ion energy is clearly observed.

angular scans and we found scan widths:  $\Psi_{1/2}=0.19^\circ$ ,  $\Psi_{1/2}=0.13^\circ$ , and  $\Psi_{1/2}=0.09^\circ$ , respectively. The observed minimum yield for the 25 MeV angular scan is significantly higher than the minimum yield observed in the 4 MeV and 12.6 MeV angular scans. This might be caused by experimental parameters. Therefore some characteristic parameters will be evaluated.

The selected energy interval in the spectra correspond to a depth interval near the surface of 1.1  $\mu\text{m}$  for both 4 MeV and 12.6 MeV experiment. The large acceptance angle of the detector in the scattering plane limits depth resolution to  $\sim 0.1\mu\text{m}$  and  $\sim 1\mu\text{m}$ , respectively. This indicates that selection of a similar depth interval in energy spectra obtained with different energies will be complicated. In addition, the demand for sufficient statistics requires a relatively large depth interval needed to be chosen in the 25 MeV experiment. The thickness of this near-surface depth interval was 12  $\mu\text{m}$  with a depth resolution of  $\sim 3\mu\text{m}$ . For these relatively large depth intervals the minimum-yield increase due to dechanneling might become important. Dechanneling studies have been presented earlier by Campisano, Grasso and Rimini [2] and Matsunami and Howe [3]. These studies conclude that the axial dechanneling as a function of depth is proportional to the energy of the incident ion, which implies that the axial dechanneling yield for 25 MeV ions in 12  $\mu\text{m}$  interval near the surface would be comparable to the axial dechanneling rate at 1  $\mu\text{m}$  in a 2 MeV experiment. The axial-dechanneling data, obtained at room temperature, indicate an increase of the minimum yield from 2% to 4% [4]. We observed a minimum yield increase much higher, which suggests that other effects are dominant in our experiment.

A closer look is taken at the fractional divergence of the incident He ion beam. The angular spread of the incident He ion beam is restricted by the diaphragms, which were set by the slits (chapter 2). The maximum angular spreads (in the horizontal and vertical plane) of the incident ion beam were  $\Delta=0.077^\circ$  for the 4 MeV experiment ( $\Psi_1=0.35^\circ$ );  $\Delta=0.074^\circ$  for the 12.6 MeV experiment ( $\Psi_1=0.20^\circ$ ) and  $\Delta=0.060^\circ$  for the 25 MeV experiment ( $\Psi_1=0.14^\circ$ ). In terms of the characteristic angle this maximum angular spread corresponds to  $\Delta=0.22\Psi_1$ , for 4 MeV;  $\Delta=0.38\Psi_1$  for 12.6 MeV and  $\Delta=0.43\Psi_1$  for 25 MeV alphas. This maximum angular spread should be compared to the FWHM of the Gaussian angular distribution that was used in the angular-scan simulations. This value of the beam divergence was defined in section 3.2.1 as  $\Delta\Psi$ ,



thus  $\text{FWHM}=2.35 \times \Delta \Psi$ . The simulations showed that a significant increase of the minimum yield can be expected when the beam divergence  $\Delta \Psi$  is larger than  $0.2 \times \Psi_1$ . This would restrict the maximum angular spread  $\Delta$  to:  $2.35 \times 0.2 \times \Psi_1 = 0.5 \times \Psi_1$ . Consequently a slightly increased minimum yield could be expected in the 25 MeV experiment, where  $\Delta = 0.43 \Psi_1$ , as has been observed in figure 3.6. We therefore conclude that angular scan measurements with He ions and energies up to 12.6 MeV can be carried out successfully but that the beam divergence should be restricted further when higher ion energies, i.e. 25 MeV He ions, are preferred.

### **3.3 Conclusions**

The data-acquisition software COLUMBUS is implemented in the experimental setup and serves as a semi-on-line representation of the acquired data. Energy spectra and scatter plots can be obtained in an angular-scan experiment. Simulations of angular scans with an angular spread of the incident ion beam shows that both the minimum yield and the measured angular-scan width depend only on the fractional beam divergence. Energy-dependent effects have not been observed in the simulations. With respect to the tuning of beam divergence in an experimental situation we conclude that when fractional beam divergences are kept below 0.2, measured angular scans exhibit only a small distortion from the ideal zero-divergence scan. We measured the  $\langle 100 \rangle$  Si axial angular scans successfully using 4 MeV, 12.6 MeV and 25 MeV incident He ions. The trend of decreasing scan width with increasing ion energy is clearly observed. The increased minimum yield, observed in the 25 MeV experiment is due to the relatively large angular spread of the incident ion beam. This effect can be explained in terms of the fractional beam divergence and of the results of the angular-scan simulations obtained with LAROSE. For future experiments the maximum angular spread of the incident ion beam ( $\Delta$ ) must be kept smaller than  $0.4 \times \Psi_1$ , where  $\Psi_1$  the characteristic angle for channeling.

**References**

1. J.H. Barrett, Phys. Rev. B 3 (1971) 1527.
2. S.U. Campisano, F. Grasso and E Rimini, Rad. Effects 9 (1971) 181.
3. N. Matsunami and L.M. Howe, Rad. eff. 51 (1980) 111.
4. K. Gärtner, K. Hehl and G. Schlotzhauer, Nucl. Instr. and Meth. B 4 (1984) 55.

# 4

## Strain in $\text{Si}_{1-x}\text{Ge}_x/\text{Si}$ heterostructures measured with high-energy ion channeling

*This chapter presents strain analysis of silicon based  $\text{Si}_{1-x}\text{Ge}_x$  heterostructures with high-energy ion channeling. Strain analysis using ion scattering is usually carried out with beam energies  $< 2$  MeV. Use of higher energies is often limited by the energy range of the accelerator. The conceptual understanding of strain will be treated in section 4.2 as well as how it effects the lattice constant perpendicular to the substrate and the physical properties of an epitaxial structure. This perpendicular lattice constant can be obtained for  $\text{Si}_{1-x}\text{Ge}_x$  strained thin films with ion channeling experiments applying high-energy (10-15 MeV)  $\text{He}^{++}$  ions. The requirements for the use of high beam energies will be discussed in section 4.3. The summarized list with points of attention is a blueprint of the considerations important for successful application of strain measurement of commensurately grown thin layers in general and is also applicable if the characterized structures consist of a combination of particular III-V elements.*

*High-energy ion channeling has been applied to single-layer quantum wells and buried layers of  $\text{Si}_{1-x}\text{Ge}_x$  on a Si(100) substrate where the germanium content varies between  $x=0.05$  and  $x=0.25$ . Results on strain analysis will be presented in section 4.4 and 4.5. Section 4.6 gives a detailed comparison of strain analysis using 4 MeV and 12.6 MeV ions for the characterisation of the strain of a buried  $\text{Si}_{1-x}\text{Ge}_x$  layer ( $x=0.175$ ). Dominant steering effects are expected when 4 MeV ions are used since in that case the kink angle is of the order of the critical angle for channeling,  $\Psi_1$ . A close resemblance of the measured germanium angular scan with a scan obtained with Monte Carlo trajectory calculations will be presented in section 4.7. A detailed correspondence of scan simulations with the experimentally obtained scans further enhances the reliability and accuracy of the determined strain. Since beam induced strain relaxation has been reported in literature, the effect of the probing ion beam on the stability of the incorporated strain in the strained layer lattice has been studied as presented in section 4.8. Section 4.9 will summarize conclusions obtained from the strain analysis with high-energy ion channeling.*

## 4.1 Introduction

High-energy ion channeling is used to determine the strain of silicon based  $\text{Si}_{1-x}\text{Ge}_x/\text{Si}$  heterostructures. Results are compared with strain measurements previously carried out on both single  $\text{Si}_{1-x}\text{Ge}_x$  films and superlattices[1] with MeV  $\text{He}^+$  ions (beam energies  $< 2$  MeV). Pioneering work of Fiory et al. [2] showed that strain of a 10 nm  $\text{Si}_{1-x}\text{Ge}_x$  film ( $x=0.5$ ) could be calculated from its misaligned off-normal  $\langle 111 \rangle$  channel using 1.8 MeV incident  $\text{He}^+$  ions. The angular difference, or kink angle, between minimum yields for the substrate and the strained layer (as determined by the germanium yield) is interpreted in terms of the tetragonal distortion,  $\epsilon_T$ , produced by biaxial compressive strain in the (100) plane. The misalignment with respect to the  $\langle 111 \rangle$  substrate channel is further referred to as  $\Delta\theta_{\langle 111 \rangle}$ . Strain measurements with relatively high energies ( $> 2$  MeV) are scarce. Hashimoto et al. [3] used 3.5 MeV incident  $\text{He}^+$  ions and determined the strain of  $\text{CaF}_2$  films, grown by molecular beam epitaxy (MBE) on a Si (111) substrate. Angular scans have been measured around the off-normal  $\langle 110 \rangle$  and  $\langle 114 \rangle$  axes in the (110) plane. Okamoto et al. also determined the strain of  $\text{NiSi}_2$  epitaxial films grown on Si(111) [4]. The strain in the  $\text{NiSi}_2$  layer was derived from the measured kink angle with an experimental accuracy of 0.07% in the tetragonal distortion  $\epsilon_T$ .

The use of high-energy ions is favourable since the characteristic angle for channeling ( $\Psi_1$ ) decreases with  $E^{-1/2}$ . Consequently this results in narrow angular scans which improves the angular accuracy and thus the exact determination of the position of a crystalline axis. This is why the applicability of 12.6 MeV  $\text{He}^{++}$  ions in strain analysis has been studied. Use of high-energy ions further reduces the ion-steering effect at interfaces thanks to the smaller characteristic angle. Even further reduction of the ion-steering effect can be obtained when high-index axial directions such as  $\langle 112 \rangle$  or  $\langle 114 \rangle$  are used.

Alternative techniques that give structural information with a comparable angular resolution are Raman spectroscopy and, traditionally used, double crystal X-ray diffractometry. Also extensive analysis of thin films can be carried out with Transmission-Electron Microscopy (TEM). For Raman scattering, or Raman spectroscopy (RS) the sample is irradiated with a laser, typical

514.5 nm [5]. The incident photons raise the scattering medium from the ground state to a higher virtual state and an electron-hole pair is created. Through electron-lattice interaction a collective excitation (e.g. a phonon) is created in the medium. Subsequently an electron-radiation interaction causes the electron-hole pair to recombine while emitting a photon. The frequencies of the emitted optical photons are analyzed with a double monochromator and are characteristic for the medium since they depend on photon-phonon interactions. The wave vector and energy of the phonons are derived from conservation of energy and momentum in the interaction sequence. Strain in the layer results in a change of the wavelength of the optical phonons of the layer. For Raman scattering the penetration and probing depth ranges between 10 and 10<sup>3</sup> nm, depending on the frequency of the probe laser. The strain sensitivity of Raman is approximately 10<sup>-5</sup> [6]. Raman spectroscopy provides reliable data for strains with an uncertainty of 10<sup>-4</sup> only when phonon deformation potentials are accurately known. Alternatively, double crystal X-ray diffractometry can be applied to characterize strain of an epitaxial Si<sub>1-x</sub>Ge<sub>x</sub> layer [7][8]. This technique uses Cu K<sub>α</sub> (0.15406 nm) or Fe K<sub>α</sub> (0.1936 nm) X-rays as a source to determine parallel and perpendicular strain,  $\epsilon_{\parallel}$  and  $\epsilon_{\perp}$ , from rocking curves. In this case the rocking curve is considered as a superposition of the diffraction peaks of the different layers and the substrate peak. The sensitivity of the X-ray method (10<sup>-7</sup>) is two or three orders of magnitude higher than that of RS [9]. The typical accuracy reached with glancing angle high-resolution X-ray diffractometry is 10<sup>-4</sup> [10] for the determination of the strain in multi-layered structures.

Compared to X-ray diffractometry and Raman Spectroscopy, ion scattering gives additional information with respect to the depth dependent elemental composition of the sample and, therefore, offers the unique ability to determine strain by measuring crystallographic orientations of individual layers as done in characterisation of strained layer superlattices (SLS) [11][12]. The third technique, TEM, provides structural information of the lattice location of atoms and can confirm commensurate growth. This technique is extremely sensitive to characterisation of defect regions and types of defects in the structure. The necessity of careful sample preparation and the relatively small ( $\mu\text{m}$ ) lateral characterized sample region limit the applicability of this technique.

## 4.2 Coherency strain in commensurately grown thin films

The use of the ion-channeling technique for coherency strain analysis of a heterostructure is based on the determination of the position of an off-normal crystalline axis of each epitaxial layer. The shape and the size of the deformed unit cell define the angles between these main crystalline axes which differ from the angles in a cubic crystal. Silicon, germanium and their binary alloys have a simple cubic diamond-type lattice. The bulk lattice constant of binary alloys of silicon and germanium and alloys of III-V mixtures is generally calculated using Vegard's law [13]. For a  $\text{Si}_{1-x}\text{Ge}_x$  bulk crystal this implies a virtual bulk crystal lattice constant,  $a_v$ , which is the average of the bulk silicon and germanium lattice constants, weighted by the mole fraction  $x$ . The virtual bulk lattice constants can be tuned continuously by adjusting the relative fractions of Si or Ge. Adding germanium to silicon also changes the physical properties of the material. Increasing the germanium content of the  $\text{Si}_{1-x}\text{Ge}_x$  alloy causes the bandgap to narrow. This narrowing effect is magnified by the strain of the layer. Bandgap tuning is thus possible by varying both the germanium content and the amount of strain in the layer. Study of the fabrication of defect-free strained films is carried out using epitaxial growth techniques such as molecular beam epitaxy (MBE), chemical beam epitaxy (CBE), chemical vapour deposition (CVD) or related techniques. In this respect ion-channeling experiments contribute to the characterization of the strain and of the number of defects in the grown structures.

Consider an epitaxially grown layer whose bulk lattice parameter differs from that of the substrate. The misfit factor,  $f$ , is defined as the relative difference between the virtual bulk lattice constant of the film and the lattice constant of the substrate [14]. Coherency growth of the epitaxial film implies that the in-plane lattice constant of the film equals the lattice constant of the substrate. A film of a certain composition, with virtual lattice constant larger than the substrate, has to be compressed before it can fit on the substrate. This is defined as compressive strain. In contrast, tensile strain results when the bulk lattice constant of an epitaxially grown film is smaller than that of the substrate. In-plane squeezing of the lattice will force the perpendicular lattice constant to increase while the in-plane tensile stretching will force its perpendicular lattice constant to decrease. A quantity for the strain is the tetragonal distortion,  $\epsilon_T$ . As a consequence of the strain in the layer, the off-normal crystalline axes of the strained layer differ by a small

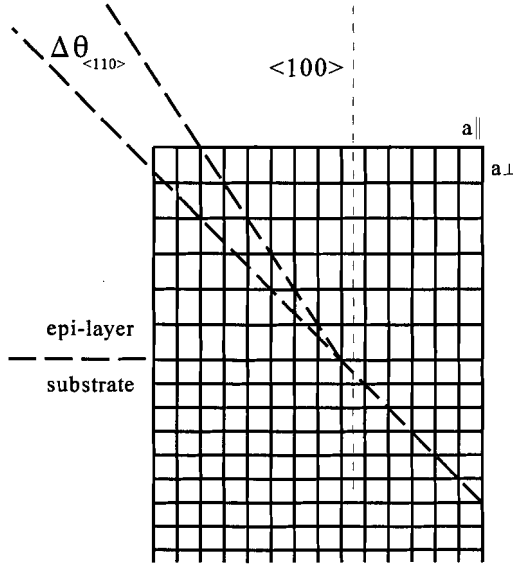


**Figure 4.1:** Schematic of an epitaxially grown layer on a  $\langle 100 \rangle$  oriented substrate with lattice parameter  $a_s$ . The compressively strained epi-layer has in-plane lattice parameter  $a_{||}$  and perpendicular lattice parameter  $a_{\perp}$ . The kink angle, occurring at the interface is indicated as  $\Delta\theta_{\langle 110 \rangle}$ .

angle,  $\Delta\theta$ , from the identical axes of the cubic substrate. This instant kink angle occurs at the interface of the substrate and the commensurately grown thin film. Ion-channeling experiments determine the strain in the epitaxially grown film directly from the measured kink angle and use this result as a measure for the lattice deformation. Figure 4.1 is a schematic of a compressively strained layer, epitaxially grown on a substrate with in-plane lattice parameter  $a_s$ . The kink angle  $\Delta\theta_{\langle 110 \rangle}$ , occurring at the interface, is indicated in the figure.

A rigorous derivation of the lattice deformation under biaxial stress has been treated by Tsao [15]. The adopted model, known as Hooke's law for cubic crystals, correlates the stresses in the film along the sample normal to the strains in the film along the sample normal. In case the epitaxial film has a free surface, which is the case during growth, Hooke's law reduces to a simple relation between planar strain and perpendicular strain. This relation assumes known macroscopic elasticity constants  $C_{11}$ ,  $C_{12}$  and  $C_{44}$ , which are calculated as linear combinations of elasticity constants of the individual elements, weighted by their mole fraction. For cubic

materials the law is commonly written in terms of Poisson's ratio,  $\nu$ , and the shear modulus,  $\mu$ . A summary of formulas used in the channeling experiments is given below. These equations are valid when the grown films are thinner than the critical thickness for the film. Beyond the critical thickness misfits are introduced in the strained layer, thereby minimizing the coherency energy. All analyzed samples are considered to be strained layers with a thickness smaller than the critical thickness,  $t_c$ , unless differently stated.

Consider the initial stage of the epitaxial growth of a thin film on a clean substrate with in-plane lattice constant  $a_{\parallel}$ . The atoms that arrive at the sample and have sufficient thermal energy migrate over the surface and will end up in lattice sites in a way that the in plane lattice constant is similar to that of the substrate. When the lattice constant of the grown alloy differs from the in-plane lattice constant of the substrate, in-plane compressive or tensile strain will result in a tetragonal distortion of the unit cell. During the growth the epitaxial film has a free surface and its lattice deformation is such that the perpendicular stresses ( $\sigma_z$ ) in the layer vanish. The in-plane stress results in an in-plane strain which has two components  $\epsilon_x$  and  $\epsilon_y$ . These components are identical when the substrate is oriented along the  $\langle 100 \rangle$  direction due to symmetry. For a fully coherent epitaxial layer the relation between the in-plane ( $\epsilon_{\parallel}$ ) and perpendicular ( $\epsilon_{\perp}$ ) strain is given in terms of Poisson's ratio:

$$\epsilon_{\perp} = \frac{-2\nu}{1-\nu} \epsilon_{\parallel} \quad 4.1$$

Poisson's ratio lies in the range 0.25-0.35 for most materials ( $\nu_{Si}=0.2782$  and  $\nu_{Ge}=0.2932$ ). The tetragonal distortion,  $\epsilon_T$ , is a relation between the in-plane and the perpendicular strains:

$$\epsilon_T = \epsilon_{\perp} - \epsilon_{\parallel} = (a_{\perp} - a_{\parallel})/a_v \quad 4.2$$

where  $a_{\perp}$  is the perpendicular lattice constant,  $a_{\parallel}$  the in-plane lattice constant and  $a_v$  the virtual crystal lattice constant for a bulk crystal with composition of the commensurate film. The in-plane strain,  $\epsilon_{\parallel}$ , and the perpendicular strain,  $\epsilon_{\perp}$ , are defined as the relative deviations of the



lattice constants from the virtual crystal lattice constant  $a_v$ .

For commensurate growth the off-normal channel of the strained layer is misaligned with respect to the off-normal channel of the substrate. The resulting geometrical kink angle,  $\Delta\theta$ , measured from the shift of the angular scan, is directly related to the tetragonal distortion as:

$$\Delta\theta = \epsilon_T \sin\theta \cos\theta \quad 4.3$$

where  $\theta$  is the angle of the off-normal axis, measured from the axis normal to the sample surface. The angular shift is defined negative in the case of compressive strain and positive in the case of tensile strain.

The strain in the film introduces coherency energy in the film. For a commensurate grown layer with misfit  $f$  a critical film thickness  $t_c$  can be derived. At this film thickness the strain energy in the layer is sufficient to introduce misfits, thereby reducing the strain energy in the film. Matthews and Blakeslee [16] adopted a model to calculate this critical film thickness as a function of the misfit factor,  $f$ . Houghton et al. [17] showed that the model successfully predicts the critical thickness for a Si<sub>1-x</sub>Ge<sub>x</sub> strained layer on a (100) silicon substrate for a composition with a germanium fraction between 0.00 and 0.15. They used X-ray topography and Nomarski microscopy for sample characterisation. Nomarski microscopy permits single dislocation detection over an entire wafer. A defect density of  $\approx 1 \text{ cm}^{-1}$  was taken as a limit for coherent growth. Bean et al. [18] characterized MBE-grown Si<sub>1-x</sub>Ge<sub>x</sub> layers with TEM, RBS and X-ray analysis. Observation of the commensurate/incommensurate transition was used to determine the value of the critical thickness. They found critical thicknesses for Si<sub>1-x</sub>Ge<sub>x</sub> ( $x=0.1-0.5$ ) films significantly larger than those presented in the study of Houghton et al. or predicted by equilibrium theory proposed by Van der Merwe [19]. This suggests that misfits are introduced in a later growth stage or at higher growth temperatures or that the number of introduced misfits is below the detection limit of the techniques. Introduction of misfits results in initial relaxation of the meta-stable layer and reduces the strain in the thin film. The considered types of stacking faults are edge dislocations and screw dislocations. Presence of these structural defects degrades

significantly the performance of semiconductor devices. The layer relaxes further by introduction of more structural defects. In the case of a fully relaxed layer, the kink angle is negligible and lots of defects are present in the layer and at the interface as is noticed in the channeled RBS spectra.

### 4.3 Requirements for the analysis of SiGe thin films with high-energy ions

In this section strain analysis of  $\text{Si}_{1-x}\text{Ge}_x$  epitaxial films with high-energy ion channeling will be discussed. At first a parallel beam with limited angular spread and an accurate three-axis goniometer are required. In all our experiments the angular spread of the incident beam was controlled by means of collimator slits in the beam line and was limited to a maximum angular spread of  $0.07^\circ$ . This is sufficiently small with respect to the critical angle for 12.6 MeV  $\text{He}^{++}$  channeling in a (100) silicon crystal ( $\Psi_c=0.20^\circ$ ). The three-axis goniometer has a superior angular accuracy, as has been shown in chapter 2. Angular scans are measured for energy intervals in the obtained spectra. The detected elastically scattered ions from germanium atoms in the strained layer and the elastically scattered ions from the silicon atoms in the substrate were selected to obtain angular scans from these heterostructures. A high count rate of these signals is preferred in order to acquire sufficient statistics. This demands sufficient beam current and a sufficiently high scattering cross-section. Use of a detector with a large solid angle will enhance the count rate significantly. Routine angular-scan measurements require full automation of the goniometer and data-acquisition system.

Unfortunately, the use of high energies in ion-scattering experiments results in a decreased Rutherford scattering cross-section, typical by a factor of  $E^{-2}$  [20]. In addition, a higher ion-energy will result in a closer nuclear encounter which might result in a nuclear reaction of the projectile with the target nucleus or might result in inelastic scattering which leaves the target nucleus in an excited state. These effects often result in complicated spectra with overlapping signals which can not be interpreted unambiguously. Thus the preferential use of elastic scattering sets a limit to the ion energy. The threshold ion energy, at which deviations from Rutherford scattering occur, can be calculated by adopting the model of Bozoian [21]. This threshold energy is a function of the scattering angle and of the atomic numbers of both the projectile and target atom. For  $170^\circ$  backscattering of  $\text{He}^{++}$  ions from silicon the calculated

threshold energy is 3.9 MeV. For scattering from germanium the threshold is 8.5 MeV. Consequently, the intention to use energies between 10 and 15 MeV needs some study on the scattering cross-section for germanium and silicon. The search for a resonance in the cross-section for elastic scattering is the most obvious first step. Unfortunately, cross-sectional data for He<sup>++</sup> scattering from germanium at energies between 3 and 30 MeV is not available in literature. Therefore, the germanium yield was measured as a function of scattering angle using 12.6 MeV He<sup>++</sup> ions. The sample consisted of a strained buried 65 nm Si<sub>1-x</sub>Ge<sub>x</sub> layer (x=0.175), capped with a 61 nm Si layer, that had been grown on a Si(100) wafer by Atmospheric Pressure Chemical Vapour Deposition (APCVD). The thin isolated Si<sub>1-x</sub>Ge<sub>x</sub> layer provides an isolated peak in the RBS spectra, assigned to ions scattered from germanium. The sample was oriented at an angle of 45 degrees with respect to the beam direction. This geometry permits scattering angles ranging between  $\theta=180^\circ$  and  $\theta=45^\circ$ . To enhance sensitivity and to increase the count rate a large 900 mm<sup>2</sup> detector was used. This results in a solid angle of 63 msrad which corresponds to an acceptance angle of 16° in the scattering plane resulting in kinematic dispersion which limits good depth resolution. For this typical situation the lack of depth resolution is not important since a detailed depth profile is not desired and the Si/SiGe/Si sample is a single layer quantum well structure.

Figure 4.2 shows the energy spectra obtained at four different scattering angles. The germanium and silicon surface positions are indicated in all energy spectra. For backscattering angles of 118° and 98° the germanium yield in the spectral region of interest is multiplied by a factor of 60. A gain in absolute scattering yield of one order of magnitude has been accomplished when the detector is moved from 98° to 54°. Furthermore, the germanium scattering yield increases more rapidly towards smaller angle than the silicon scattering yield. Thus the forward scattering geometry is preferred when high sensitivity for germanium is required. The Si scattering yield in all spectra reflects the occurrence of many resonances in the scattering cross section for (in)elastic scattering from silicon. The exact shape of this scattering yield depends on the used ion energy and scattering angle. These yield variations are very much suppressed in the channelled spectrum [22].

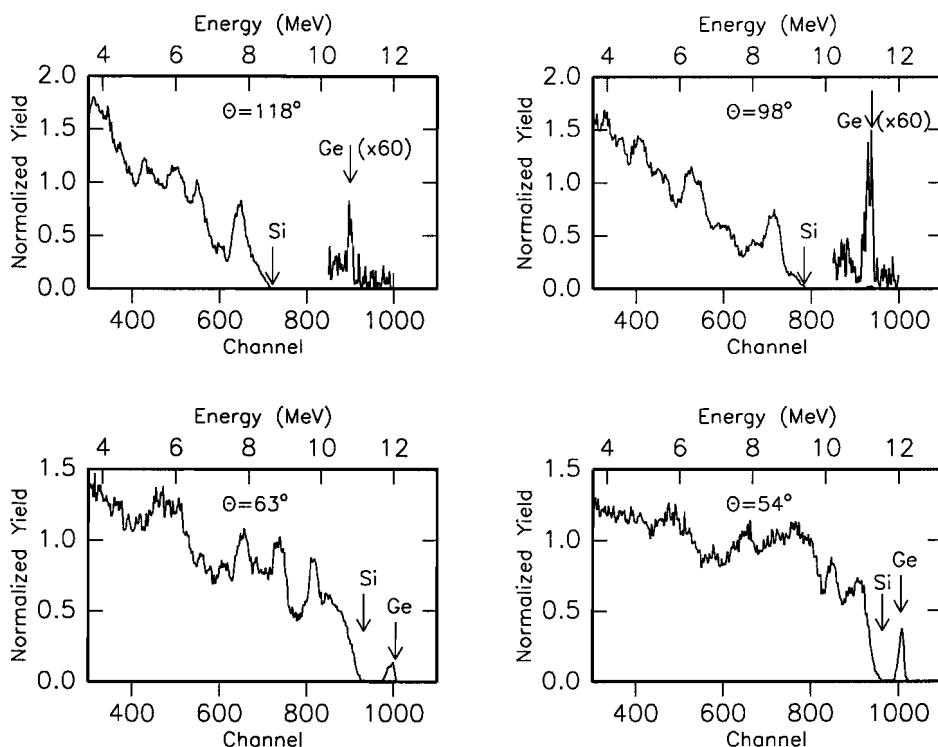


**Figure 4.2:** Energy spectra measured at different backscattering angles:  $\theta=118^\circ$ ,  $\theta=98^\circ$ ,  $\theta=63^\circ$  and  $\theta=54^\circ$ . The silicon surface edge and the germanium peak are indicated in the spectra. Germanium yield is magnified by a factor of 60 for  $\theta=118^\circ$  and  $\theta=98^\circ$ . The germanium yield increases for more forward scattering angle. The separation of the germanium peak from the silicon surface edge is reduced for more forward scattering angles. Overlap starts for  $\theta \approx 50^\circ$ .

In order to circumvent background subtraction procedures a separation of the germanium signal from the silicon edge is preferred. This separation is reduced when the SiGe film is not near the surface of the sample. Depending on the composition of the analyzed sample and the thickness of the capping layer a more backward scattering angle might be required. The preferential scattering geometry compromises between sufficient mass separation and sufficient count rate.

Figure 4.3 gives the measured angular dependence of the germanium scattering yield. The measured yield has been corrected for the linear background, originating from pile-up in the detector. The gain in germanium yield obtained for forward scattering is sufficient for the

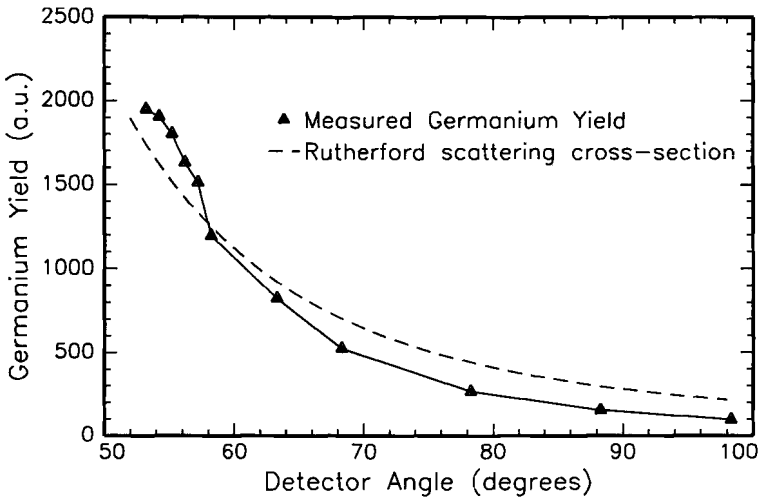


**Figure 4.3:** The filled triangles show the integrated germanium yield as a function of the scattering angle  $\theta$ . The position of the scanning window in the energy spectra differed with scattering angle. A more forward scattering angle results in an enhancement of the yield of more than one order of magnitude. The theoretical Rutherford behaviour is represented by the dashed curve.

acquisition of strain measurements on samples with composition and layer thicknesses close to that of the test sample.

Finally, the arguments for the choice of an off-normal crystallographic axis for angular scan analysis are considered. A maximum shift of the off-normal axis of interest is preferred to obtain a high sensitivity for the tetragonal distortion. Obviously, a maximum shift is found for the  $\langle 110 \rangle$  axis while the angular shifts of the  $\langle 111 \rangle$  and  $\langle 110 \rangle$  axes,  $\Delta\theta_{\langle 111 \rangle}$  and  $\Delta\theta_{\langle 110 \rangle}$ , differ by only 6% for a given tetragonal distortion. Furthermore, ion-steering effects can be suppressed when the shift, due to the tetragonal distortion, is large compared to the characteristic angle for channeling; i.e.  $\Delta\theta > \Psi_1$ . This consideration would favour the measurement of the  $\langle 111 \rangle$  axis since  $\Psi_{\langle 111 \rangle}$  ( $=0.21^\circ$ ) differs  $\sim 10\%$  from  $\Psi_{\langle 110 \rangle}$  ( $=0.23^\circ$ ). With respect to the germanium count rate from the  $\text{Si}_{1-x}\text{Ge}_x$  layer, measurement of the  $\langle 111 \rangle$  direction is preferred over the measurement of the  $\langle 110 \rangle$  direction. In our experiments angular scans through both main crystallographic directions,  $\langle 110 \rangle$  and  $\langle 111 \rangle$ , have been carried out. Strain measurements on heterostructures of  $\text{Si}_{1-x}\text{Ge}_x$  with the germanium content between 0.05 and 0.25 are presented in the next sections. Both samples with SiGe strained capping layers and samples with strained

SiGe buried layers are subject of the study. We successfully determined the tetragonal distortion of a *buried*  $\text{Si}_{1-x}\text{Ge}_x$  layer with  $x=0.175$ .

#### 4.4 Coherency strain in a hetero-epitaxial $\text{Si}_{1-x}\text{Ge}_x$ ( $x=0.05$ ) top layer grown on silicon(100)

Strain analysis with 12.6 MeV  $\text{He}^{++}$  ions has been applied to an epitaxial  $\text{Si}_{1-x}\text{Ge}_x/\text{Si}$  structure ( $x=0.05$ ). The 550 nm compressively strained  $\text{Si}_{1-x}\text{Ge}_x$  top layer ( $t_c > 1000$  nm [23]) was grown in an APCVD reactor on 6 inch Si (100) wafers. For the strain analysis with the ion beam a  $1 \text{ cm}^2$  area had been cut from the wafer. The beam current used in the experiment was 4 nA and the

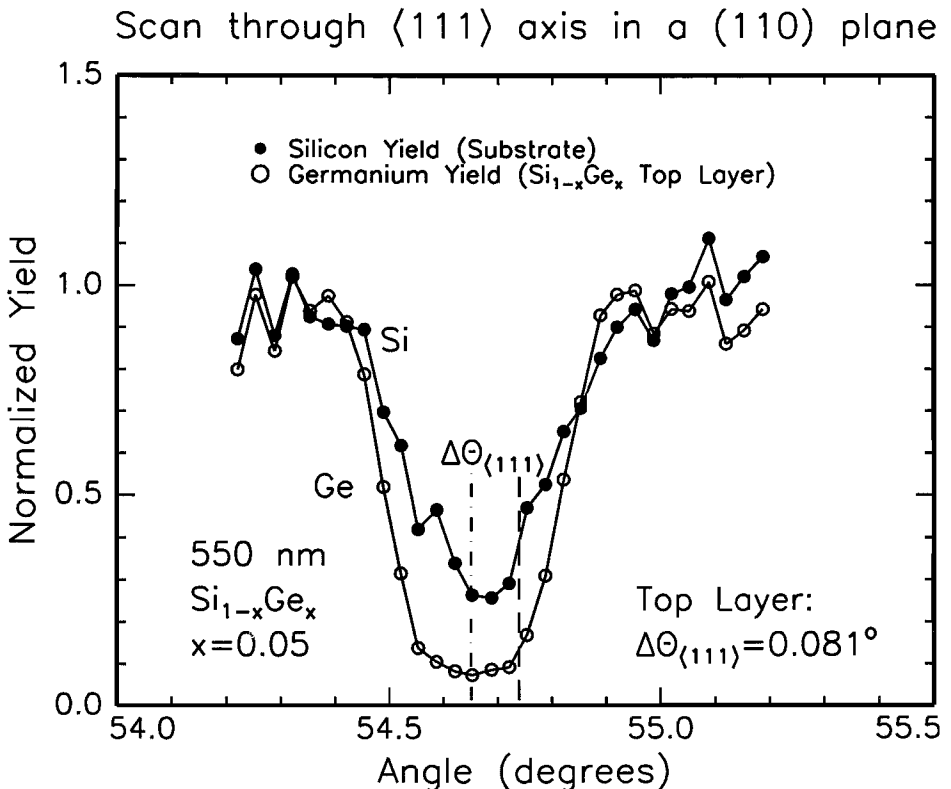


**Figure 4.4:** Scattering yield as a function of sample rotation angle measured with respect to the  $\langle 100 \rangle$  axis through the  $\langle 111 \rangle$  axis in a  $(110)$  plane. Angular scans of the germanium yield from the  $\text{Si}_{1-x}\text{Ge}_x$  film (open circles) and the silicon yield from the substrate (filled circles). The analyzed sample is a 550 nm strained  $\text{Si}_{1-x}\text{Ge}_x$  film ( $x=0.05$ ) grown on a silicon (100) substrate. The strain in the layer is determined from the measured kink angle,  $\Delta\theta_{\langle 111 \rangle}$ .

maximum angular spread of the incident beam was better than 0.07°. The sample was mounted on the 3-axis goniometer and aligned with respect to the incident ion beam. The position of the [100] crystalline direction of the substrate was determined from an angular scan in the (110) plane across the <100> channel, using a backscattering angle of 110°. The target orientation was determined with respect to the position of the <100> minimum. In order to determine the strain inside the Si<sub>1-x</sub>Ge<sub>x</sub> top layer the detector was moved to a scattering angle of 54°, providing sufficient germanium yield. The Ge angular scan was measured in the (110) plane across the <111> substrate axis, for which  $\theta=54.736^\circ$ . Both the <100> and the <111> angular scans have been acquired in the same scan direction of the goniometer to eliminate possible hysteresis effects.

Figure 4.4 shows the <111> Si and Ge angular scans obtained from 30 energy spectra, measured for 5 minutes each, using intervals of 0.033°. The angular position,  $\theta$ , is measured with respect to the position of the <100> axis. Normalization has been carried out with respect to the silicon and germanium yield of an azimuthally averaged energy spectrum. The location of the <111> crystalline axis of the Si<sub>1-x</sub>Ge<sub>x</sub> top layer is determined from the position of the minimum germanium scattering yield:  $\theta_{\langle 111 \rangle} = 54.655^\circ \pm 0.005^\circ$ . This implies an angular shift of the <111> axial direction of  $\Delta\theta_{\langle 111 \rangle} = 0.081^\circ \pm 0.005^\circ$  with respect to the position of the <111> crystalline axis of a cubic crystal. This angular shift corresponds to a tetragonal distortion of the Si<sub>1-x</sub>Ge<sub>x</sub> top layer of  $\epsilon_T = 0.30 \pm 0.02\%$ . The average perpendicular lattice constant of the commensurate grown compressively strained Si<sub>1-x</sub>Ge<sub>x</sub> layer is  $a_\perp = 0.5447 \pm 0.0001$  nm.

The location of the silicon minimum yield, which is assigned to the substrate, was determined as  $\theta = 54.68^\circ \pm 0.01^\circ$ . This value differs significantly from the location of the <111> axis (54.736°) of a cubic crystal and might point to ion steering at the SiGe/Si interface. The asymmetrical shape of the angular scan also indicates steering of channeled ions from the top layer into the channel of the silicon substrate. Steering can occur since the kink angle is small with respect to the characteristic angle for channeling,  $\Psi_{1\langle 111 \rangle}$ . Determination of the kink angle  $\Delta\theta$  with respect to the <111> direction of the substrate thus results in an underestimation of the kink angle and an underestimation of the strain. Steering effects also limit reliable and accurate

determination of the strain of buried layers, especially in cases where the kink angle is of the order of the critical angle for channeling. The experiment shows that the use of 12.6 MeV  $\text{He}^{++}$  ions enables determination of the tetragonal distortion of a strained  $\text{Si}_{1-x}\text{Ge}_x$  top layer with an accuracy of  $2 \times 10^{-4}$ . This is comparable with the accuracy obtained with glancing angle X-ray diffraction. The next step in the characterization of  $\text{Si}_{1-x}\text{Ge}_x$  strained layers is the study of the limitations in the analysis of a *buried* layer. In that case steering effects occur at two interfaces which affects the scans of Ge and the substrate scans.

#### 4.5 Coherency strain in a hetero-epitaxial $\text{Si}_{1-x}\text{Ge}_x$ ( $x=0.25$ ) buried layer

The strain of an epitaxial  $\text{Si}_{1-x}\text{Ge}_x$  *buried layer* has been determined in a 12.6 MeV  $\text{He}^{++}$  ion channeling experiment to determine the accuracy for strain measurements. Deposition of the heterostructure was performed with the MBE system at Philips Research Laboratories [24]. A thermally cleaned Si(100) substrate was capped with an epitaxially grown Si buffer layer to obtain a clean atomically smooth surface. Subsequently a 120 nm  $\text{Si}_{1-x}\text{Ge}_x$  ( $x=0.25$ ) layer was grown which was then capped with a 120 nm thick Si capping layer. Straightforward determination of the tetragonal distortion  $\epsilon_T$  from the angular positions of the  $\langle 111 \rangle$  and  $\langle 110 \rangle$  germanium minimum yield was carried out since the characteristic angle for channeling,  $\Psi_1$ , is smaller than the kink angle  $\Delta\theta$  at the Si/ $\text{Si}_{1-x}\text{Ge}_x$  ( $x=0.25$ ) interfaces according to the theory of bulk elasticity ( $\Delta\theta_{\langle 110 \rangle} = 0.53^\circ$ ,  $\Psi_{1\langle 110 \rangle} = 0.23^\circ$  and  $\Delta\theta_{\langle 111 \rangle} = 0.50^\circ$ ,  $\Psi_{1\langle 111 \rangle} = 0.21^\circ$ ). The locations of the  $\langle 110 \rangle$  and  $\langle 111 \rangle$  off-normal axes are determined with respect to the normal  $\langle 100 \rangle$  direction.

The measurements have been acquired with the detector located at a  $60^\circ$  forward scattering angle. As discussed in section 4.3, the choice of this geometry compromises between an enhanced germanium signal and sufficient mass separation of the silicon and germanium signal. Normalization of the scattering yield was carried out with respect to the azimuthally averaged spectrum. The typical beam current was 4 nA and the corresponding maximum angular spread of the incident ion beam was smaller than  $0.07^\circ$ . Figure 4.5 depicts the integrated Ge signal in the (100) plane across the  $\langle 110 \rangle$  channel and in the (110) plane across the  $\langle 111 \rangle$  channel. The angle  $\theta$  is with respect to the [100] axis, near the surface normal. The germanium  $\langle 110 \rangle$  and



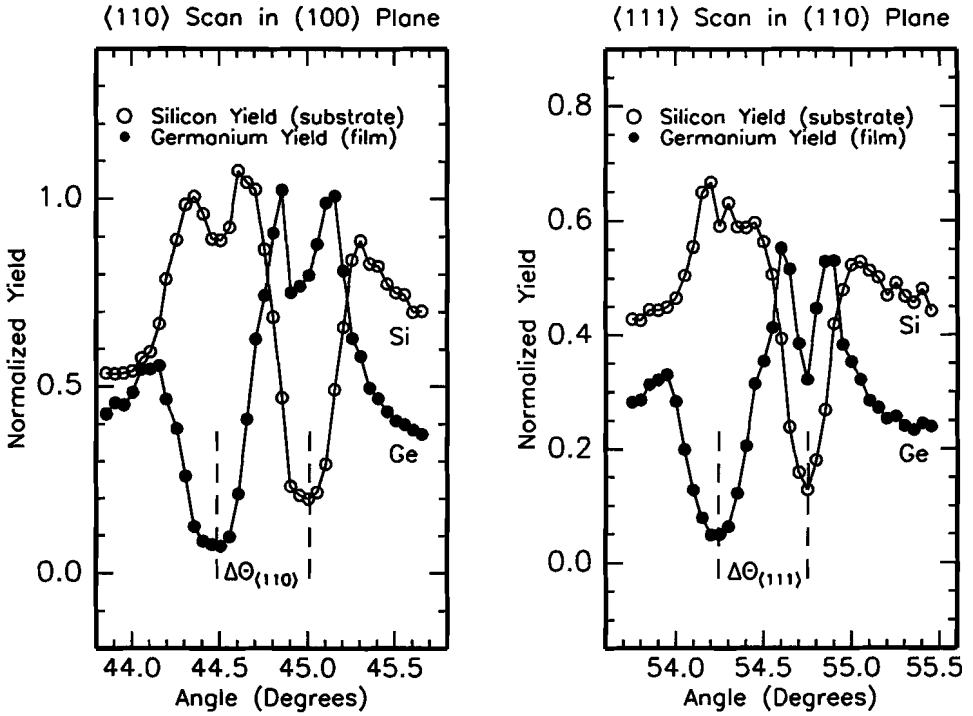


**Figure 4.5:** Normalized scattering yields as a function of sample rotation angle have been measured with respect to the  $\langle 100 \rangle$  axis. Angular scans through the  $\langle 110 \rangle$  axis in the  $(100)$  plane and through the  $\langle 111 \rangle$  axis in the  $(110)$  plane are obtained from setting an energy window on the germanium peak in the 37 measured energy spectra. The analyzed sample is a commensurate 120 nm  $\text{Si}_{1-x}\text{Ge}_x$  layer ( $x=0.25$ ) capped with a 120 nm silicon top layer. Scans of the germanium yield from the film (filled circles) and the silicon yield from the substrate (open circles) are depicted. The strain in the film is determined from the measured kink angles indicated in the figure as  $\Delta\theta_{\langle 111 \rangle}$  and  $\Delta\theta_{\langle 110 \rangle}$ .

$\langle 111 \rangle$  scans are shifted with respect to the location of the  $\langle 110 \rangle$  and  $\langle 111 \rangle$  scans for a cubic crystal. The angular shifts of the germanium minimum yield are  $\Delta\theta_{\langle 110 \rangle} = 0.511^\circ \pm 0.005^\circ$  and  $\Delta\theta_{\langle 111 \rangle} = 0.510^\circ \pm 0.004^\circ$ . The tetragonal distortion in the layer, derived from these values, is  $\epsilon_{T\langle 110 \rangle} = 1.78 \pm 0.02\%$  and  $\epsilon_{T\langle 111 \rangle} = 1.89 \pm 0.02\%$ , respectively. In spite of the accuracy of the goniometer which allows to determine the position of the scan within  $0.005^\circ$  this results in a tetragonal distortion which is different for the  $\langle 110 \rangle$  and the  $\langle 111 \rangle$  axes by 0.1%. Apparently, other experimental uncertainties such as ion steering limit the accuracy of the determined strain to  $\epsilon_T = 1.84 \pm 0.07\%$ . This corresponds with an average perpendicular lattice constant of the

compressively strained  $\text{Si}_{1-x}\text{Ge}_x$  layer of  $a_x=0.5531\pm 0.0003$  nm.

The germanium angular scans show a decreased scattering yield at the location of the silicon  $\langle 110 \rangle$  and  $\langle 111 \rangle$  minima, flanked by two small peaks. This local minimum is explained by the phenomenon that axially channeled ions in the silicon top layer are steered into the (100) and (110) planes at the  $\text{Si}/\text{Si}_{1-x}\text{Ge}_x$  interface. The ions remain channeled which reduces the probability for scattering from atoms in this buried layer. Steering only concerns ions with small initial transverse kinetic energy. Those ions that remain channeled in the top layer but have relatively high transverse kinetic energy dechannel at the  $\text{Si}/\text{Si}_{1-x}\text{Ge}_x$  interface, since planar channeling further restricts the magnitude of the transverse kinetic energy of the ions. This results in an increased scattering probability for ions from atoms in the strained layer, thus for the germanium scattering yield. This is observed in the germanium angular scan as two small peaks flanking the sub-minimum. The  $\langle 110 \rangle$  silicon substrate scan shows a similar local minimum at the location of the germanium  $\langle 110 \rangle$  minimum, flanked by two peaks.

The Si yield, shown in figure 4.5, originates from a spectral interval of the silicon scattering yield, just below the silicon surface peak. The  $\langle 110 \rangle$  and  $\langle 111 \rangle$  minima of these scans are located at the positions presumed for a cubic crystal. This suggests that steering effects in the top layers do not introduce a significant shift of the substrate minimum in contrast to the case of the Si substrate in combination with the  $\text{Si}_{1-x}\text{Ge}_x$  top layer with  $x=0.05$ .

#### 4.6 Coherency strain in a hetero-epitaxial $\text{Si}_{1-x}\text{Ge}_x$ ( $x=0.175$ ) buried layer

The straightforward interpretation of the measured angular shift of an off-normal crystalline axis to obtain the tetragonal distortion  $\epsilon_T$  of an epitaxial layer is not applicable for buried layers in the case that  $\Delta\theta$  is of the order of the characteristic angle for channeling. Steering effects on the interface of the capping layer and the strained layer may result in asymmetrical scans or an extra shift of the minimum scattering yield of an element in the strained layer. In order to investigate these effects, a buried  $\text{Si}_{1-x}\text{Ge}_x$  strained layer has been analyzed using two different ion energies, 4 MeV  $\text{He}^+$  and 12.6 MeV  $\text{He}^{++}$ . The coherency strain of this buried layer has been determined from the measured  $\langle 110 \rangle$  angular scans. The characterized sample is a strained buried  $\text{Si}_{1-x}\text{Ge}_x$ .

layer ( $x=0.175$ ) with a thickness of 65 nm, capped with a 61 nm epitaxial Si layer. The sample was grown on a Si(100) wafer by Atmospheric Pressure Chemical Vapour Deposition (APCVD) at Philips Research Laboratories in Eindhoven. Interpretation of these angular scans was performed with help of Monte Carlo ion trajectory calculations which provided a detailed agreement of the estimated angular scans.

Angular scans have been measured using the 900 mm<sup>2</sup> detector positioned at a backscattering

### Germanium $\langle 110 \rangle$ Scans in $(100)$ Plane

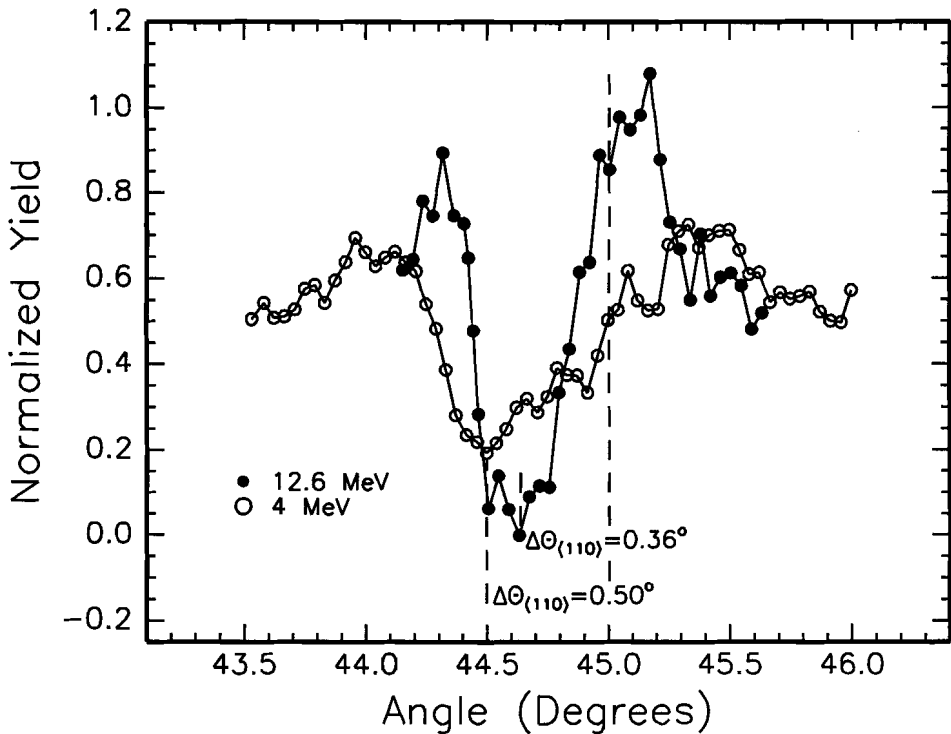


**Figure 4.6:** Normalized angular scans through the  $\langle 110 \rangle$  direction in the  $(100)$  plane obtained from a  $\text{Si}_{1-x}\text{Ge}_x$  buried strained layer ( $x=0.175$ ). Scans are obtained from setting an energy window on the germanium peak. Incident ions are 4 MeV  $\text{He}^+$  (open circles) and 12.6 MeV  $\text{He}^{++}$  (filled circles) respectively. The 4 MeV experiment suggests a larger kink angle due to the asymmetrical shape of the scan as a result of steering effects at the  $\text{Si}/\text{Si}_{1-x}\text{Ge}_x$  interface. These effects are suppressed when high-energy 12.6 MeV  $\text{He}^{++}$  incident ions are used due to the smaller characteristic angle for channeling for these ions.

angle of  $98^\circ$ . This detector position serves to measure both the  $\langle 100 \rangle$  and  $\langle 110 \rangle$  angular scans in the (100) plane. The sample rotation angle  $\theta$  is then measured with respect to the [100] axis which is close to the surface normal. The scattering yield in the  $\langle 110 \rangle$  scans is normalized to the scattering yield obtained from an azimuthally averaged direction. Figure 4.6 depicts the measured  $\langle 110 \rangle$  germanium angular scans. From the 4 MeV experiment the germanium yield has been obtained from 60 energy spectra, measured 90 seconds each. The angular shift with respect to  $45^\circ$  is obtained from the location of the germanium  $\langle 110 \rangle$  minimum and is  $\Delta\theta = 0.50^\circ \pm 0.02^\circ$ . The experiment has been repeated using a 12.6 MeV  $\text{He}^{++}$  beam. The  $\langle 110 \rangle$  germanium angular scan is obtained from 38 energy spectra, measured for 5 minutes each. In order to obtain a correct scan a linear background subtraction procedure for the germanium yield was necessary. The angular shift with respect to  $45^\circ$  has been determined from the location of the germanium minimum yield of the  $\langle 110 \rangle$  angular scan and results in  $\Delta\theta = 0.36^\circ \pm 0.02^\circ$ .

The decreased width of the angular scan obtained with 12.6 MeV ions is clearly visible. Note that the measured angular shift using 12.6 MeV ions differs significantly from the value found with the 4 MeV ion beam. This is indeed due to steering effects regarding the asymmetrical shape of the scan obtained with 4 MeV ions. The 12.6 MeV scan also shows an asymmetrical shape and shows an enhanced yield at  $45^\circ$ , but due to the small characteristic angle the effect is minimized and does not cause an extra shift of the minimum yield. The enhanced yield is the result of enhanced scattering of ions that were channeled in the top layer and which are steered on the SiGe strings of the strained buried layer. The measured 12.6 MeV angular scans have been simulated with MC ion trajectory simulations to determine the strain in the buried layer more accurately, as discussed below.

#### 4.7 Angular-scan simulations with Monte Carlo trajectory calculations

Simulations have been carried out with the Monte Carlo program LAROSE [25]. This program offers the feature for the simulation of angular scans and allows a detailed study of the shape of the measured angular scans. Comparison of measurements and simulations allows to enhance the accuracy in the interpretation of angular scans. The program treats ion-atom interactions as binary collisions and uses the repulsive Coulomb force. In case the ion approaches the atom

sufficiently close a large-angle scattering event or nuclear reaction can occur. This close-encounter probability can be extracted from the program. Considering the fundamental approach of trajectory simulations the program also treats the steering effects at the interfaces of the films. The input parameters used in LAROSE are: ion energy (12.6 MeV), layer thicknesses (450 atomic layers = 65 nm) for both capping and buried layer, FWHM of the beam divergence ( $\Delta=0.07^\circ$ ), composition of the strained  $\text{Si}_{1-x}\text{Ge}_x$  layer ( $x=0.175$ ) and the kink angle ( $\Delta\theta$ ) of the  $\langle 110 \rangle$  channel of the strained layer with respect to the  $\langle 110 \rangle$  channel of the substrate. These parameters are used to calculate the close encounter probability of ions with the atoms for each

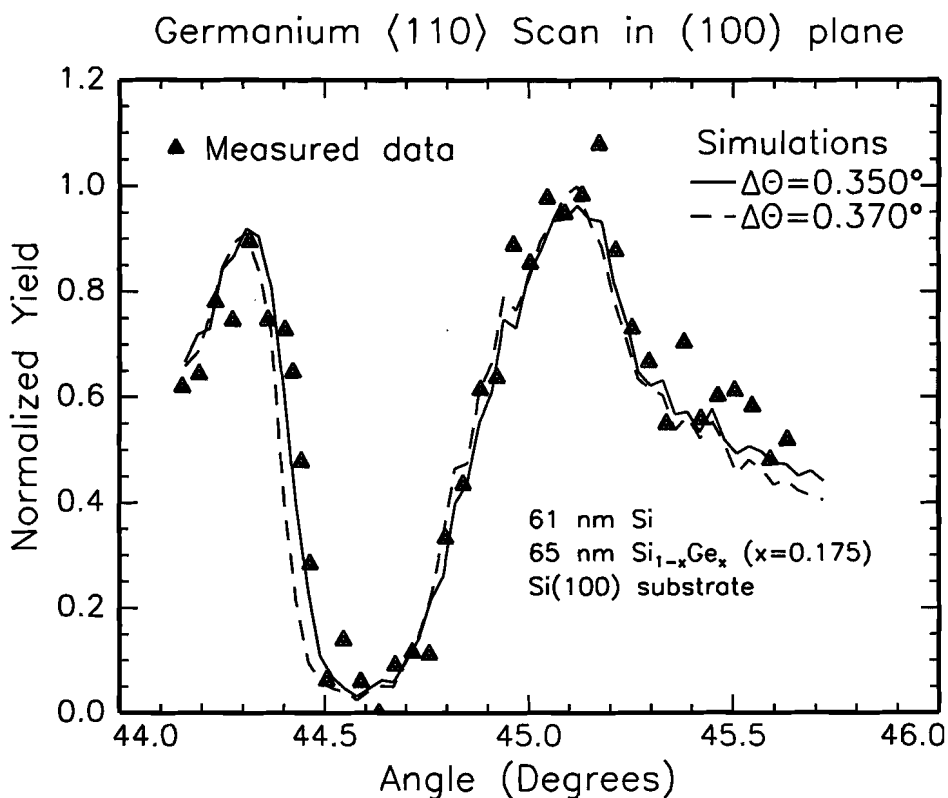


**Figure 4.7:** Measured germanium yield and LAROSE Monte-Carlo simulations of the  $\langle 110 \rangle$  angular scan obtained from the close-encounter probability in the buried  $\text{Si}_{1-x}\text{Ge}_x$  layer. Depicted simulations have been calculated using different kink angles:  $\Delta\theta=0.350^\circ$  (full curve) and  $\Delta\theta=0.370^\circ$  (dashed curve). A detailed resemblance with the measured scan is obtained for a kink angle of  $\Delta\theta=0.350^\circ$ .

defined layer. The simulated angular scans determine the close-encounter probability as a function of the sample orientation with respect to the incident ion beam. Full agreement of the simulated scans with the measured scans was aspired. The kink angle  $\Delta\theta$  has been obtained from the input parameters of the simulation that shows the best resemblance with the measured scan. In order to provide a detailed agreement of the simulations with the experiment a rectangular angular distribution for the beam divergence was implemented in the program. This distribution is an equal contribution of all incident angles between  $-\frac{1}{2}\Delta$  and  $\frac{1}{2}\Delta$  with respect to the main beam direction, where  $\Delta$  is referred to as the maximum angular spread. This distribution agrees better with the angular distribution used in the experiment and differs from the Gaussian angular distribution which is used as default in the program.

In order to match the measured profile, many simulations have been carried out with different kink angles. Figure 4.7 depicts the 12.6 MeV measured data points, represented by filled triangles, together with two angular-scan simulations, represented by the full and dashed curves. The shown simulations have been obtained using kink angles of  $\Delta\theta=0.350^\circ$  and  $\Delta\theta=0.370^\circ$ , respectively. The simulation with  $\Delta\theta=0.350^\circ$  resembles closely the experimental data. The difference between the kink angles of the simulated scans is taken as a measure for the accuracy.

The tetragonal distortion is calculated from the geometrical kink angle ( $\Delta\theta=0.350^\circ$ ) using equation 4.3 and yields:  $\epsilon_{\tau}=1.26\pm 0.04\%$ . Subsequently the perpendicular lattice constant of the strained layer was calculated:  $a_{\perp}=0.5498$  nm for  $\Delta\theta=0.350^\circ$  and  $a_{\perp}=0.5502$  nm for  $\Delta\theta=0.370^\circ$ . Apparently the perpendicular lattice constant of the buried layer can be determined with an accuracy of 0.0004 nm. This accuracy is comparable with the accuracy achieved with glancing angle X-ray diffraction.

For utilisation of many simulations in routine measurements this method is very time consuming. Simulation of one angular scan took 2 hours on a DEC AXP 3300, equipped with 98 Mbyte of DRAM. Furthermore, experimental parameters such as beam divergence, orientation of the crystal with respect to the incident beam and the sample composition and thicknesses of both the capping layer and the strained layer need to be known accurately. These properties are used in

the MC calculations and are obtained either from the MBE or APCVD growth menu or from RBS analysis. Acquisition of reliable experimental data requires careful control of experimental parameters conscientious beam handling and precise target orientation. The accuracy for strain analysis using ion beams is claimed to be  $7 \times 10^{-4}$  for 2 MeV ions and is further improved to  $4 \times 10^{-4}$  when 12.6 MeV high-energy ions are used. The systematic error in the straightforward determination of the coherency strain from the measured kink angle is  $0.15^\circ$  when using 4 MeV He<sup>+</sup> ions. This error is reduced to  $0.01^\circ$  in case 12.6 MeV ions are used. Further improvement of the accuracy is obtained when comparison with simulations is accomplished.

#### **4.8 Beam-induced strain relaxation**

An important question concerning the accuracy of strain determination with ion beam analysis involves a possible effect of the incident ion beam on strain relaxation of a meta-stable epitaxially grown layer. In literature some controversy about this necessity is reported. Mantl et al. [12] determined the strain of magnetic superlattices by ion channeling and found that after an accumulated dose of  $1 \times 10^{17}$  He cm<sup>-2</sup> no significant relaxation was noted. However, Pan et al. [26] did notice strain relaxation of the order of 50%, using X-ray rocking-curve analysis on GaSb/AlSb strained layer superlattices, which had been analyzed with RBS channeling before. They mentioned extensive bombardment in RBS test runs but did not quantify the accumulated ion dose.

In order to study the effect of the ion beam on strain relaxation the strain of the buried Si<sub>1-x</sub>Ge<sub>x</sub> (x=0.175) layer was determined on two different spots of the sample. One spot had been irradiated in previous experiments with a cumulative dose of 1.6 mC, with high-energy 4 MeV He<sup>+</sup> and 12.6 MeV He<sup>++</sup> ions. A typical beam spot size on the sample of 2x2 mm<sup>2</sup> is used in these experiments which implies a cumulative incident ion flux of  $2 \times 10^{17}$  cm<sup>-2</sup>. The second spot was a fresh spot on the sample which had not been irradiated before. Figure 4.8 depicts two successive <110> angular scans of the silicon substrate yield and of the germanium scattering yield. Fortunately there is no visible or measurable shift of the scans nor an increase of the minimum yield of the previously irradiated spot with respect to the fresh spot. This indicates that no significant strain relaxation has been noticed. Conclusively we claim that a necessity for the

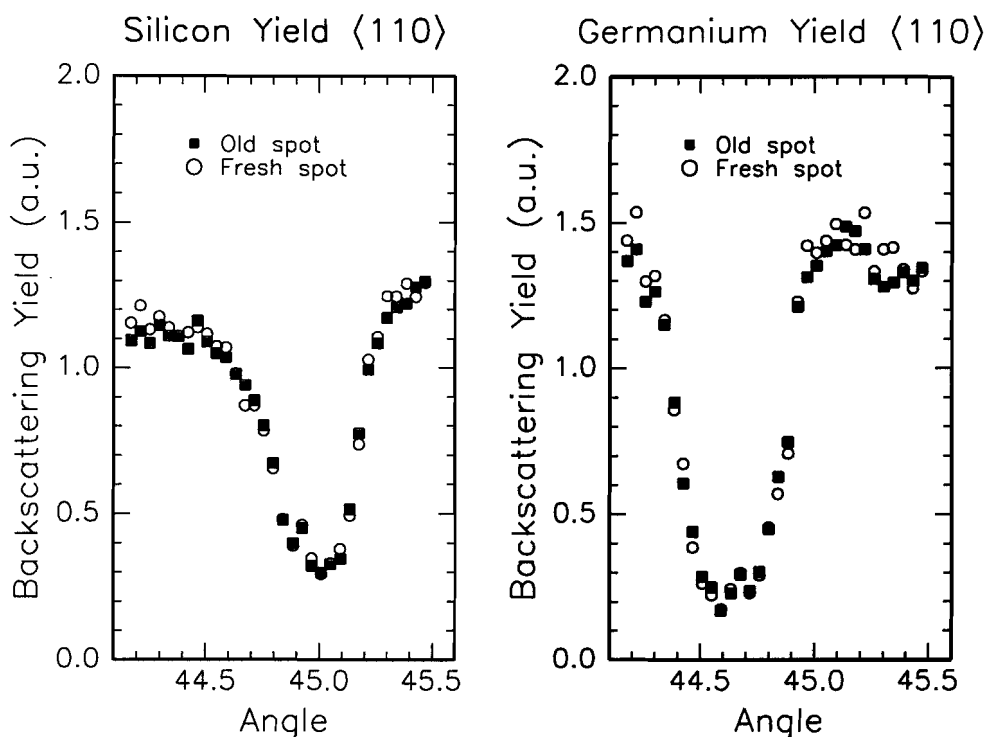


**Figure 4.8:** The  $\langle 110 \rangle$  angular scans obtained from strain measurement on a fresh spot and on a previously irradiated spot on the sample with an ion flux of  $2 \times 10^{17} \text{ cm}^{-2}$ . No significant shift of the germanium scan nor an increase of the minimum yield is noticed. This implies that there is no strain relaxation and that induced structural damage to the strained layer is below the detection limit.

movement to a fresh spot on the target is not essential in these experiments and the same sample can be analyzed with different beam energies without sensitivity loss due to damaging.

## 4.9 Conclusions

The straightforward determination of strain in single-layer  $\text{Si}_{1-x}\text{Ge}_x$  heterostructures has been achieved using 12.6 MeV ions, taking advantage of the small characteristic angle. Analysis of buried  $\text{Si}_{1-x}\text{Ge}_x$  layers with 4 MeV and 12.6 MeV ions confirmed the advantage of the use of higher energies and the reduction of steering effects at the interfaces at the higher energies. Optimisation of the target scattering geometry and the detector position is necessary to obtain sufficient statistics in the angular scans. Obtained results show that it is recommended not to use



even higher ion energies (e.g. 25 MeV) for the characterisation of the SiGe layers since the cross-section for elastic scattering from germanium at 60 degrees becomes non-Rutherford at approximately 12.6 MeV, when adopting the model of Bozoian. Resonant scattering cross-sections that occur for higher energies are not available in literature and might be subject for further study. The use of 12.6 MeV high-energy ions improves the accuracy in the determination of the kink angle towards  $0.01^\circ$  as obtained for analysis of a buried Si<sub>1-x</sub>Ge<sub>x</sub> (x=0.175) layer of 65 nm thickness. This angular accuracy corresponds with an accuracy of  $4 \times 10^{-4}$  in the determination of the tetragonal distortion and 0.0004 nm for the determination of the perpendicular lattice constant. Additional ion MC trajectory calculations give a detailed match of the simulated angular scans with the measured angular scans and enhances the accuracy further towards  $2 \times 10^{-4}$ . Ion-beam induced strain relaxation was not observed for cumulative ion fluxes up to  $2 \times 10^{17}$  cm<sup>-2</sup>. This confirms the observation of Mantl et al. who characterized magnetic superlattices and did not observe any strain relaxation. This could imply that this value can be generalized for samples of different composition. More applications of high-energy ion channeling are presented in chapter 5.

## References

1. S.T. Picraux, W.K. Chu, W.R. Allen and J.A. Ellison. Nucl. Instr. and Meth. B15 (1986) 306.
2. A.T. Fiory, J.C. Bean, L.C. Feldman, and I.K. Robinson. J. Appl. Phys. 56 (1984) 1227.
3. S. Hashimoto, J.L. Peng, W.M. Gibson, L.J. Schowalter and R.W. Fathauer, Appl. Phys. Lett. 47 (1985) 1071.
4. M. Okamoto, S. Hashimoto, B.D. Hunt, L.J. Schowalter and W.M. Gibson, Mat. Res. Soc. Symp. Proc. 56 (1986) 157.
5. G. Burns, C.R. Wie, F.H. Dacol, G.D. Petit and J.M. Woodall, Appl. Phys. Lett. 51 (1987) 1919.
6. E. Anastassakis, NATO ASI Vol. 283, *Application of Particle and Laser Beams in Materials Technology*, (1995).
7. G. Bai and M.-A. Nicolet, J. Appl. Phys. 71 (1992) 4227.
8. G. Bai, M.-A. Nicolet, C.H. Chern and K.L. Wang, J. Appl. Phys. 75 (1994) 4475.

9. A.C. Diebold, S.W. Steinhauser and R.P. Mariella Jr., *J. Vac. Sci. Technol. B* 7 (1989) 365.
10. H. Aharoni, *Vacuum* 28 (1978) 571.
11. B. Holländer, R. Butz, and S. Mantl, *Phys. Rev. B* 46 (1992) 6975.
12. S. Mantl, Ch. Buchal, B. Strizker and B. Saftic, *Nucl. Instr. And Meth. B* 15 (1986) 314.
13. A.J. Durelli, E.A. Phillips and C.H. Tsao, *Introduction to the theoretical and experimental analysis of stress and strain*, McGraw-Hill, New York (1958)
14. K.-N Tu, J.W. Mayer, L.C. Feldman, *Electronic Thin Film Science for Electrical Engineers and Materials Scientists*, Maxwell Macmillian Int. New York, NY, 1992.
15. J.Y. Tsao, *Materials Fundamentals of Molecular Beam Epitaxy*, Academic Press, San Diego CA, 1992.
16. J.W. Matthews and A.E. Blakeslee, *J. Cryst. Growth* 27 (1974) 118.
17. D.C. Houghton, C.J. Gibbings, C.G. Tuppen, M.H. Lyons and M.A.G. Halliwell, *Appl. Phys. Lett.* 56 (1990) 460.
18. J.C. Bean, L.C. Feldman, A.T. Fiory, S. Nakahara and I.K. Robinson, *J. Vac. Sci. Technol. A* 2 (1984) 436.
19. J.H. van der Merwe and C.A.B. Ball, in *Epitaxial Growth*, edited by J. Matthews (Academic, New York, 1975), Part b.
20. W.K. Chu, J.W. Mayer and M.A. Nicolet, *Backscattering Spectrometry* (Academic London, 1978)
21. M. Bozoian, *Nucl. Instr. and Meth. B* 58 (1991) 127.
22. P.W.L. van Dijk, L.J. van IJzendoorn and M.J.A. de Voigt, *Nucl. Instr. and Meth. B* 118 (1996) 97.
23. A.T. Fiory, J.C. Bean, L.C. Feldman and I.K. Robinson, *J. Appl. Phys.* 56 (1984) 1227.
24. L.J. van IJzendoorn, G.F.A. van de Walle, A.A. van Gorkum, A.M.L. Theunissen, R.A. van den Heuvel and J.H. Barrett, *Nucl. Instr. And Meth. B* 50 (1990) 127.
25. J.H. Barrett, *Phys. Rev. B* 3 (1971) 1527.
26. C.K. Pan, D.C. Zheng, T.G. Finstad, W.K. Chu, V.S. Speriosu, M.-A. Nicolet and J.H. Barrett, *Phys. Rev. B* 31 (1985) 1270.

# 5

## Applications of high-energy ion channeling

*The study of crystal defects [1] and quantification of defect formation introduced by keV heavy-ion implantation [2] were some of the early applications of MeV-ion channeling in materials characterisation. The ion-channeling technique has shown to be a valuable tool that gives detailed information on the amount and the depth distribution of defects. The possibility for reliable quantification makes it an effective tool to study annealing kinetics of disorder. Moreover, the distinction between different types of defects is possible with ion channeling. Applications presented in this chapter focus on the advantages of high-energy ion channeling for defect depth profiling. The main advantage is the large depth interval that can be analyzed when high-energy ions are used. The accuracy, sensitivity and detection limits for defect analysis will be discussed in section 5.2 where the number of defects in a 4  $\mu\text{m}$  thick SiGe multi-layered structure is determined.*

*Section 5.3 treats the characterization of  $\text{Si}_{1-x}\text{Ge}_x\text{C}_y$  strained layers. The aim was defect free growth of epitaxial  $\text{Si}_{1-x}\text{Ge}_x\text{C}_y$  films with up to 2.0% C and 20% Ge. Incorporation of carbon in the meta-stable SiGe film will diminish the accommodated strain which results in a more stable thin film. A correlation is thus expected between the present strain in the film and the carbon fraction in case the carbon atoms occupy substitutional sites in the lattice. The crystalline quality of the grown structures is determined in a 4 MeV RBS channeling experiment. The tetragonal distortion of the films has been measured with channeling using 12.6 MeV  $\text{He}^{++}$  ions. A third structure of interest is a buried strained InGaAs grown on a GaAs substrate which is of interest for the development of high-mobility field-effect transistors (HFET). A plasma treatment is part of the fabrication process of the HFET. The plasma treated samples showed a decreased charge carrier mobility. Ion channeling with 4 MeV  $\text{He}^+$  has been carried out to study the effect of the plasma treatment on the strain of the InGaAs layer and the crystalline damage in the heterostructure. The results are presented in section 5.4. Section 5.5 will summarize conclusions. First a brief introduction of the theory of damage creation and defect detection will be presented.*

## 5.1 Theory of defect analysis

The number and type of defects in the near surface region of a crystalline sample can be derived from the measured aligned scattering yield in an RBS channeling experiment [3]. The channeled ions have gentle collisions with the atomic strings and occasionally contribute to large-angle scattering. The scattering yield in the aligned spectrum is a measure of the dechanneled fraction of the ion beam. When the spectrum is compared to the random spectrum, the defect density can be derived from the ratio of channeled to random yield ( $y_{\text{chan}}/y_{\text{rand}}$ ). The theory describes the interaction of the ions with the crystal qualitatively in terms of channeled and dechanneled ions. In a virgin crystal ions can remain channeled or dechannel due to interaction with the vibrating atoms in the atomic strings. In a crystal with little disorder or small amounts of defects, ions can scatter directly from an interstitial atom, or dechannel due to the presence of crystalline imperfections or stacking faults which deteriorate the ions from their channeled precedence. As a result the dechanneled fraction increases which results in an enhanced backscattering yield. The magnitude of the increased backscattering yield depends on the types of defects and their dechanneling factors, i.e. the number of defects and their depth distribution. A detailed calculation of the number of defects from the measured increased scattering yield is given by Feldman, Mayer and Picraux [4]. The measured ratio of the channeled to random backscattering yield at a depth  $t$ ,  $\chi_d(t)$ , is compared to the ratio for a defect free (virgin) crystal which aligned fraction is denoted as  $\chi_v(t)$ . The difference between these ratios is related to the presence of defects that caused the enhanced dechanneling. The minimum yield is defined as:  $\chi_{\text{min}} = \chi_v(0)$ . The number of defects can be derived from the measured  $\chi_d(t)$  when the type of disorder or type of defect and its dechanneling factor,  $\sigma_d$ , are known. Previous treatments and calculations of the dechanneling factors corresponding to the types of dislocations are given by Quéré [5][6] and Picraux [7]. In case different types of defects are present in the crystal it is important to identify the dominant type of defect that contributes to the increased yield. In order to do this reliable dechanneling factors and defect densities need to be assumed in the calculation. The magnitude of the product of dechanneling factor and defect density determines the dominant defect type. Calculations show that the dechanneling factor for stacking faults or dislocation lines is significantly larger than for isolated interstitials. The energy dependence is expected to be  $E^0$  for stacking faults,  $E^{1/2}$  for dislocations, and  $E^{-1}$  to  $E^{-1/2}$  for point defects and defect clusters. In all our

experiments dealing with relaxation of strained layers, dechanneling from dislocation lines is assumed to be dominant and dechanneling induced by direct scattering from interstitials is neglected in first approximation.

Two types of dislocation lines can be considered: screw dislocations and edge dislocations. The dechanneling factor,  $\sigma_d$ , for a screw dislocation is inversely proportional to the half-width at half-minimum,  $\Psi_{1/2}$ , which is measured in an angular scan experiment. This suggests a higher sensitivity for the detection of these types of defects when higher ion energies are used. The magnitude of the dechanneling factor and its energy dependence are similar for screw dislocations and edge dislocations [8]. The dislocation density can be derived once the measured aligned yield, the measured random yield, the measured aligned yield in a virgin crystal and the dechanneling factor are known. When the increase of the dechanneling rate in a virgin crystal is small compared to the increment of the yield caused by dechanneling:  $d\chi_v(t)/dt \ll d\chi_d(t)/dt$  and  $\chi_v(t) \ll 1$ , the total disorder  $N_d(t)$  found between the surface and depth  $t$  is:

$$N_d(t) = \frac{1}{\sigma_d} \ln \left[ \frac{1 - \chi_v(t)}{1 - \chi_d(t)} \right] \quad 5.1$$

where  $\sigma_d$  is the dechanneling factor of the dominant defect. Note that the unit of  $N_d(t)$  depends on the nature of the defect. In case of line dislocations this is  $\text{cm}^{-1}$ , in case of point dislocations this is  $\text{cm}^{-2}$ . The virgin scattering ratio,  $\chi_v(t)$ , is assumed to be a constant fraction of the random yield,  $\chi_v(t) = K\chi_r(t)$ . The constant  $K$  is determined from the measured ratio in the channeled spectrum just behind the surface peak:  $K = \chi_d(0)$ .

## **5.2 Defect depth profiling of a 4 micron $\text{Si}_{1-x}\text{Ge}_x$ multi-layered structure**

Defect depth profiling with high-energy ion beams has been performed on a structure of seven freestanding, incommensurately grown  $\text{Si}_{1-x}\text{Ge}_x$  layers of approximately 470 nm thickness. The layers have been grown with increasing germanium fraction starting with  $x=0.02$ ,  $x=0.06$ ,  $x=0.10$ ,  $x=0.14$ ,  $x=0.18$  and  $x=0.22$  on a (100) oriented Si crystal. Subsequently a 740 nm relaxed layer of  $\text{Si}_{1-x}\text{Ge}_x$  ( $x=0.26$ ) was grown. On top of the relaxed  $\text{Si}_{1-x}\text{Ge}_x$  layer a 20 nm, tensile

strained, Si layer was grown. The structure was capped with an undoped 50 nm  $\text{Si}_{1-x}\text{Ge}_x$  ( $x=0.26$ ) layer and a Sb doped top layer serving as an electron donor. The layer thicknesses and compositions were obtained from the MBE growth menu provided by Philips Research Laboratories. The total thickness of the  $\text{Si}_{1-x}\text{Ge}_x$  layers, including the silicon strained layer, is approximately 4 microns. The morphology of the characterized structure is shown in figure 5.1.

The design of the analyzed structure is of interest in the fabrication of heterojunction Field Effect Transistors (FET) with high electron mobility. Epitaxial growth of a strained  $\text{Si}_{1-x}\text{Ge}_x$  layer on a Si substrate will result in the formation of a 2-D hole gas at the  $\text{Si}_{1-x}\text{Ge}_x/\text{Si}$  interface. Growth of a tensile strained silicon layer on a relaxed  $\text{Si}_{1-x}\text{Ge}_x$  substrate results in an offset in the conduction band and the formation of a 2-D electron gas at the  $\text{Si}_{1-x}\text{Ge}_x/\text{Si}$  interface. This 2-D electron gas has a high charge carrier mobility compared to a 2-D hole gas. The mobility of charge carriers is further enhanced when the contribution of impurity scattering of electrons from (remote) donor atoms and defect scattering are suppressed and reduced. This requires controlled growth of the relaxed structure in figure 5.1. Different kinds of defects can reduce the mobility of the charge carriers in the device. Point defects, dislocation lines, screw dislocations, stacking faults and mosaic spread in the structure should be located far from the electrically active layer. Defect profiling in the relaxed graded buffer layer on a silicon substrate is therefore of high importance to localise the defects and thereby optimise the electrical performance of the HFET's.

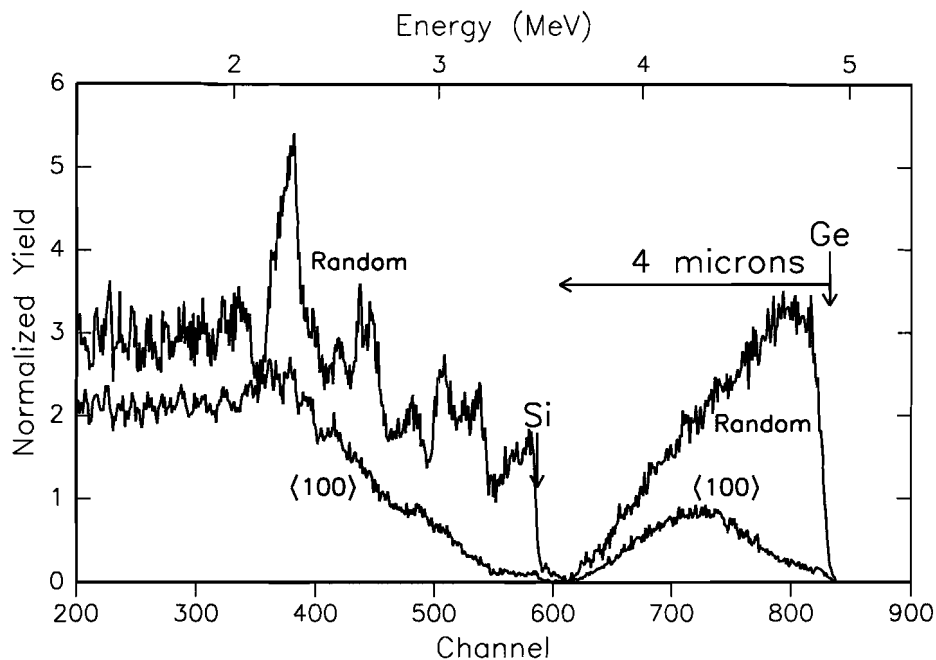
Commensurate growth of the tensile strained silicon layer requires an atomically smooth and defect-free relaxed SiGe surface with the aspired in-plane lattice constant since that determines the magnitude of the tetragonal distortion and the tensile strain in the silicon layer. This in-plane lattice constant is equal to the virtual lattice constant for a freestanding SiGe layer. TEM analysis on the morphology of structures grown at different conditions has shown a relaxed defect-free SiGe layer can be obtained when elevated growth temperatures ( $900^\circ\text{C}$ ) are used during growth. TEM analysis showed that the lowest defect density was obtained when relaxed layers of typical  $0.5\ \mu\text{m}$  thickness are grown with step-wise increasing germanium content. In that case dislocation lines are mainly localized at the layer interfaces to accommodate the difference in lattice constant of the neighboring layers [9]. The analyzed sample is a typical structure grown

under these conditions. Since the nature of the defects has been established with TEM the use of RBS combined with ion channeling offers the possibility to determine the depth distribution of defects quantitatively.

### **5.2.1 Experimental details**

In order to determine the damage depth profile of the 4 micron structure we used a 6 MeV He<sup>++</sup> beam and measured the backscattering yield at  $\theta=155^\circ$  with the beam aligned along the  $\langle 100 \rangle$  direction and compared this to the random spectrum. A typical beam current is 5 nA with a spot area of 4 mm<sup>2</sup>. The high energy (6 MeV) was selected to isolate the germanium peak in the backscattering spectrum from the silicon yield. Apart from the better energy separation of the surface peaks of silicon and germanium an increment of the incident ion energy results in a decreased stopping power of the ions. Use of 6 MeV He<sup>++</sup> allows depth profiling over more than 4  $\mu\text{m}$  while use of 2 MeV He<sup>++</sup> ions limits the depth of the analyzed profile to 900 nm which is definitely inadequate for characterization of the sample of interest. The energy resolution of the detection system is approximately 20 keV which corresponds to an obtained depth resolution of 70 nm at the surface for perpendicular incidence. The scattering cross-section for elastic scattering of He<sup>++</sup> from Ge turns non-Rutherford at approximately 9 MeV for  $\theta=155^\circ$  [10]. Thus no problems are expected with rapidly varying nuclear scattering cross-sections.

The 6.0 MeV He<sup>++</sup> ion beam was aligned with the  $\langle 100 \rangle$  axis and the backscattering spectrum has been acquired for 120 minutes to allow enough statistics. After this measurement the sample has been tilted 5 degrees away and rotated over 1.5 degree away from the aligned position and the azimuthally averaged random spectrum has been acquired for 40 minutes. Figure 5.2 shows both the azimuthally averaged and  $\langle 100 \rangle$  aligned backscattering spectra. The non-Rutherford scattering from silicon, of ions with energies exceeding 4 MeV, results in a wildly varying backscattering yield which dominates the random spectrum. This variation is highly suppressed in the channeled spectrum which shows a much smoother profile. Due to the resonant scattering cross-section the silicon yield is inadequate to use for the determination of defect depth distributions. The measured Ge yield is therefore used to determine the number of defects.

Damage Depth Profiling 4  $\mu\text{m}$  SiGe on Si

**Figure 5.2:** Backscattering spectra ( $\theta=155^\circ$ ) obtained from a 4 micron thick  $\text{Si}_{1-x}\text{Ge}_x$  multi layer grown on  $(100)\text{Si}$  using 6 MeV  $\text{He}^{++}$  ions. The azimuthally averaged and the  $\langle 100 \rangle$  aligned backscattering spectra are depicted. The surface positions for germanium and silicon are indicated by the arrows in the spectra. The non-Rutherford scattering from silicon atoms, of ions with energies exceeding 4 MeV, results in a wildly varying backscattering yield which dominates in the random spectrum.

The random spectrum shows a decreasing germanium yield with increasing depth which reflects the germanium fraction in the layered structure. The random spectrum was simulated using the RUMP code [11] with parameters from the MBE growth menu and a proper fit was obtained. In order to obtain defect profiles the silicon and the germanium random and aligned spectra have been converted to depth profiles using the random stopping powers. These profiles have been used to determine the channeled to random ratio,  $\chi_D(t)$ , as a function of depth. The resulting curves depict the development of the dechanneling as a function of depth and are used to calculate the defect density.



### **5.2.2 Quantification of defect density**

Since TEM analysis suggested that strain relaxation occurred predominantly through dislocation lines at the interfaces only two types of dislocation lines have been considered for quantifications: edge dislocations and screw dislocations. The dechanneling factor  $\sigma_d$  is calculated from the burgers vector,  $b$ , and the half-angle for channeling  $\Psi_{1/2}$ :  $\sigma_d = b/(\Psi_{1/2}\pi)$ . The experimentally determined  $\Psi_{1/2}$  for Si and 1.0 MeV He ions is  $0.63^\circ$  according to Picraux [12]. Extrapolation of this value to the conditions for 6 MeV He ions yields:  $\Psi_{1/2} = 0.26^\circ$  (4.5 mrad). The burgers vector quantifies the direction and magnitude of atom displacements around the dislocation. We assume the direction of the burgers vector for the line dislocations normal to the dislocation axis with the magnitude equal to the  $\sqrt{2}/4$  times the lattice constant [13]. This corresponds to the (110)-inter-planar distance. These assumptions result in an estimated dechanneling factor of  $\sigma_d = 14$  nm for dislocation lines. The aligned scattering yield  $\chi_v(t)$  for a dislocation-free sample was assumed to be 4% of the random scattering yield at depth  $t$  for the entire region of interest. Equation 5.1 is used to calculate the number of defects.

Figure 5.3 depicts the accumulated number of dislocation lines,  $N_d(t)$ , up to a depth  $t$ . The defect profile obtained from the measured Ge scattering yield has been taken from channel 600-830 (fig 5.2) and the defect profile obtained from the Si scattering yield has been taken from channel 200-600. The horizontal scale is indicated as areal density ( $10^{15}$  at/cm<sup>2</sup>) and can be converted to a depth scale in microns (upper scale) by multiplication with the atomic density ( $N = 0.4978 \times 10^{23}$  at/cm<sup>3</sup>). The interpretation problem in the case of non-Rutherford behavior of the cross-section is illustrated by the plotted defect profile obtained from the measured silicon yield. Interpretation of this curve results in unreliable conclusions about the dislocation line density. This is the reason that the germanium profile is used for quantification of the total disorder in the top layer.

From the defect profile in the inset of figure 5.3 the total disorder in the top-most  $0.60 \mu\text{m}$  is found to be smaller than  $0.4 \times 10^5$  dislocation lines per cm. A significant increase of the total number of defects is detected at the depth interval between 1.0 and 2.0 microns. Beyond a depth of 2.5 microns the total disorder does barely increase further. However, at a depth of 3.6 microns an instant increase in the yield is visible. This increase is an artefact due to the scattering yield

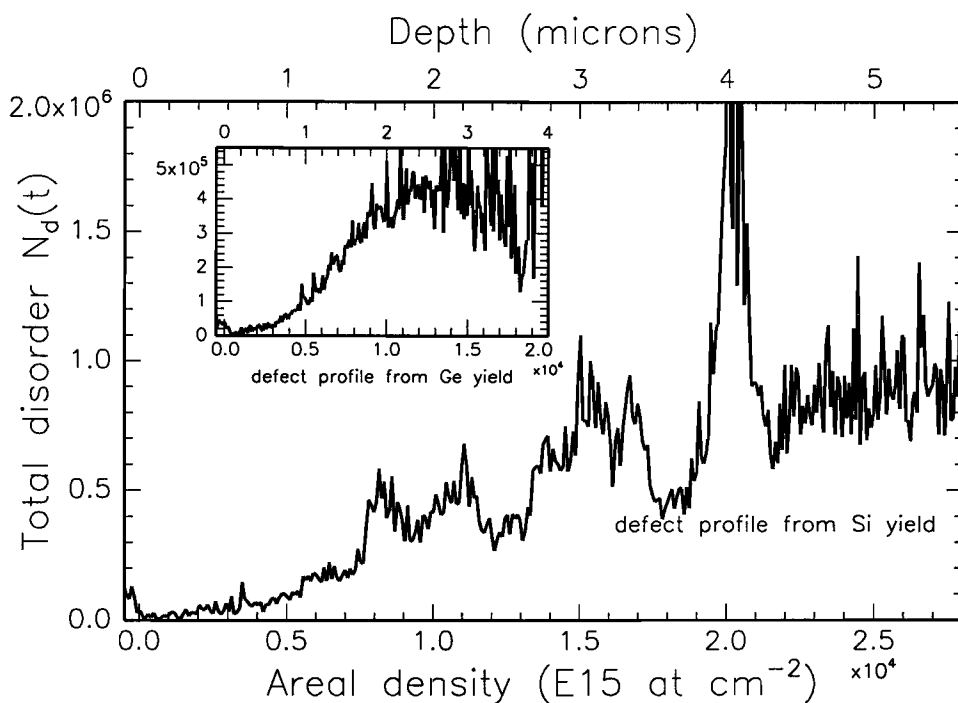


**Figure 5.3:** Defect depth profiles obtained from the measured silicon and germanium yields. The profiles depict the integrated number of defects as a function of depth. The inset depicts the obtained profile from the germanium yield. The resonant scattering cross section for ions scattered on silicon atoms hinders quantification of the defect density in the structure. The total disorder as a function of depth is therefore obtained the defect profile obtained from the germanium yield.

corresponding to surface scattering from silicon which results in an additional background for the germanium yield below channel 600 in the backscattering spectrum (fig 5.2). The defect profile obtained from the germanium yield shows poor statistics for the depth interval between 2.0 microns and 4.0 microns from the surface which is due to the small amount of germanium in this depth interval. According to the obtained profile the integrated disorder in the structure is  $4.6 \times 10^5$  dislocation lines per cm. The estimated error is  $0.2 \times 10^5$  dislocation lines per cm in the near-surface depth interval but due to poor statistics this is increasing for regions at larger depth. The sensitivity for the detection of line dislocations in the near surface region in a SiGe sample is also taken as  $0.2 \times 10^5$  dislocation lines per cm.

### **5.2.3 Discussion**

In the defect-density calculation a constant dechanneling factor,  $\sigma_d$ , and a constant virgin backscattering fraction,  $\chi_v(t)=\chi_v(0)$ , were assumed. At increasing sample depths corrections should be made since the dechanneling factor decreases with decreasing ion energy as  $E^{1/2}$ . The absence of a correction for the dechanneling factor results in an underestimation of the number of defects of about 5% at a depth of 4 microns. The in-depth backscattering fraction for a virgin crystal  $\chi_v(t)$  is always higher than the one near the surface,  $\chi_v(t)\geq\chi_v(0)$ . This effect results in a slight overestimation of the number of defects. It is assumed that the two corrections approximately compensate one another.

It is interesting to compare the measured integrated defect density ( $4.6\times 10^5\text{ cm}^{-1}$ ) with the number of dislocation lines expected in case of full strain relaxation. An estimate for the expected number of line defects at the interface between a  $\text{Si}_{1-x}\text{Ge}_x$  layer and silicon is calculated from the virtual lattice constants of the alloy. The number of planes (110) per unit length corresponds to the reciprocal distance and equals  $5.208\times 10^7$  (110) planes  $\text{cm}^{-1}$  for crystalline silicon. This quantity differs for the  $\text{Si}_{1-x}\text{Ge}_x$  alloy since the virtual lattice constant of the alloy is a linear combination of the lattice constants of its elements. When using a lattice constant of  $5.4307\text{ \AA}$  for silicon and  $5.6579\text{ \AA}$  for germanium,  $5.6\times 10^5$  defect lines per cm are expected for freestanding  $\text{Si}_{1-x}\text{Ge}_x$  ( $x=0.26$ ) on (100) silicon.

The measured defect profile obtained from the germanium yield indicates an integrated maximum number of  $4.6\times 10^5$  line defects per cm which is within ~20% of the expected number of defects.

### **5.2.4 Summary and conclusions**

The use of 6 MeV He ions for the depth profiling of damage is successfully applied to a 4 micron multi-layer of  $\text{Si}_{1-x}\text{Ge}_x$  with an increasing germanium content towards the surface. The number of line dislocations detected in the channeling experiment is smaller than  $0.2\times 10^5$  dislocation lines per cm in the top 0.6 microns and indicates that the 50 nm  $\text{Si}_{1-x}\text{Ge}_x$  capping layer, the tensile strained 20 nm Si layer and the 740 nm  $\text{Si}_{1-x}\text{Ge}_x$  buffer layer of very good crystalline

quality and with a small number of defects. Quantification of the number of dislocation lines in the total stack of  $\text{Si}_{1-x}\text{Ge}_x$  layers results in a number that resembles the number of expected defects within 20% when the dechanneling factor for dislocation lines is used. This confirms the dominance of line defects as observed by TEM.

The interpretation problem in the case of non-Rutherford behavior of the cross-section is illustrated by the plotted defect profile obtained from the measured silicon yield. This curve shows that damage depth profiling with high-energy RBS requires a scattering cross-section that smoothly changes with energy of the incident ions. For germanium alloys grown on silicon substrates layer thicknesses up to 8 microns can be profiled successfully with ions of 9 MeV and a depth resolution of 150 nm.

### 5.3 Characterisation of $\text{Si}_{1-x-y}\text{Ge}_x\text{C}_y$ strained layers

Thin heteroepitaxial films of  $\text{Si}_{1-x-y}\text{Ge}_x\text{C}_y$  with up to 2.0% C and 20% Ge have been characterized with 4 MeV RBS-channeling and 12.6 MeV high-energy ion channeling. The high-energy ion channeling experiments have been carried out to determine the accommodated strain in the epitaxial layers with enhanced accuracy. The development of a growth procedure for  $\text{Si}_{1-x-y}\text{Ge}_x\text{C}_y$  thin films is of interest for the fabrication of low-power heterojunction diodes [14]. Fabrication of the films has been carried out at Arizona State University (ASU), Tempe, with atmospheric pressure chemical vapor deposition (APCVD) using  $\text{C}_2\text{H}_2$  as a C source [15]. The crystallinity of the films is very sensitive to the flow rate of  $\text{C}_2\text{H}_2$  and to the substrate temperature during the growth process. The results of the characterization of the samples will be used to improve the growth technique towards device-quality epitaxial  $\text{Si}_{1-x-y}\text{Ge}_x\text{C}_y$  layers on (100) Si substrates.

Section 5.3.1 reviews the structural and electronic properties of the alloy and the possibilities for the use of these structures in heterojunction diodes. A detailed description of the characterized samples is given. Section 5.3.2 provides the experimental details that were necessary to obtain the ion scattering spectra. The results of the 4 MeV RBS channeling measurements are given in section 5.3.3. Subsequently section 5.3.4 presents the strain measurements with 12.6 MeV  $\text{He}^{++}$  ions on buried  $\text{Si}_{1-x-y}\text{Ge}_x\text{C}_y$  layers. Section 5.3.5 presents measurements of samples consisting of

an epitaxial  $\text{Si}_{1-x-y}\text{Ge}_x\text{C}_y$  layer with an additional silicon capping layer. Finally, conclusions on the analysis with high-energy ion channeling are summarized in section 5.3.6.

### **5.3.1 Applications of the characterized structures in electronic devices**

Band-gap engineering in silicon-based semiconductor technology has been well established through the application of SiGe alloys. The band gap of the  $\text{Si}_{1-x}\text{Ge}_x$  decreases monotonically as the germanium fraction increases [16]. The decrease is magnified by the presence of strain in the layer [17]. For the case of pseudomorphic  $\text{Si}_{1-x}\text{Ge}_x$  films grown on Si(100) substrates, the compressive strain results in a major drawback i.e. a structural and thermal instability illustrated by the limited film thickness and processing temperatures [18]. The addition of substitutional carbon into SiGe alloy layers has been suggested to diminish strain and thus enhance the stability. The lattice constant of a  $\text{Si}_{1-x-y}\text{Ge}_x\text{C}_y$  free-standing ternary alloy can be estimated applying Vegard's law and adopting lattice constants for bulk silicon (0.54307 nm), for germanium (0.56579 nm) and for carbon (0.3545 nm). Full strain compensation should be accomplished for 8.3 at% Ge by addition of 1 at% C. The presence of a small amount of carbon will reduce the stress in the film and hereby the likelihood of misfit dislocation formation during device fabrication. In addition, the presence of the substitutional carbon will modify the band gap. Carbon in its diamond form is an elemental group-IV insulator with a band gap of 5.5 eV, much wider than silicon (1.13 eV) or germanium (0.62 eV). The estimated band gaps for the ternary alloy in relation to the strain have been extensively discussed by Soref [19] and falls somewhere in between 0.62eV - 5.5eV. The electrical and structural properties of the  $\text{Si}_{1-x-y}\text{Ge}_x\text{C}_y$  heterostructures indicate the technical potential for low-power applications in device-fabrication technologies, i.e. heavy-doped-base transistors.

Five samples have been characterized which were grown on Si(100) with APCVD at 700°C. The temperature used during the APCVD process allows for enhanced surface diffusion which permits atoms to occupy substitutional sites hereby minimizing the total energy of the system. A description of the samples is given in table 5.1. Two of the analysed samples consist of a heteroepitaxial  $\text{Si}_{1-x-y}\text{Ge}_x\text{C}_y$  film with an additional 200 nm Si capping layer. The remaining other three samples do not have the Si capping layer.

SAMPLE	Si cap (nm)	Si %	Ge %	C %	SiGeC (nm)	RBS ( $\pm 10$ nm)	$\chi_{\min <100>}$
12C	none	77	22	1	225	215	0.05
12D	none	77	21	1.7	220	215	0.05
15K	200	78	21	1	125	187 / 113	0.03
15L	200	78	22	0	125	187 / 113	0.03
15N	none	78	20	2	740	743	0.03 - 0.1

**Table 5.1:** Composition of the characterized APCVD grown samples. Sample number is given in the first column. The elemental atomic fractions of the grown  $\text{Si}_{1-x-y}\text{Ge}_x\text{C}_y$  are listed in column 3-5. Layer thicknesses obtained from the growth menu are given in nm and listed in column 2 and 6. Layer thicknesses obtained from the RBS analysis (section 5.3.3) are listed in column 7. The two values listed for sample 15K and 15L concern the measured thicknesses of capping and SiGeC layer. The measured minimum yields are listed in the last column.

The fraction of carbon in the SiGeC layers has been obtained in a 4.28 MeV nuclear-scattering experiment which profits from the enhanced scattering cross-section of the  $^{12}\text{C}(\alpha, \alpha)^{12}\text{C}$  elastic-resonance-reaction. These energy-dispersive resonant profiling experiments were carried out at ASU. SIMS carbon profiles have also been obtained at ASU and showed that the carbon was distributed uniformly in the alloy layers of these samples. At EUT the crystal quality and strain of the  $\text{Si}_{1-x-y}\text{Ge}_x\text{C}_y$  layers were determined applying 4 MeV RBS channeling and 12.6 MeV high-energy ion channeling.

### 5.3.2 Experimental details for characterization of the $\text{Si}_{1-x-y}\text{Ge}_x\text{C}_y$ structures

Experiments with 4 MeV  $\text{He}^+$  ions were carried out using the 50 mm<sup>2</sup> PIPS detector at a backscattering angle of 170 degrees. The maximum angular spread of the incident beam was limited to 0.075° in both the horizontal and vertical planes and the beam current was 10 nA. The quality of the grown layer is determined from the <100> aligned and the random backscattering spectra. The 4 MeV RBS results of all five samples will be presented in section 5.4.3.

Strain analysis of the  $\text{Si}_{1-x-y}\text{Ge}_x\text{C}_y/\text{Si}$  structures was carried out with He ions of 12.6 MeV using the 900 mm<sup>2</sup> detector. Angular scans through the <111> channel in the (110) plane were measured with the detector located at  $\theta=65^\circ$ , hereby benefiting from an enhanced germanium backscattering yield. The maximum angular spread of the 12.6 MeV  $\alpha$  beam was limited to

0.070° and a beam current of 10 nA was used. The tetragonal distortion of the  $\text{Si}_{1-x-y}\text{Ge}_x\text{C}_y$  layer was determined directly from the angular difference between the  $\langle 111 \rangle$  angular scan, obtained from the integrated germanium scattering yield in the measured energy spectra, and the angular scan through the  $\langle 100 \rangle$  axis. This straight-forward determination of the strain from the shift,  $\Delta\theta_{\langle 111 \rangle}$ , is justified for buried distorted layers when the angular shifts expected are larger than the characteristic angle for channeling,  $\Psi_{\langle 111 \rangle} = 0.21^\circ$ .

The results of the strain analysis of the  $\text{Si}_{1-x-y}\text{Ge}_x\text{C}_y/\text{Si}$  samples without a capping layer will be presented in section 5.3.4. The results of the characterization of the  $\text{Si}/\text{Si}_{1-x-y}\text{Ge}_x\text{C}_y/\text{Si}$  samples (with a capping layer) will be presented in section 5.3.5.

### **5.3.3 Characterisation of composition and sample structure**

The composition, layer thickness and crystalline quality of all five samples were derived from the 4 MeV  $\text{He}^+$  RBS measurements. To enhance depth resolution the detector was located at 170 degrees and a glancing-angle scattering geometry was chosen. The angle of the incident beam with the sample normal was 65 degrees and the angle of the detected scattered ions with that normal was 75 degrees. The combination of the glancing-angle geometry and a detector with an energy resolution of 25 keV (FWHM) results in a depth resolution near 17 nm. Use of the glancing-angle geometry is necessary to determine both the layer thickness and the germanium fractions of the  $\text{Si}_{1-x-y}\text{Ge}_x\text{C}_y$  films. The Si/Ge ration and layer thickness of the various layers were determined from simulations of the measured energy spectra using the RUMP code assuming the C concentration provided in table 5.1.

The deduced layer thicknesses of the  $\text{Si}_{1-x-y}\text{Ge}_x\text{C}_y$  layers are 215 nm for samples 12C and 12D and 113 nm for sample 15K and 15L. The latter two samples have an additional 187 nm thick silicon capping layer. The layer thickness of the  $\text{Si}_{1-x-y}\text{Ge}_x\text{C}_y$  top layer of sample 15N is obtained from the width of the germanium peak in the random spectrum as is indicated in figure 5.3. and equals 743 nm. Simulations with varying layer thicknesses show that the given numbers are accurate within 10 nm. The RBS results are summarized in the seventh column of table 5.1. The measured layer thicknesses agree within 5% with the values from the APCVD growth menu. The Si and Ge atomic fractions are within 1 at% of the composition obtained from the growth menu. The

carbon signal is submerged by the silicon background in the RBS spectra due to the small cross-section for elastic scattering of  $\text{He}^+$ .

The crystalline quality of the samples was determined from the measured  $\langle 100 \rangle$  aligned and random backscattering spectra using 4 MeV  $\text{He}^+$  ions. First the results of the characterization of sample 15N are presented. Figure 5.3 depicts the channeled and random backscattering spectra of sample 15N; the 743 nm thick  $\text{Si}_{1-x}\text{Ge}_x\text{C}_y$  film on Si(100). The observed silicon yield variation in the near surface region (channel 300-350) of the random spectrum is not due to a non-

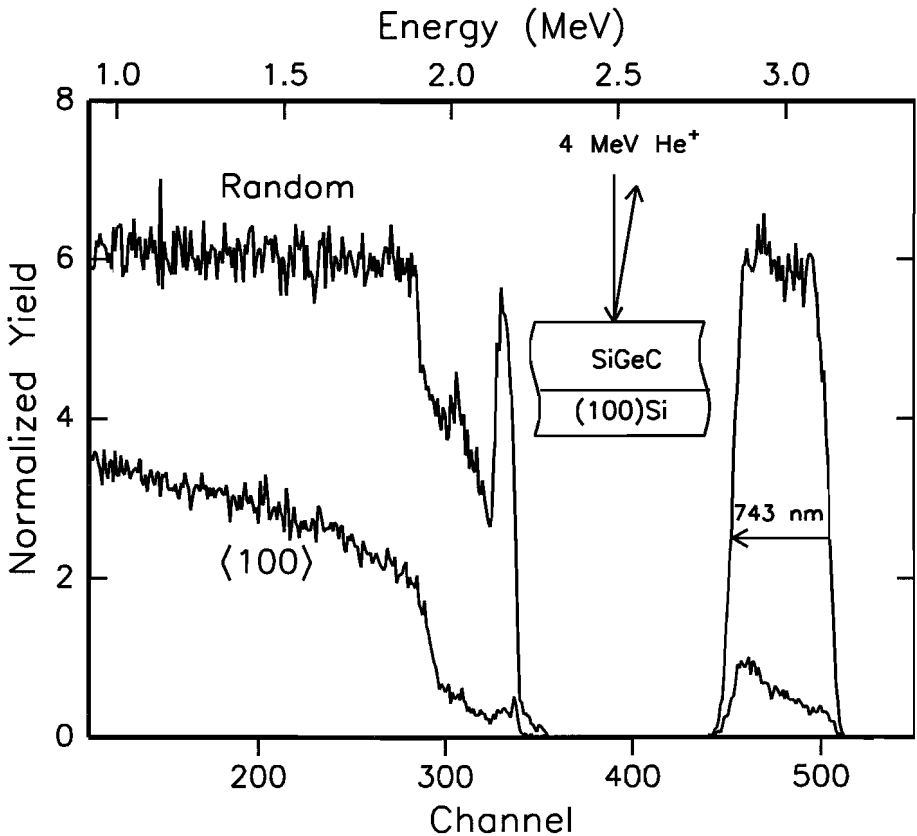


**Figure 5.3:** The  $\langle 100 \rangle$  channeled and random backscattering spectra of sample 15N. The silicon yield variation in the near surface region is due to a resonance in the scattering cross-section. The germanium normalized channeled yield increases steadily with depth from  $\chi=0.03$  at the surface towards  $\chi=0.10$  at the interface. The normalized silicon yield of the  $\langle 100 \rangle$  aligned spectrum shows a pronounced increase at the SiGeC/(100)Si interface, towards  $\chi=0.35$  which confirms the presence of interfacial defects.



uniformity of composition of the top layer but is due to a resonance in the  $^{28}\text{Si}(\alpha, \alpha)^{28}\text{Si}$  scattering cross-section [20] which occurs near 3.9 MeV. The yield variation is less pronounced for the  $\langle 100 \rangle$  aligned spectrum.

In the  $\langle 100 \rangle$  channeled spectrum the germanium yield increases steadily with depth. The normalized Ge yield right behind the surface peak is  $\chi=0.03$  and it increases up to  $\chi=0.10$  at the interface with the silicon substrate. The observed rapidly increasing minimum yield shows that the grown film is of poor crystalline quality. The silicon  $\langle 100 \rangle$  channeled yield shows the surface peak and a slowly increasing yield with depth, with  $\chi=0.03$  behind the surface peak and an increase towards  $\chi=0.10$  at the  $\text{Si}/\text{Si}_{1-x-y}\text{Ge}_x\text{C}_y$  interface. A pronounced increase of the Si yield at the interface of the  $\text{Si}_{1-x-y}\text{Ge}_x\text{C}_y$  layer and the Si(100) substrate near channel 290 indicates the presence of many interfacial defects. The normalized Si yield increases towards  $\chi=0.35$ . Since the normalized Si yield remains high in the Si substrate dislocation lines at the interface are most likely to occur. This indicates a poor match of the film on the Si(100) substrate.

The total disorder in sample 15N is determined from the calculated normalized yield profile using equation 5.1. Since the nature of the defects has not independently been established with TEM, the product of the dechanneling factor,  $\sigma_d$ , and the integrated density  $N_d(t)$  is plotted versus depth in figure 5.4. If the instant yield increase at the SiGeC/Si interface is due to the formation of dislocation lines the integrated number of interfacial defects at the  $\text{Si}_{1-x-y}\text{Ge}_x\text{C}_y/\text{Si}$  interface can be calculated when a dechanneling factor is assumed. The quantification of the number of dislocation lines is carried out using the virgin fraction  $\chi_v(t)$  as a constant fraction of the random yield ( $\chi_v(t)=0.03\chi_r(t)$ ). The quantification assumes a dechanneling factor of  $\sigma_d=12$  nm for 4 MeV  $\text{He}^+$  ions interacting with dislocation lines.

Figure 5.4 depicts the defect profile obtained from the silicon normalized yield of sample 15N and shows that the accumulation of disorder in the  $0.743 \mu\text{m}$  thick  $\text{Si}_{1-x-y}\text{Ge}_x\text{C}_y$  film and a step-wise increase at the SiGeC/Si interface. A profile obtained from a defect free virgin silicon crystal is also depicted in figure 5.4. This virgin profile shows the increase of the normalized yield due to dechanneling in the virgin crystal and can be misinterpreted as an increase of the

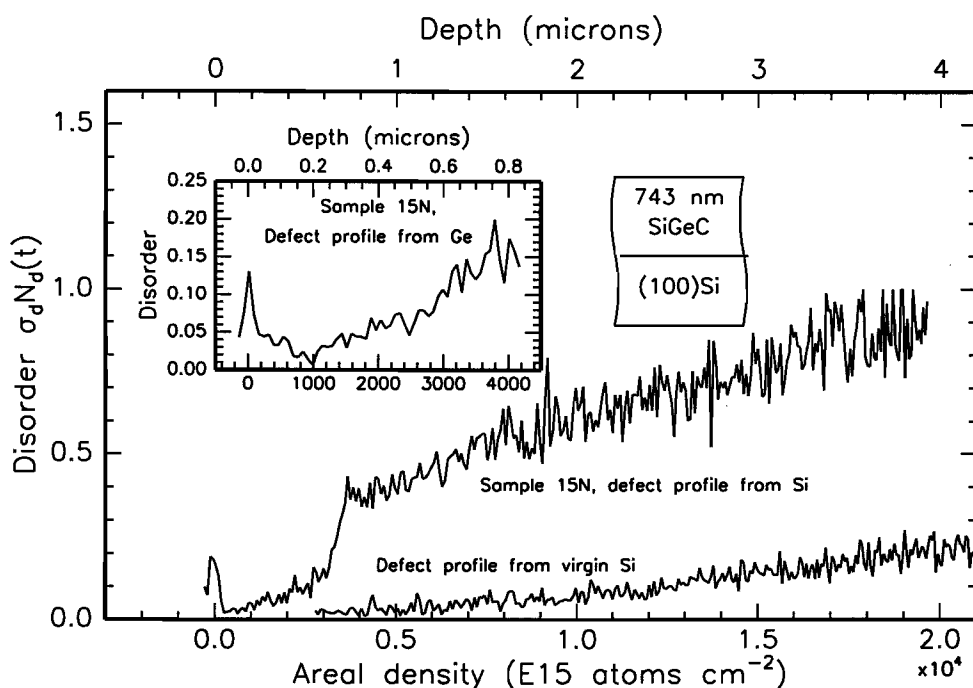


**Figure 5.4:** The obtained defect profiles from the Si and Ge spectra of sample 15N. The virgin Si profile shows the yield increase due to dechanneling in the virgin crystal. The defect profile derived from the germanium yield is shown in the inset. The silicon profile shows a rapid yield increase at the  $\text{Si}_{1-x}\text{Ge}_x/\text{Si}(100)$  interface which indicates a local defect density of most likely dislocation lines.

total disorder. Calculation of the real number of defects in the near surface region of sample 15N needs correction for this effect. However, the plotted virgin profile shows that the correction  $\sigma_d N_d(t) < 0.05$  for a near surface depth interval. This number is taken as a lower limit for detection of disorder.

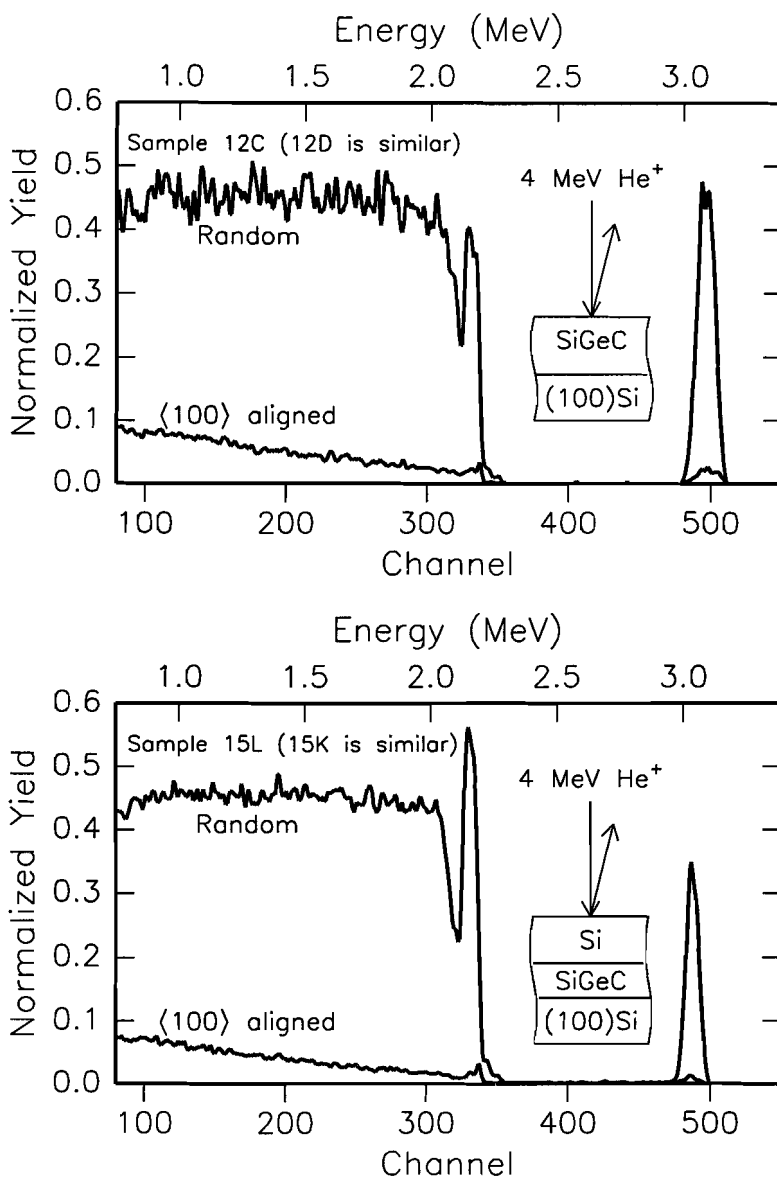
The defect profile deduced from the germanium yield (inset) shows the increase of the number of defects in the  $\text{Si}_{1-x}\text{Ge}_x\text{C}_y$  film top layer. Corresponding to the defect profile obtained from the silicon yield, the integrated disorder reaches ultimately  $\sigma_d N_d(t) = 0.15$ .

Quantification of the number of dislocations can be achieved when the dominant dislocation type and its corresponding dechanneling factor are known. Similar to the analysis of the structure

analyzed in section 5.2 we assume that formation dislocation lines are due to the increased yield. For a fully relaxed  $\text{Si}_{1-x-y}\text{Ge}_x\text{C}_y$  ( $x=0.2$ ,  $y=0.02$ ) film on a Si substrate the misfit is estimated using Vegard's law, which suggests calculation of the lattice constant of the alloy by linear interpolation of the lattice constants by atomic fraction. This suggests a virtual lattice constant of 5.4384 Å, and implies a distance of 1.9228 Å between the neighbouring (110) planes. The dechanneling factor  $\sigma_d$  is calculated using a half-angle:  $\Psi_{1/2} = 0.32^\circ$  (5.5 mrad) and a burgers vector,  $b$ , corresponding to the (110) inter-planar distance. This results in  $\sigma_d=11$  nm.

The assumption of the dechanneling factor indicates a measured number of  $1.4 \times 10^5$  dislocation lines per cm in the SiGeC top layer. The number of dislocation lines at the SiGeC/Si interface is calculated from the step-wise increase of  $\sigma_d N_d(t)=0.25$  and is  $2.3 \times 10^5$  dislocation lines per cm. An estimate for the number of dislocation lines expected on behalf of the composition of the ternary alloy is calculated from the virtual lattice constant of the alloy and the substrate. When using a lattice constant of 5.4307 Å for silicon and 5.4384 Å for the ternary alloy, only  $0.7 \times 10^5$  dislocation lines per cm are expected for a relaxed  $\text{Si}_{1-x-y}\text{Ge}_x\text{C}_y$  film on a (100) silicon substrate. The number derived from the measured disorder profile is significantly larger than expected on behalf of this straight-forward calculation. This indicates that extensive defect clusters or different defect types are due to the observed enhanced scattering yield in the top layer and at the SiGeC/Si interface. Hence no measurement of the strain in the top layer has been carried out on sample 15N.

The crystalline quality of the samples 12C, 12D, 15K and 15L has been determined in a similar manner. The backscattering spectra obtained from sample 12C and 12D are similar and also the spectra obtained from sample 15K and 15L show a close resemblance. This is not surprising since only the carbon concentration in the  $\text{Si}_{1-x-y}\text{Ge}_x\text{C}_y$  films is different and not likely to be detected in the RBS channeling experiment. Typical random and  $\langle 100 \rangle$  channeled energy spectra are shown in figure 5.5. The top figure depicts both the random and  $\langle 100 \rangle$  aligned backscattering spectra from samples 12D (spectra from 12C are similar) while the lower spectra have been obtained from sample 15L (spectra from 15K are similar). The normalized yield near the sample surface is  $\chi=0.05$  for samples 12C and 12D and  $\chi=0.03$  for samples 15K and 15L.



**Figuur 5.5:** The random and  $\langle 100 \rangle$  aligned backscattering spectra obtained from sample 12C (the spectra from 12D are similar) are depicted in the upper figure, spectra of sample 15L (the spectra from 15K are similar) are depicted in the lower figure. The measured minimum yield at the surface is  $\chi_{\min} = 0.05$  for samples 12C and 12D and  $\chi_{\min} = 0.03$  for samples 15K and 15L. The germanium peak in the RBS spectra obtained from samples 15L (and 15K) is shifted towards lower energy due to the presence of the Si capping layer.

The slightly higher normalized yield of sample 12C and 12D can be due to the presence of a little disorder in the thin  $\text{Si}_{1-x-y}\text{Ge}_x\text{C}_y$  top layer. However, the obtained defect depth profiles are very similar to the Si(100) virgin depth profile and the number of defects in the  $\text{Si}_{1-x-y}\text{Ge}_x\text{C}_y$  films is below the detection limit for channeling. No instant increase of the silicon yield or the germanium yield was observed in the aligned backscattering spectra obtained from samples 15K and 15L. This confirms the epitaxial growth of both the  $\text{Si}_{1-x-y}\text{Ge}_x\text{C}_y$  film on the (100)Si substrate and the silicon capping layers on the thin  $\text{Si}_{1-x-y}\text{Ge}_x\text{C}_y$  films. Strain in these epitaxial  $\text{Si}_{1-x-y}\text{Ge}_x\text{C}_y$  layers is still expected since the lattice constant for freestanding  $\text{Si}_{1-x-y}\text{Ge}_x\text{C}_y$  differs from the lattice constant of the silicon substrate. The analysis of the films is completed by measuring the accommodated strain in the  $\text{Si}_{1-x-y}\text{Ge}_x\text{C}_y$  films of samples 12C, 12D, 15K and 15L. The tetragonal distortion is determined in the 12.6 MeV  $\text{He}^{++}$  ion channeling experiments.

#### **5.3.4 Strain analysis of $\text{Si}_{1-x-y}\text{Ge}_x\text{C}_y$ samples without a capping layer**

Figure 5.6 depicts the angular scans of sample 12C and 12D through the  $\langle 111 \rangle$  channels in the (110) planes as measured in the 12.6 MeV  $\text{He}^{++}$  experiment. The integrated germanium scattering yield and the silicon yield (obtained from the substrate) are plotted as a function of the target orientation with respect to the  $\langle 100 \rangle$  axis, which is near the surface normal. The location of the  $\langle 100 \rangle$  channel has been determined by measuring the  $\langle 100 \rangle$  angular scans with the backscattering detector at  $\theta=140^\circ$ . The  $\langle 111 \rangle$  angular scans have been obtained with the detector located at  $\theta=65^\circ$ . The yield in both angular scans is normalized to the yield in an azimuthally averaged spectrum. The location of the  $\langle 111 \rangle$  channel of the  $\text{Si}_{1-x-y}\text{Ge}_x\text{C}_y$  top layer can be derived from the position of the germanium minimum yield. The accommodated strain is determined from the measured angular shift of the  $\langle 111 \rangle$  axis,  $\Delta\theta_{\langle 111 \rangle}$ .

The measured angular position of the Ge  $\langle 111 \rangle$  minimum is  $54.423^\circ \pm 0.001^\circ$  for sample 12C. This implies an angular shift of the  $\langle 111 \rangle$  axis of  $\Delta\theta_{\langle 111 \rangle} = 0.313^\circ \pm 0.001^\circ$  with respect to the location of the  $\langle 111 \rangle$  axis of a cubic crystal. For sample 12D the Ge  $\langle 111 \rangle$  minimum is located at  $54.433^\circ \pm 0.003^\circ$  which indicates an angular shift of  $\Delta\theta_{\langle 111 \rangle} = 0.303^\circ \pm 0.003^\circ$ . The measured angular shifts are larger than the critical angle for channeling;  $\Psi_{\langle 111 \rangle} = 0.21^\circ$ .

The position of the substrate  $\langle 111 \rangle$  minimum is  $54.756^\circ \pm 0.003^\circ$  and  $54.755^\circ \pm 0.002^\circ$  for sample 12C and 12D respectively. This position differs  $0.020^\circ$  with the location of the  $\langle 111 \rangle$  channel for a cubic crystal ( $54.736^\circ$ ). Although the measured tetragonal distortion is larger than the critical angle for channeling, this small difference might be due to the ion-steering effect at the  $\text{Si}_{1-x}\text{Ge}_x\text{C}_y/(100)\text{Si}$  interface. The silicon angular scan shows a decreased scattering yield at the location of the germanium minimum, flanked by two small peaks. The local minimum is caused by axially channeled ions in the  $\text{Si}_{1-x}\text{Ge}_x\text{C}_y$  top layer that are steered into the (110) plane of the substrate at the  $\text{Si}_{1-x}\text{Ge}_x\text{C}_y/\text{Si}$  interface due to their small transverse kinetic energy with respect to the (110) plane in the substrate. The component of the transverse kinetic energy in the  $\langle 111 \rangle$  axis of the  $\text{Si}_{1-x}\text{Ge}_x\text{C}_y$  layer, perpendicular to the (100) plane contributes to both the minimum and the two peaks. Axially channeled ions with high transverse kinetic energy with

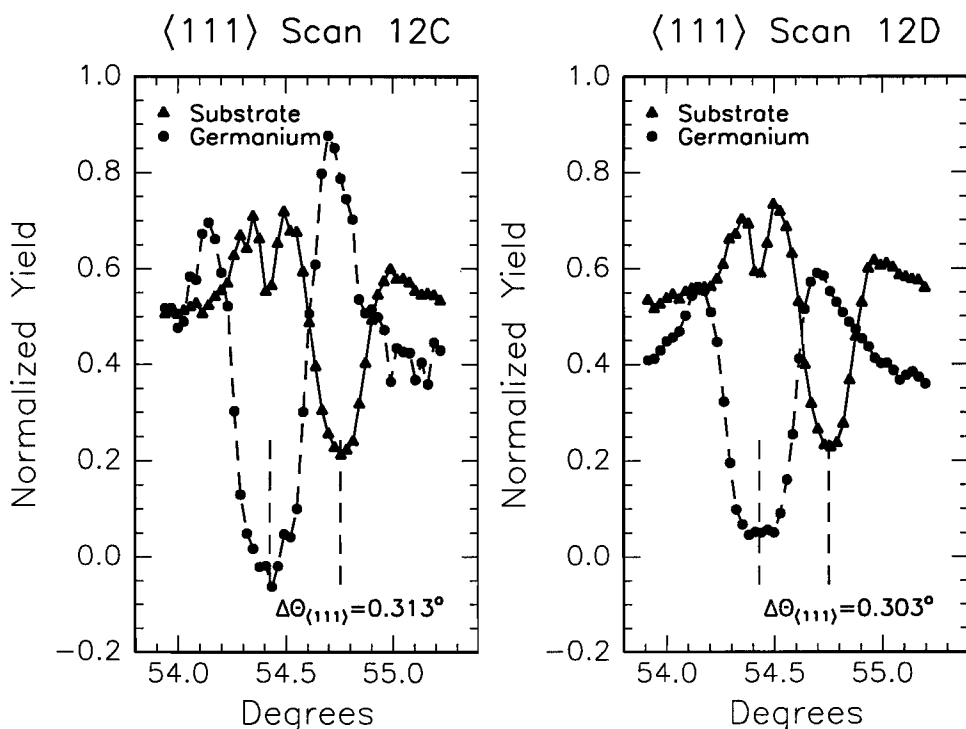


**Figure 5.6:** The measured angular scans of sample 12C and 12D through the  $\langle 111 \rangle$  channels in the (110) planes. The target orientation is with respect to the  $\langle 100 \rangle$  axis. The accommodated strain is determined from the measured angular shift of the  $\langle 111 \rangle$  axis,  $\Delta\theta_{\langle 111 \rangle}$ . The measured angular shifts are:  $\Delta\theta_{\langle 111 \rangle} = 0.313^\circ \pm 0.001^\circ$  for sample 12C and  $\Delta\theta_{\langle 111 \rangle} = 0.303^\circ \pm 0.003^\circ$  for sample 12D.

respect to the (110) plane in the Si substrate will dechannel at this interface since the acceptance for planar channeling is more critical for the magnitude of the transverse kinetic energy. Consequently these ions are likely to dechannel or scatter at the interface as is observed as a slightly increased yield resulting in the two satellite peaks.

Assuming the validity of Vegard's law full strain compensation by the substitutional carbon atoms in the samples would have resulted in an angular shift of the  $\langle 111 \rangle$  axis of  $\Delta\theta_{\langle 111 \rangle} = 0.25^\circ$  for sample 12C ( $y=0.01$ ) and  $\Delta\theta_{\langle 111 \rangle} = 0.12^\circ$  for sample 12D ( $y=0.017$ ). The measured angular shifts are significantly larger which indicates that the present amount of carbon is not fully incorporated in the strain compensation. Theory of bulk elasticity and a presumed validity of Vegard's law indicates that for both samples only 0.8 at% carbon is active in strain compensation based on the measured angular shifts.

### **5.3.5 Strain analysis of $\text{Si}_{1-x}\text{Ge}_x\text{C}_y$ samples with a silicon capping layer**

The strain in the samples 15K and 15L is also determined in a 12.6 MeV  $\text{He}^{++}$  RBS channeling experiment where the location of the  $\langle 111 \rangle$  main crystalline axis is determined. The position of the  $\langle 111 \rangle$  minima is measured with respect to the  $\langle 100 \rangle$  axis near the surface normal. All experimental details are similar to the settings used for characterization of the samples 12C and 12D. The  $\text{Si}_{1-x}\text{Ge}_x\text{C}_y$  layers of the samples 15K and 15L are thinner than the  $\text{Si}_{1-x}\text{Ge}_x\text{C}_y$  layers of the samples 12C and 12D. Furthermore an additional 187 nm ( $\pm 10$  nm) silicon capping layer is present for both sample 15K and 15L. It is likely that the silicon capping layer will influence the shape of the Ge angular scan due to steering effects on the first  $\text{Si}/\text{Si}_{1-x}\text{Ge}_x\text{C}_y$  interface.

Figure 5.7 shows the in plane  $\langle 111 \rangle$  angular scans of the integrated germanium yield and the silicon yield for samples 15K and 15L. The germanium minimum is located at  $54.376^\circ \pm 0.005^\circ$  for sample 15K which correspond to an angular shift of  $\Delta\theta_{\langle 111 \rangle} = 0.360^\circ \pm 0.005^\circ$ . The germanium  $\langle 111 \rangle$  minimum is located at  $54.381^\circ \pm 0.001^\circ$  for sample 15L which results in an angular shift of the  $\langle 111 \rangle$  axis of  $\Delta\theta_{\langle 111 \rangle} = 0.354^\circ \pm 0.002^\circ$ . The position of the Si minimum yield of the substrate scan is located at  $54.743^\circ$  which is only  $0.007^\circ$  higher than expected for a cubic crystal. This value indicates that the angular shift due to ion-steering at the interfaces is negligible. The substrate (silicon) yield and the germanium yield both show satellite sub-minima,

flanked by two peaks caused by the acceptance of ions with limited transverse energy as has been described in the previous section.

The deduced angular shifts do not correspond to the value calculated from the theory of bulk elasticity when assuming full incorporation of the carbon fraction on substitutional sites. Calculations based on theory of bulk elasticity show that incorporation of 1 at% C in the buried layer of sample 15K should reduce the strain and result in an angular shift of  $\Delta\theta_{\langle 111 \rangle} = 0.25^\circ$  when all carbon atoms occupy substitutional lattice sites. The measured angular shift of the  $\langle 111 \rangle$  axis was  $\Delta\theta_{\langle 111 \rangle} = 0.360^\circ \pm 0.005^\circ$  which is significantly larger. According to the measured angular shift only a typical fraction of 0.4 at% carbon contributes to the strain compensation instead of the 1 at% C fraction in the film. The surplus of carbon atoms ( $3 \times 10^{15}$  at/cm<sup>2</sup>) might be located

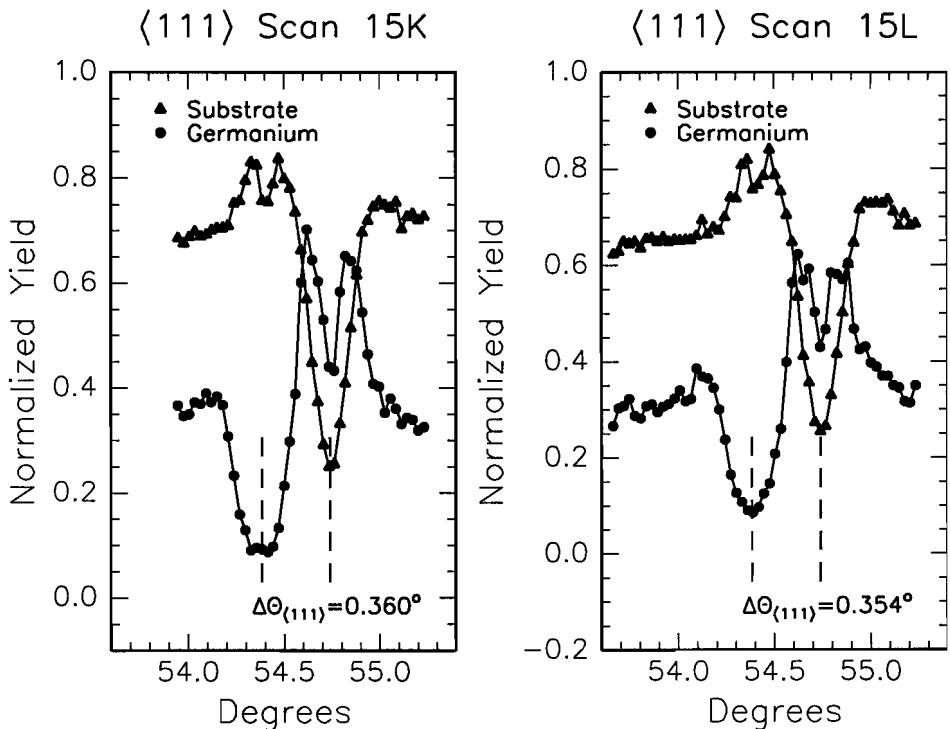


**Figure 5.7:** The in-plane  $\langle 111 \rangle$  angular scans of the germanium yield and the silicon yield of the samples 15K and 15L. The obtained angular shifts for the Ge scans are  $\Delta\theta_{\langle 111 \rangle} = 0.360^\circ \pm 0.005^\circ$  for sample 15K and  $\Delta\theta_{\langle 111 \rangle} = 0.354^\circ \pm 0.001^\circ$  for sample 15L. The satellite peaks in the germanium yield are related to ion steering at the  $\text{Si}/\text{Si}_{1-x}\text{Ge}_x\text{C}_y$  interface as explained in the text.



in the film as isolated interstitials. Quantification of the number of isolated interstitials from the measurements is not possible since the normalized yield increase is invisible due to the small dechanneling cross section for isolated interstitials.

The calculated angular shift is  $\Delta\theta_{\langle 111 \rangle} = 0.44^\circ$  for sample 15L while  $\Delta\theta_{\langle 111 \rangle} = 0.354^\circ \pm 0.002^\circ$  was measured. The observed strain relaxation in sample 15L might be due to the creation of a number of defects or misfit dislocations since no carbon is incorporated in the lattice which might have induced this. When formation of dislocation lines is assumed the difference is explained when the number of dislocation lines is  $0.8 \times 10^5$  per cm. This is close to the detection limit for dislocation lines as given in section 5.3.3, which explains that no difference with a virgin crystal yield is observed. Another possibility might be that agglomerate of point defects contribute to the strain relaxation. The cross-section for dechanneling from point defects is much smaller which would explain that the measured normalized yield is near the normalized yield obtained from a virgin crystal.

### **5.3.6 Summary and conclusions**

Characterization of the  $\text{Si}_{1-x-y}\text{Ge}_x\text{C}_y$  structures with 4 MeV  $\text{He}^+$  RBS and 12.6 MeV  $\text{He}^{++}$  ion channeling has been carried out successfully. The crystallinity of sample 15N was definitely far beyond defect-free device quality. The obtained  $\langle 100 \rangle$  aligned backscattering spectrum implied the presence of interfacial defects at the  $\text{Si}_{1-x-y}\text{Ge}_x\text{C}_y/(100)\text{Si}$  interface. Depth profiling of the disorder resulted in a calculated number of  $2.3 \times 10^5$  interfacial dislocation lines and  $1.4 \times 10^5$  dislocation lines in the top  $\text{Si}_{1-x-y}\text{Ge}_x\text{C}_y$  film. This suggests a bad fit of the film on the Si(100) substrate. Channeling measurements showed that the samples 12D, 12C, 15K and 15L were of much better crystalline quality and were grown epitaxially. The number of interfacial defects was below the detection limit, smaller than  $0.5 \times 10^5$  dislocation lines per cm. The strain was derived from the measured kink angles  $\Delta\theta_{\langle 111 \rangle}$  and vary significantly from the strain expected on behalf of the given sample compositions as calculated using theory of bulk elasticity and Vegard's law. Systematic errors in the determination of the kink angle due to steering effects is unlikely since the measured kink angles are larger than the characteristic angle for channeling;  $\Psi_{\langle 111 \rangle} = 0.21^\circ$ . The results of strain analysis suggest that a typical fraction of 50% of the incorporated carbon

contributed to the strain compensation.

Measurements with other analytical techniques such as TEM and HRXRD will be necessary to obtain detailed additional information on the crystalline structure of the grown samples and confirm our results. Analysis of the samples with TEM could provide information on the types of defects in the SiGeC layers since the detection limit is better than  $0.5 \times 10^5$  dislocation lines per cm. Subsequently the dechanneling factor corresponding to the dominant defect could be used for quantification of the defect density in the measured defect profiles. Glancing angle X-ray diffraction could be used to confirm the presence of tetragonal distortion of the strained SiGeC layers. Together with our data additional results obtained from these analytical techniques might be of great help to improve the APCVD growth technique further towards a reliable method for the epitaxial growth of device-quality ternary heterostructures.

#### **5.4 Defect analysis of plasma etched GaAs/Al<sub>y</sub>Ga<sub>1-y</sub>As/In<sub>x</sub>Ga<sub>1-x</sub>As/GaAs heterostructures**

The RBS channeling technique was applied to investigate the crystalline quality of an MBE grown GaAs/AlGaAs/InGaAs/GaAs heterostructure. These heterostructures are of interest since the GaAs material has high electron mobility and allows fabrication of fast opto-electronic devices with superior frequency characteristics. Section 5.4.1 describes the physical properties of this heterostructure and the possibilities for the use of the structure as a transistor. During the transistor fabrication process, contacts for source, drain and gate need to be constructed on the heterostructure. The gate contact controls the conductivity of the channel that connects the source and drain and is usually below the semiconductor surface. The gate recess step is critical in the fabrication process of the field-effect transistor. This step concerns the etching of the highly doped GaAs top layer which can be achieved by either wet chemical etching or by dry plasma etching. Since plasma etching offers a very good reproducibility and uniformity the interest for dry processing is rapidly increasing. Furthermore the plasma etch is anisotropical and hence reduces underetch which allows processing of smaller structures.

The effect of the ion bombardment and the CH<sub>4</sub>/H<sub>2</sub>/Ar reactive etching plasma on the optical and electrical properties of the heteroepitaxial structure has been studied by Van Es et al. [21]. They found that the electron mobility in the AlGaAs/InGaAs/GaAs heterostructure had dramatically decreased after the etch procedure and was not restored after thermal annealing treatment of the etched wafer. In addition to a decreased electron mobility, sample structure changes e.g. creation of defects or strain relief of the meta-stable InGaAs layer, could be induced by the plasma etching procedure. The aim of this work was to investigate whether the sensitivity of high-energy ion channeling for the analysis of these heterostructures was sufficient to find a correlation between sample damage and decreased electron mobility.

Effects of processing steps on these sample structures have been reported in literature. Strain relaxation of a GaAs/In<sub>0.2</sub>Ga<sub>0.8</sub>As/GaAs single-layer quantum well (SQW), initiated by an 1050°C annealing treatment, has been observed by Kozanecki et al. [22] who used 2 MeV He<sup>+</sup> RBS to determine the strain in the In<sub>0.2</sub>Ga<sub>0.8</sub>As layer. The availability of high-energy ions offers

possibilities for strain measurement with enhanced angular accuracy. Experimental details concerning the channeling measurements are presented in section 5.4.2. The strain in the metastable InGaAs layer was derived from angular scans obtained before and after plasma treatment. The angular scans are presented in section 5.4.3. Section 5.4.4 discusses the results and presents the conclusions. First a detailed description of the analyzed structure and its applications in the fabrication and design of electronic devices is presented.

#### 5.4.1 Characteristics of the heterostructure and applications in electronic devices

A recent detailed study on the processing and characterization of the analyzed structures is provided in the thesis of Van Hassel [23]. The characterized GaAs/Al<sub>y</sub>Ga<sub>1-y</sub>As/In<sub>x</sub>Ga<sub>1-x</sub>As/GaAs heterostructure is a typical multi layer grown for the fabrication of Heterostructure Field-Effect Transistors (HFETs). In this device the electrons are spatially separated from their donor atoms and confined in a two-Dimensional Electron Gas (2-DEG) through which the charge transport takes place. In the structure of interest this 2-DEG is located in the In<sub>x</sub>Ga<sub>1-x</sub>As layer. Apart from better transport properties of electrons in InGaAs, the increased band gap allows a higher sheet density and a greater carrier confinement. The donor atoms are spatially separated from the InGaAs layer as a  $\delta$ -doped donor layer. The deficit of donor atoms in the InGaAs conducting layer in the HFET provides enhanced charge carrier transport. Present donor atoms or defects would act as scatter centers and affect the electron transport induced by Coulomb interaction. Introduction of a small (1-5 nm) undoped AlGaAs spacer layer, between the InGaAs and the  $\delta$ -doped donor layer, increases the separation between the electrons and the ionized donors and further reduces the Coulomb scattering of the electrons with the ionized donors. Hence the introduction of this spacer layer leads to an increased electron mobility. The electrons from the ionized donor atoms transfer to the InGaAs layer, which has a smaller band gap. In this way an electric field is build up and by Coulomb attraction the electrons are confined to a plane along the AlGaAs/InGaAs interface and form a 2-DEG.

The characterized heterostructure was GaAs/Al<sub>0.25</sub>Ga<sub>0.75</sub>As/In<sub>0.15</sub>Ga<sub>0.85</sub>As/GaAs on (100)GaAs. This sample is further referred to as W483H99. The heterostructure had been grown by means of MBE on a (100) oriented GaAs substrate at the EUT in the division of Solid State Physics.

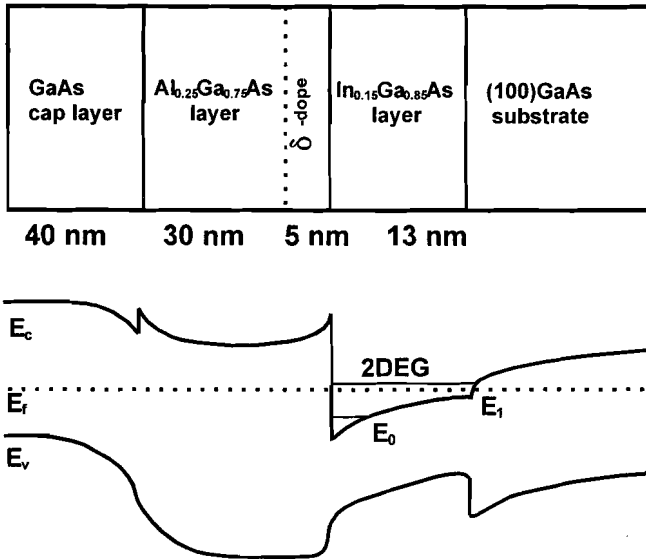


**Figure 5.8:** The sample structure and the band gap diagram are depicted in the figure. The location of the 2DEG and the Si  $\delta$ -dope are indicated.

The given layer thicknesses were obtained from the growth menu. On top of the (100) substrate a GaAs buffer layer and a 13 nm undoped In<sub>0.15</sub>Ga<sub>0.85</sub>As layer were grown, followed by an undoped 5 nm Al<sub>0.25</sub>Ga<sub>0.75</sub>As spacer layer, a  $1.5 \times 10^{12}$  at/cm<sup>3</sup> Si  $\delta$ -doped layer and a 30 nm Al<sub>0.25</sub>Ga<sub>0.75</sub>As layer, doped with  $1.5 \times 10^{18}$  at/cm<sup>3</sup> Si. Finally, a heavily doped 40 nm GaAs top layer with  $2 \times 10^{18}$  at/cm<sup>3</sup> Si was grown to prevent the AlGaAs from oxidation. Figure 5.8 depicts the sample structure and the band gap diagram. The location of the 2DEG is indicated in the figure. After analysis of the sample with RBS channeling the top 40 nm was dry etched with a ECR plasma and the sample was analyzed again. Any observed differences between backscattering spectra or angular scans measured before and after the treatment i.e. enhanced minimum yield, shifted peaks in the measured backscattering spectra or shifted angular scans are likely due to the plasma treatment.

#### 5.4.2 Experimental details

RBS combined with ion channeling is used to determine the strain and the crystalline quality of the GaAs/AlGaAs/InGaAs/GaAs structure before and after the plasma treatment. The straightforward measurement of the  $\langle 111 \rangle$  angular scan requires a background free indium

signal. This signal is preferentially separated from the As surface edge in the RBS spectra even when the ion beam impinges the sample at a  $54^\circ$  incidence angle with respect to its surface normal. The required mass resolution ( $M_{\text{In}}=114.8$  amu,  $M_{\text{As}}=74.9$  amu) implies a backscattering angle close to  $180^\circ$ . The maximum detector angle is restricted by the detector disk design to a maximum backscattering angle of  $170^\circ$ . The  $50 \text{ mm}^2$  PIPS detector with an energy resolution of 23 keV (FWHM) was positioned at this scattering angle. Measurements by Kozanecki et al. [24] who used 1.5 MeV and 2 MeV  $\text{He}^{++}$  for their strain measurements on GaAs/InGaAs/GaAs SQW's showed that the indium signal was well separated from the As surface edge when the thickness of their GaAs capping layers was only 30 nm. In order to obtain kinematic separation and a good depth resolution they used a detector with energy resolution of 12 keV (FWHM), located at a  $150^\circ$  scattering angle. The thickness of the capping layer of the sample that we analyzed is 40 nm. Characterization of the sample described in section 5.4.1 with 2 MeV  $\text{He}^{++}$  ions, a glancing incident beam ( $54^\circ$  with respect to the sample normal) and a detector with an energy resolution of 23 keV (FWHM) provides insufficient kinematic separation of the In peak from the Ga and As surface peaks and thus hampers selection of a background-free In signal. The use of a higher beam energy ( $> 2$  MeV) enhances the kinematic separation of the In peak and is therefore recommended for the strain analysis of the sample of interest.

A more prominent advantage of the use of high-energy ions in strain analysis, i.e. the enhanced angular resolution in the strain determination and the reduced beam steering in the top layer, would suggest a preferable ion energy in the 10-15 MeV region. However, this would drastically reduce the indium backscattering cross-section, which is still obeying the Rutherford behaviour for those ion energies. To compromise between angular resolution and scattering cross-section, 4 MeV  $\text{He}^+$  ions were used for the strain measurements.

RUMP simulations were performed to obtain the optimum scattering geometry. The simulated  $170^\circ$  backscattering spectrum shows a well separated indium peak. Separation of the In from the As surface edge remains visible when the angle between incoming beam and sample normal is  $54^\circ$ , even when the 40 nm GaAs top layer is present. This geometry is necessary to obtain the  $\langle 111 \rangle$  angular scans for strain analysis. Due to the limited InGaAs film thickness (13 nm) and

the small amount of indium in the pseudomorphic film (15 at%), the indium peak area is small with respect to the background originating from pile-up. Simulations showed that the pile-up background increases rapidly when the beam current exceeds 10 nA. Hence experiments have been carried out with a beam current of 10 nA and a pile-up-reduction-circuit.

### 5.4.3 Measurements on GaAs/Al<sub>0.25</sub>Ga<sub>0.75</sub>As/In<sub>0.15</sub>Ga<sub>0.85</sub>As/GaAs with RBS and channeling

Figure 5.9 depicts the measured 170° RBS energy spectrum for the azimuthal averaged and the <100> aligned sample. It is noted that the detected indium yield ( $4 \times 10^{15}$  In at/cm<sup>2</sup>) is close to the

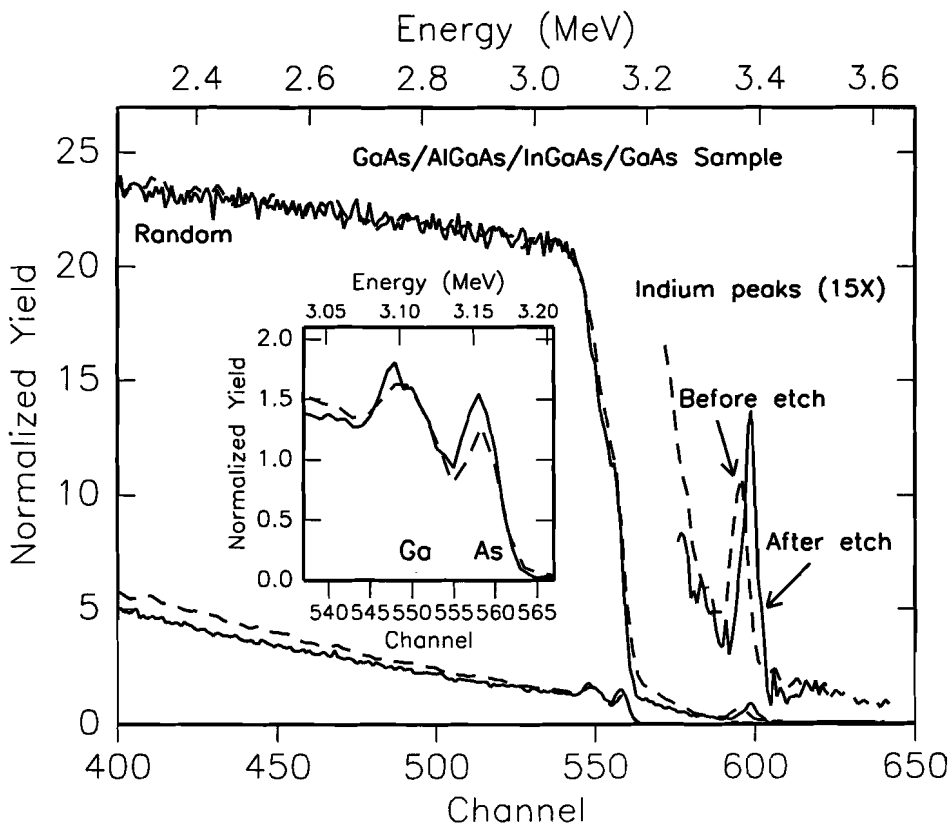


**Figure 5.9:** The measured 170° RBS energy spectrum for the azimuthal averaged and the <100> aligned sample. The minimum yield is  $\chi_{min} = 0.06$  for both the 'as grown' and the etched sample. The inset depicts the Ga and As surface peaks of the <100> aligned spectra. The surface peaks are slightly higher for the etched sample. No rapid increase of the minimum yield as a function of depth has been observed which confirms the good crystalline quality of the grown structure before and after etching of the top layer.

detection limit for Rutherford Backscattering Spectrometry. The In peak observed in the RBS spectrum of the etched sample is shifted towards higher energy due to the absence of the GaAs top layer and thus the absence of stopping of the incident and scattered ions. Simulation of the backscattering spectra with the RUMP code confirmed that a 40 nm GaAs top layer had been removed by the etching procedure. The minimum yield is derived from the integrated indium signal in the channeled and random spectra and corresponds to  $\chi_{\min} = 0.06$  for both the 'as grown' and the etched sample.

No rapid increase of the minimum yield as a function of depth was observed which confirms the good crystalline quality of the structure and little interfacial defects. The areal density of aluminum atoms and silicon donor atoms is far below the detection limit for RBS. Slight differences in the magnitude of the Ga and As surface peaks in the aligned spectrum were observed which point to amorphisation of the near surface region of the sample due to the plasma etching process. The number of displaced atoms is quantified assuming a defect-scattering-cross-section equal to the elastic scattering cross section of  $\text{He}^{++}$  from As. This results in  $8 \times 10^{15}$  at/cm<sup>2</sup> randomly displaced atoms in the top layer. The limited depth resolution restricts the exact determination of the layer thickness in which these defects are present to 50 nm.

The locations of the  $\langle 111 \rangle$  crystalline axes with respect to the  $\langle 100 \rangle$  axis were determined in angular-scan measurements in the (110) plane through the  $\langle 111 \rangle$  axes. The angular scans were carried out on the 'as grown' sample and directly after plasma etching of the heavily doped 40 nm GaAs top layer. Figure 5.10 depicts the angular scans obtained in both experiments. Each point in the angular scan is derived from an energy spectrum which was acquired for 3 minutes. The observed shifts of the indium angular scans with respect to the GaAs angular scans demonstrates that strain is present in the InGaAs sub-layer of both the 'as grown' and the etched sample. The straightforward determination of the position of the minima results in angular shifts of  $\Delta\theta_{\langle 111 \rangle} = 0.63^\circ \pm 0.02^\circ$  for the 'as grown' sample and  $\Delta\theta_{\langle 111 \rangle} = 0.55^\circ \pm 0.01^\circ$  for the etched sample. Theory of bulk elasticity and application of Vegard's law predicts an angular shift of the  $\langle 111 \rangle$  axis of  $\Delta\theta_{\langle 111 \rangle} = 0.55^\circ$  for the epitaxial  $\text{In}_{0.15}\text{Ga}_{0.85}\text{As}$  layer with respect to the  $\langle 111 \rangle$  axis of the GaAs substrate. This corresponds with the measured angular shift of the etched sample.



The characteristic angle for channeling in GaAs is  $\Psi_{\langle 111 \rangle} = 0.56^\circ$  so that steering effects are expected especially for the analysis of the buried  $\text{In}_{0.15}\text{Ga}_{0.85}\text{As}$  layer sample before etching. As a consequence the angular scan of the indium yield for the ‘as grown’ sample is highly asymmetric and the position of the scan minimum is shifted. The enhanced In yield in the ‘as grown’ scan is most probably due to detection of ions that scattered from indium but were initially channeled in the  $\langle 111 \rangle$  direction of the GaAs top layer. These ions did not remain channeled in the  $\langle 111 \rangle$  direction of the InGaAs layer due to the large kink angle at the GaAs/InGaAs interface. Straight-forward determination of the location of the In minimum results

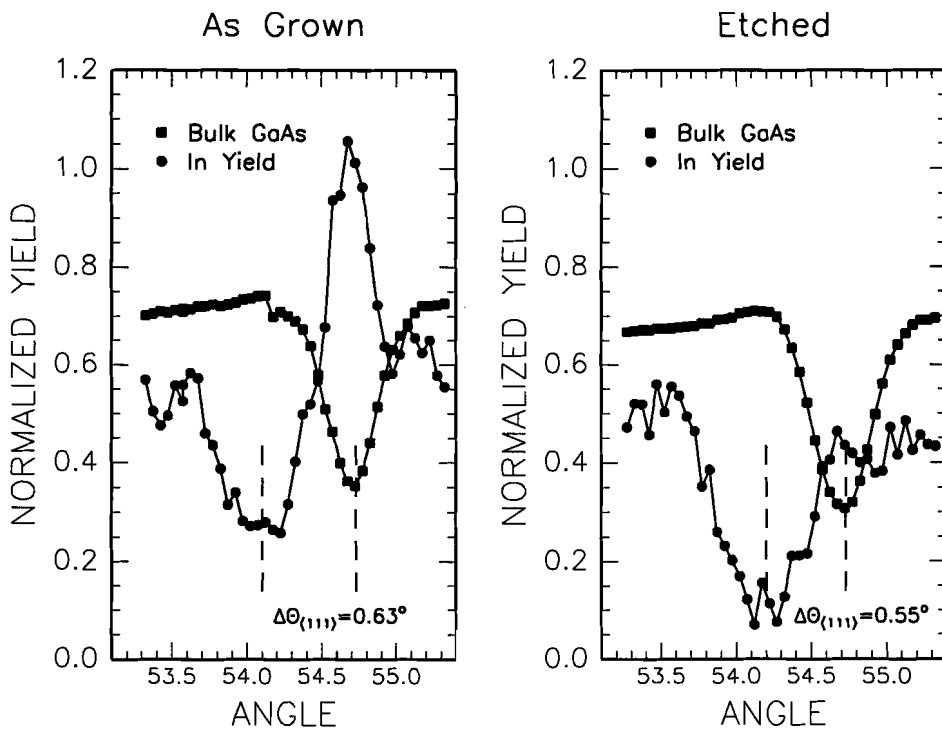


**Figure 5.10:** Angular scan measurements in the  $(110)$  plane through the  $\langle 111 \rangle$  axes, carried out on the ‘as grown’ sample and directly after plasma etching of the heavily doped 40 nm GaAs top layer. The horizontal scale is with respect to the  $\langle 100 \rangle$  axis near the surface normal. Tetragonal distortion in the InGaAs layer has been observed in both cases. The strain is determined from the measured angular shifts,  $\Delta\theta_{\langle 111 \rangle}$ , which are indicated in the figure. Straight-forward interpretation of the positions of the minima results in angular shifts of  $\Delta\theta_{\langle 111 \rangle} = 0.63 \pm 0.02^\circ$  for the as grown sample and  $\Delta\theta_{\langle 111 \rangle} = 0.55 \pm 0.01^\circ$  for the etched sample.

therefore in an overestimation of the the angular shift and consequently an overestimation of the strain in the  $\text{In}_{0.15}\text{Ga}_{0.85}\text{As}$  layer. In this case the other characteristic points in the measured  $\langle 111 \rangle$  In angular scans can be taken into account. Evaluation of the position of the In yield in the scan of the 'as grown' sample and the angular scan of the etched sample at half-minimum, near  $53.7^\circ$ , would be a good comparison to determine whether plasma induced strain relaxation has occurred. The observed overlap of both curves at this edge suggests that no strain relaxation has been induced by the  $\text{CH}_4/\text{H}_2/\text{Ar}$  reactive plasma treatment.

#### 5.4.4 Conclusions

The effects of dry plasma etching of the GaAs capping layer of a GaAs/AlGaAs/InGaAs/GaAs heterostructure on the strain and crystalline quality of the InGaAs layer have been studied with Rutherford backscattering spectrometry and ion channeling. A pile-up-rejection-circuit was necessary to reach a detection limit sufficiently low to detect a background free In signal. Nevertheless, the In areal density in the samples of interest (typical  $4 \times 10^{15}$  at/cm<sup>2</sup>) is close to the detection limit for 4 MeV 170 degree  $\text{He}^+$  RBS. Investigation of the Ga and As surface peaks in the aligned  $\langle 100 \rangle$  spectra revealed a number of point defects ( $8 \times 10^{15}$  at/cm<sup>2</sup>) in the top 50 nm which can be ascribed to the etching procedure.

The strain of the GaAs/AlGaAs/InGaAs/GaAs structures has successfully been determined from angular scans in the (110) plane through the  $\langle 111 \rangle$  axes using 4 MeV  $\text{He}^+$  ions. No indisputable shift of the In angular scan was observed after the plasma treatment. Due to the presence of fluxpeaking and steering effects an asymmetrical shape of the In angular scan was observed for the analysis of the 'as grown' sample, hereby introducing an extra shift of the indium minimum of the angular scan. This effect is likely to occur since the angular shift  $\Delta\theta_{\langle 111 \rangle}$  is of the order of the characteristic angle for channeling,  $\Psi_{\langle 111 \rangle} = 0.55^\circ$ . The position of the downward edges of both In  $\langle 111 \rangle$  scans, near  $53.7^\circ$ , is equivalent. This suggests that no strain relaxation of the InGaAs layer has been induced by the  $\text{CH}_4/\text{H}_2/\text{Ar}$  reactive plasma treatment.

A more detailed interpretation of the flux peaking effects in the angular scans is only possible when additional trajectory simulations are carried out. Simulation of the scans for the mentioned

structure with LAROSE requires modification of the standard code since the InGaAs zinc-blende lattice is represented by a pile of element III and element V elements on top of each other. This alternation is not implemented in the standard code that was used to simulate the SiGe strained layers.

Characterisation of the heterostructures is also possible with complementary techniques which give additional information on the sample structure and sample composition. Alternative IBA techniques recommended for further study of these samples are the measurement of the In signal with PIXE or use of NRA which profits from enhanced nuclear scattering cross-section. NRA has been used to detect P in InP samples as described in the next chapter.

## **5.5 Summary and conclusions**

Defect analysis and characterisation of crystalline quality and strain have been subject of study in this chapter. Three different types of samples have been characterized with high-energy ion channeling. Section 5.2 presented the measured damage depth profile of a 4 micron thick SiGe layer grown on (100)Si. The use of 6 MeV He<sup>++</sup> ions in this defect-depth-profiling experiment was necessary to obtain a background-free germanium peak from which the defect density could be determined. The observed disorder profile showed that the number of defects in the top 0.6  $\mu\text{m}$  was smaller than  $0.4 \times 10^5$  dislocation lines per cm. A significant increase of the total number of defects is detected at the depth interval between 1.0  $\mu\text{m}$  and 2.0  $\mu\text{m}$ . Beyond a depth of 2.5  $\mu\text{m}$  the total disorder does barely increase further. The quantification of the number of defects resulted in  $4.6 \times 10^5$  dislocation lines per cm, which is within ~20% of the expected number of defects. The sensitivity for the detection of line dislocations in the near-surface region in a SiGe sample is  $0.2 \times 10^5$  dislocation lines per cm.

Successful damage depth profiling studies have been carried out on APCVD grown SiGe and SiGeC layers (section 5.3). The RBS spectra obtained from a 743 nm SiGeC film on (100)Si confirmed the presence of defects in the layer and line dislocations at the SiGeC/Si interface. Detailed analysis and quantification of the defect density confirms the presence of  $2.3 \times 10^5$  interfacial defects at the SiGeC/Si interface and  $1.4 \times 10^5$  dislocation lines per cm in the top layer.

The number derived from the measured disorder profile is significantly larger than expected on behalf of a suggested straight-forward estimation. This suggests that extensive defect clusters or different defect types are due to the measured enhanced aligned scattering yield. The dominant defect should be assigned before quantification of the number of defects is carried out.

Characterization of a series of SiGeC samples with ~2 at% C showed that the crystalline damage in the pseudomorphic layers is below the detection limit for channeling. Strain measurements on these heterostructures showed that the incorporated carbon does not fully contribute to the strain compensation as calculated using theory of bulk elasticity. Only a typical fraction of 50% of the present carbon in these layers contributes to the strain compensation.

The third study (section 5.4) has been carried out on the effect of a plasma treatment on the strain of a GaAs/AlGaAs/InGaAs/GaAs heterostructure using high-energy ion channeling. The 4 MeV He<sup>+</sup> ions were necessary to obtain a separated In signal in the glancing-angle RBS experiments and to reduce the ion steering effects at the interfaces. The choice for this particular ion energy compromises between sufficient In peak separation and sufficient sensitivity for In. The <111> scans obtained from the integrated In signal in the backscattering spectra showed that the InGaAs layer was compressively strained. No significant strain relaxation of this layer was observed after the plasma treatment. Slight differences in the magnitude of the Ga and As surface peaks in the aligned spectra were observed which points to amorphisation of a near surface region of the sample due to the plasma treatment. Quantification indicates that the increase can be appointed to an increase of  $8 \times 10^{15}$  at/cm<sup>2</sup> randomly displaced atoms in the top layer.

## References

1. E. Bøgh, Can. J. Phys. 46 (1968) 653.
2. J.W. Mayer, L. Eriksson, S.T. Picraux and J.A. Davies, Can. J. Phys. 46 (1968) 663.
3. J. Mory and Y. Quéré, Rad. Effects 13 (1972) 57.
4. L.C. Feldman, J.W. Mayer and S.T. Picraux, *Materials analysis by ion channeling*, Academic Press N.Y., 1982.
5. Y. Quéré, Phys. Status Solidi 30 (1968) 713.

6. Y. Quéré, J. Nucl. Mat. 53 (1974) 262.
7. S.T. Picraux, E. Rimini, G. Foti and S.U. Campisano, Phys. Rev. B 18 (1978) 2078.
8. S.T. Picraux, J.A. Knapp and E. Rimini, (1982)
9. D.J. Gravesteijn, private communication.
10. M. Bozoian, Nucl. Instr. and Meth. B58 (1991) 127.
11. L.R. Doolittle, Nucl. Instr. and Meth. B9 (1985) 344.
12. S.T. Picraux, J.A. Davies, L. Eriksson, N.G.E. Johansson and J.W. Mayer, Phys. Rev. 180 (1969) 873.
13. D. Hull, *Introduction to dislocations*, Pergamon Press Oxford, 1975.
14. T.L. Alford, A.E. Bair, Z. Atzmon, L.M. Stout, S.G. Balster, D.K. Schroder, and R.J. Roedel, accepted for publication in *Thin Solid Films* (1995)
15. Z. Atzmon et al., Appl. Phys. Lett. 65 (20), 1994.
16. R. People, IEEE J. Quantum Electron., QE22 (9), (1986) 1696.
17. R. Braunstein, A.R. Moore and F. Herman, Phys.Rev. 109 (1958) 695.
18. J.C. Bean, L.C. Feldman, A.T. Fiory, S. Nakahara and I.K. Robinson, J. Vac. Sci. Technol. A2 (1984) 436.
19. R.A. Soref, J Appl. Phys. 70, (1991) 2470.
20. J.F. Ziegler and J.E.E. Baglin, J. Appl. Phys. 42 (1971) 2031.
21. C.M. van Es et al., J. Appl. Phys. 74, (1993) 6242.
22. A. Kozanecki, W.P. Gillin and B.J. Sealy, Appl. Phys. Lett. 64 (1994) 40.
23. J.G. van Hassel, *Dry processing of GaAs-based MESFETs and pseudomorphic HFETs* (Eindhoven University of Technology 1995), PhD thesis.
24. A. Kozanecki, B.J. Sealy, C. Jaynes, W.P. Gillin and R.Grey, Nucl. Instr. and Meth. B85 (1994) 192.

# 6

## **Analysis of InP with channeling nuclear reaction analysis; vibrational amplitudes of In and P**

*In this chapter a study is presented on the use of NRA- and RBS-channeling for the determination of the vibrational amplitude of In and P atoms in a diatomic InP crystal. These vibrational amplitudes are required to interpret angular scans of heterostructures with Monte Carlo calculations by introducing those vibrational amplitudes of In and P independently. Since literature reports a range of values for the vibrational amplitudes in InP a detailed study on the variation of the half-angle and the minimum yield with vibrational amplitude has been carried out. The use of NRA combined with RBS provides a unique possibility to interpret the In and P angular scans independently since the angular scans of the P atoms are sorted from the NRA spectra while the angular scans of the In atoms are sorted from the RBS spectra. The simulation program is modified to provide this independent angular-scan calculation of In and P atoms.*

*The simulations of the  $\langle 111 \rangle$  and  $\langle 110 \rangle$  angular scans showed that the In and P  $\langle 111 \rangle$  scans had equal minimum yield and scan-widths while the minimum yield and half-widths of the In and P  $\langle 110 \rangle$  angular scans differ. This difference can be explained qualitatively by the a modified single-string continuum theory as proposed by Bai and Nicolet. Monte Carlo calculations provide a detailed match of simulated angular scans with the measured angular scans. We obtained the RMS values for the one-dimensional vibrational amplitudes of the In and P atoms: 14 pm for the In atoms and 11 pm for the P atoms in the zinc-blende InP lattice. Comparison of the angular-scan simulations with the measured angular scans demonstrates that the vibrational amplitude can be determined with an accuracy of 0.001 nm. The values of the RMS vibrational amplitudes are within the range of values that is reported in literature. However, our results show that the vibrational amplitude of the light element (P) is smaller than the vibrational amplitude of the heavy element (In). This effect is not expected from theoretical models.*

## 6.1 Introduction

InP substrates are frequently used in III-V technology for fabrication of InP-InGaAsP based material e.g. dielectric waveguides and 1.1 $\mu$ m-1.6 $\mu$ m long-wavelength semiconductor lasers which are of considerable interest for optical-fiber communications [1]. Reliable data of the individual vibration amplitudes of In and P are essential as input parameters for ion trajectory calculations necessary to simulate measured angular scans, needed for strain analysis. In the literature many contradictory values for the vibrational amplitudes are published. Theoretical calculations of the Debye-Waller factor based on theoretical lattice-dynamical models have been reported by Talwar and Agarwal [2] and earlier by Vetelino and coworkers [3]. Both papers reported a one-dimensional vibrational amplitude  $u_i$  of 8.0 pm for both atomic species. Reid [4] used the valence shell model and reported values of 10.7 pm for In and 8.6 pm for P in the zinc-blende lattice. Experimental techniques used to measure the vibrational amplitudes were neutron diffraction [5], where phonon spectra are measured, and X-ray diffraction [6][7][8], where the intensity of the detected x-rays is studied as a function of temperature. Dygo and Turos obtained the thermal surface-atom vibrations from surface studies of III-V compound semiconductors using 2 MeV He RBS-channeling [9]. The values of the thermal vibration amplitudes, 11.6 pm for In and 11.4 pm for P, were obtained from evaluation of a backscattering surface peak in a measured  $\langle 100 \rangle$  aligned energy spectrum of a (100) oriented InP single crystal. Their measured data was evaluated with simulations of the aligned backscattering spectrum where the one-dimensional vibrational amplitude was included as input parameter. Thus the values for the RMS vibrational amplitudes  $u_i$  at room temperature (293K) vary from 8.0 pm to 11.6 pm for In and from 8.0 pm to 13.7 pm for P if all studies are included.

The application of high-energy ion channeling provides the unique possibility to study both the In and the P atoms independently by using RBS and NRA, respectively. The width of the angular scans is a direct measure of atomic vibrations along the atomic strings which form the channel. The magnitude of the vibrational amplitude of the individual In and P atoms in the InP lattice was obtained from comparison of the measured angular scans with the simulated scans along the  $\langle 110 \rangle$  and  $\langle 111 \rangle$  direction. For this purpose the standard LAROSE MC code has been modified to simulate ion trajectories in a zinc-blende diatomic crystal and the vibrational amplitude has

been specified as an independent input parameter for both P and In.

The measured <110> and <111> angular scans of the In yield and the P yield are obtained from simultaneously measured RBS and NRA spectra, respectively, using the  $^{31}\text{P}(\alpha, \text{p})^{34}\text{S}$  reaction. This is an exothermal reaction ( $Q=631.6$  keV) which in principle provides the opportunity to detect the energetic protons in an almost background-free condition. However, in case of characterisation of InP the energy of the detected protons interferes with the energy of detected alpha particles, elastically scattered from In. Furthermore, cross sections for the nuclear reaction are typical 0.3 mbarn/sr while cross sections for elastic scattering from In is 808 mbarn/sr. Therefore discrimination of the scattered alpha particles from the protons is required. The application of the  $^{31}\text{P}(\alpha, \text{p})^{34}\text{S}$  nuclear reaction for depth profiling has been examined by Segeth et al. [10] who used the 2.79 MeV and 3.048 MeV resonances. Resonant NRA has also been applied by McIntyre et al. [11] who used the 3.64 MeV and 3.97 MeV resonances. The resonance data is of great help in the interpretation of the energy spectrum of the detected protons. Details on the scattering geometry and the experimental setup are given in section 6.2. The obtained RBS and NRA spectra are discussed in section 6.3.

The measured width of the <110> and <111> angular scans is correlated with the critical angle for channeling  $\Psi_c$  and Lindhard's characteristic angle for channeling  $\Psi_l=(2Z_1Z_2e^2/Ed)^{1/2}$  as presented in section 1.5 of this thesis. From a classical viewpoint, a positively charged particle is channeled with respect to a row of atoms if it is incident upon the row at some angle  $\Psi$ . This angle has to be small that it is reflected away from the row by a correlated series of many consecutive glancing collisions with atoms in the row. As the incidence angle becomes greater than some critical angle  $\Psi_c$ , the particle begins to approach the row so closely, within the critical distance  $r_{\min}$ , that the trajectory no longer can remain channeled. Instead, the particle will rapidly be scattered away from the row by single or at most a few collisions with individual atoms in the row. Lindhard described the moving swift ions as an interacting charge in a single-string screened Coulomb continuum potential of atoms with charge  $Z_2$  and with atomic spacing  $d$  along the string. The conditions for the validity of the continuum approximation in axial channeling are discussed by Lindhard [12] where he also suggests that the critical distance ( $r_{\min}$ ) is



approximately the Thomas-Fermi screening distance ( $r_{\min} \sim a_{TF}$ ). Inserting this value in Lindhard's equation for the critical angle resulted in  $\Psi_c = 0.83 \Psi_1$ . For channeling in a non-static lattice Lindhard proposed incorporation of the vibrating strings by simply taking the sum of the squared screening distance,  $a_{TF}^2$ , and the squared transverse vibrational amplitude,  $u_2^2$ , for  $r_{\min}^2$ . Expressions for the temperature-dependent continuum potentials for rows and planes of thermally vibrating atoms have been given by Appleton et al. [13].

The continuum, single-string model of channeling, with the inclusion of atomic vibrations has been used by Andersen [14] to calculate the shape of channeling dips who compared with experimental results for  $H^+$  in W. In Monte Carlo simulations of Barrett [15] the channeling phenomenon was calculated in a classical ion-atom collision model where the half-width of the axial dip was compared to the characteristic angle. A proportionality relation between  $\Psi_{1/2}$  and  $\Psi_1$  was found:  $\Psi_{1/2} = \alpha \Psi_1$ , where the factor  $\alpha$  is a function of the one-dimensional vibrational amplitude,  $u_1$ , and the Thomas-Fermi screening distance. Barrett found an expression for the critical angle for axial channeling,  $\Psi_c^B = 0.83 F_{RS}(\xi) \Psi_1$ , which was obtained from a comparison of angular scan widths obtained from simulations and experimental values of  $\Psi_{1/2}$ . Here  $\xi$  is the normalized critical distance  $\xi = 1.2u_1/a_{TF}$ . The values of  $F_{RS}$  versus  $\xi$  are tabulated. Barrett's work also suggests a dependence of the observed minimum yield in a near-surface depth interval, hereby incorporating the atomic vibrations. Barrett compared the calculated values for the minimum yield for axial channels with experimental data of Davies et al. [16]. These results fit the equation  $\chi_{\min} = Nd\pi(0.2a_{TF}^2 + 3u_2^2)$ . This suggests that the term of the screening length is sufficiently small that it can usually be neglected. Also the magnitude of the observed minimum yield is largely depending on the vibrational amplitude of the atoms.

Ion channeling experiments with a diatomic  $UO_2$  single crystal have been reported by Eriksson and Davies [17]. They monitored deuterons from wide-angle scattering of the uranium atoms and of the  $^{16}O(d,p)^{17}O$  reaction and measured the angular dependence of the interaction of these 0.975 MeV deuterons with both the oxygen and uranium atoms independently. They observed that the two processes exhibited completely different orientation dependencies. To explain these differences the channeling continuum theory has been extended for channeling in a biatomic

lattice. Bai et al. [18] analyzed a thin polyatomic film of  $\text{ReSi}_2$  on  $\text{Si}(100)$  substrate and observed a similar orientation dependence. They observed a different half-angle ( $\Psi_{1/2}$ ) for the rhenium and silicon signal of the  $\langle 100 \rangle$  axial direction and observed that the minimum yield of the light element (Si) was far greater than the minimum yield derived from the backscattering yield of the heavy element (Re). These results have been explained by a model which describes the lattice in terms of biatomic strings. The model explains differences in half-angle and minimum yield of the measured In and P angular scans qualitatively without incorporation of the vibrational amplitudes of the atoms and is used to interpret the angular scans. The measured  $\langle 110 \rangle$  and  $\langle 111 \rangle$  angular scans are presented in section 6.3 and interpretation of these scans is extensively treated in section 6.4.

A quantitative interpretation of the measured  $\langle 110 \rangle$  and  $\langle 111 \rangle$  angular scans of the InP sample is obtained from LAROSE MC calculations which incorporated the values for the different atomic vibrational amplitudes. Modification of the code was necessary for correct interpretation of the angular scans as is described in detail in section 6.5. Section 6.6 shows the effect of incorporation of the atomic vibrations on the minimum yield and scan width of the  $\langle 110 \rangle$  and  $\langle 111 \rangle$  simulated angular scans. The LAROSE code has been used to reproduce the measured angular scans in detail using the individual vibrational amplitudes as parameters. The simulations that resemble the measured angular scans in detail are presented in section 6.6. Finally section 6.7 summarizes conclusions concerning the method and of the magnitude of the obtained RMS vibrational amplitudes.

## **6.2 Experimental details**

The measurements on the InP sample have been carried out with a 50 nA, 4 MeV  $\text{He}^+$  beam from the 3-30 MeV Eindhoven AVF-cyclotron. The beam divergence was limited to  $0.07^\circ$  by means of the collimator slits. NRA spectra have been measured for the (100) oriented InP substrate simultaneously with the RBS spectra measured at a scattering angle of  $170^\circ$ . The RBS spectra, obtained with the 50  $\text{mm}^2$  PIPS detector, are used to monitor the In yield as a function of depth while the NRA spectrum is used to obtain the P yield as a function of depth. The 900  $\text{mm}^2$  NRA detector is used for the detection of protons from the  $^{31}\text{P}(\alpha, \text{p})^{34}\text{S}$  reaction and is located at

$\theta=140^\circ$ . Phosphorus is detected applying the  $^{31}\text{P}(\alpha,\text{p})^{34}\text{S}$  reaction. The energy of protons, resulting from an  $(\alpha,\text{p})$  reaction at the surface, is 3.7 MeV, assuming an incident  $\text{He}^+$  ion energy of 4 MeV while the  $\text{He}^+$  ions have an energy of 2.5 MeV when elastically scattered from surface phosphorus. At an angle of  $140^\circ$  (NRA detector) elastically scattered ions from In at the surface are detected with an energy of 3.5 MeV. Since the nuclear-reaction cross section for  $^{31}\text{P}(\alpha,\text{p})^{34}\text{S}$  is about five orders of magnitude smaller than the cross section for elastic scattering from indium (0.3 mbarn/sr [19] and 808 mbarn/sr, respectively), suppression of the scattered He ions is indispensable. This is achieved using a stopper foil, mounted in front of the NRA detector, as is usually applied in Elastic Recoil Detection Analysis (ERDA). A 10  $\mu\text{m}$  thick aluminum stopper foil, placed in front of the large 900  $\text{mm}^2$  PIPS backscattering detector, is sufficient to slow down the 3.5 MeV He ions to 1.1 MeV while the emitted protons only lose 190 keV of their kinetic energy. Consequently, the proton yield is visible in the NRA detector, virtually background-free, as a single peak in the energy spectrum. The reduced number of detected  $\text{He}^+$  ions is small enough to prevent pile-up in the spectral region of interest.

The energy calibration has been obtained from measured energy spectra of an AmCm source (5443 keV, 5486 keV, 5764 keV and 5805 keV) which was used for both detectors. The energy of the emitted  $\alpha$ -particles, after passing through the aluminum foil, is calculated using ZBL stopping powers from TRIM [20]. Proper calibration provides the energy scales of both RBS and NRA spectra, required to select identical depth intervals for In and P which is necessary for comparison of the measured angular scans with the scans obtained from MC calculations.

### 6.3 Results

The spectrum along the  $\langle 100 \rangle$  axis and the azimuthally averaged random spectra of the InP(100) crystal have been measured to determine the minimum yield. Subsequently angular scans through the  $\langle 110 \rangle$  axis and through the  $\langle 111 \rangle$  axis have been measured to determine the minimum yield and the angular scan widths obtained from the In and P signals.

Figure 6.1 depicts energy spectra of the RBS and NRA detector for the azimuthally averaged random and for the  $\langle 100 \rangle$  aligned crystal orientation. The random NRA spectrum shows a rapid

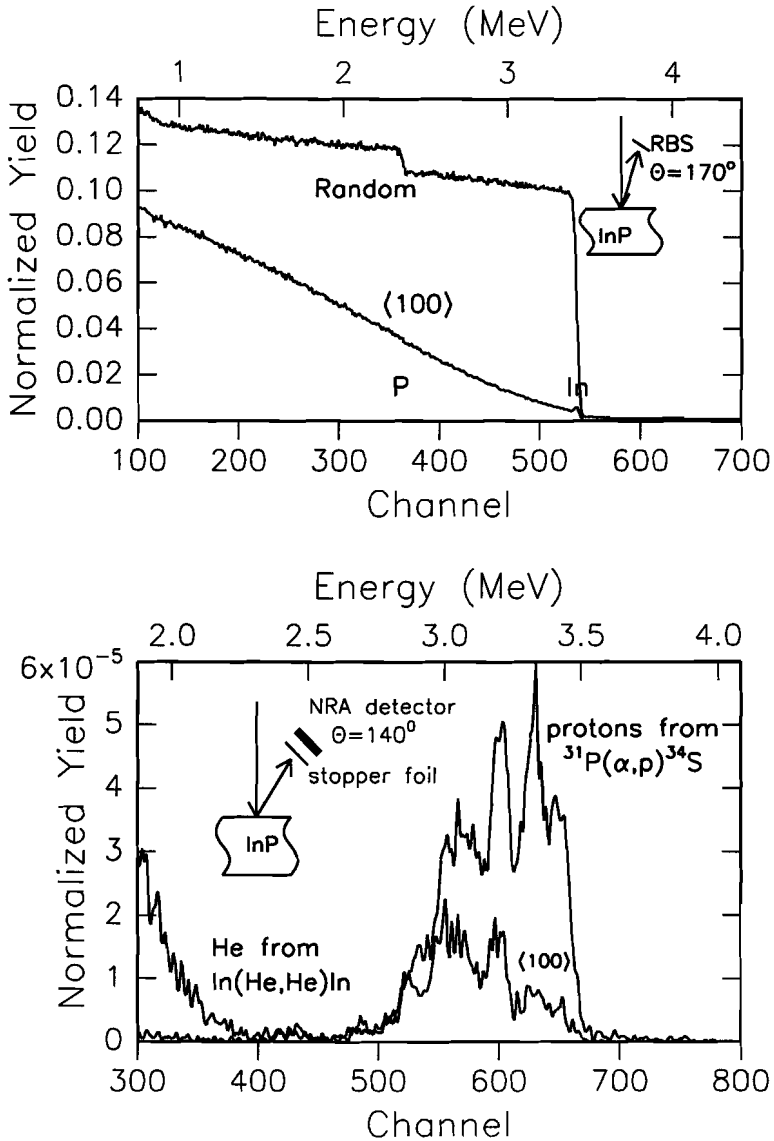


**Figure 6.1:** Energy spectra of the RBS and NRA detector for the azimuthally averaged random and for the  $\langle 100 \rangle$  aligned crystal orientation of the  $(100)$  InP substrate. The random RBS spectrum depicts the In scattering yield and a step in the yield at the surface position of phosphorus which is indicated in the top figure. The random NRA spectrum depicts a rapid variation of the yield with energy resulting from the resonances in the  $^{31}\text{P}(\alpha,p)^{34}\text{S}$  nuclear reaction cross section. The low-energy region in the NRA spectrum depicts pile-up from scattered He ions that still penetrate the stopper foil.

variation of the yield with energy resulting from the resonances in the nuclear reaction cross section. The low energy region of the NRA spectrum shows the yield originating from the detection of scattered  $\text{He}^+$  ions that penetrated the aluminum stopper foil. The random RBS spectrum shows the In scattering yield and a small step in the yield at the surface position of phosphorus. The  $\langle 100 \rangle$  channeling spectra have been obtained after sample alignment with the incident ion beam. The measured minimum yields determined from the In and P yields, just behind the surface peaks in the RBS and NRA spectra, are:  $\chi_{\min} = 0.03$  for indium and  $\chi_{\min} = 0.08$  for phosphorus. This experiment shows that RBS combined with NRA allows independent measurement of depth profiles of the heavy and light element in the (100)InP sample.

Angular scans have been measured through the  $\langle 110 \rangle$  channel in the (100) plane and through the  $\langle 111 \rangle$  axis in the (110) plane. Spectral windows have been selected in the obtained RBS and NRA spectra, corresponding to the identical depth interval in the sample; between  $635\text{\AA}$  and  $2350\text{\AA}$ . This depth interval was selected to avoid deformation of the angular scan by dechanneling at large depths or by the surface peak. Moreover it allowed a comparison with MC calculations without entering extreme long execution times. The angular scans have been obtained from 30 NRA and RBS spectra that were acquired for 5 minutes each and were normalized with respect to the random yield.

Figure 6.2 shows the angular scans through the  $\langle 110 \rangle$  direction in the (100) plane and through the  $\langle 111 \rangle$  axis in the (110) plane. The target orientation is with respect to the  $\langle 100 \rangle$  axis near the sample normal. The half-angles ( $\Theta_{1/2}$ ) and minimum yields ( $\chi_{\min}$ ) are determined from both the indium and the phosphorus scans for each axis. The measured width of the In and P angular scans are identical for the  $\langle 111 \rangle$  axis. On the contrary the width of the  $\langle 110 \rangle$  angular scans differ. This is qualitatively explained by the model of Bai et al. which describes the crystal sublattice in terms of atomic strings and will extensively be discussed in section 6.4. The  $\langle 111 \rangle$  orientation can be described by one type of atomic string consisting of alternating In and P atoms while the  $\langle 110 \rangle$  orientation distinguishes two types of strings, either In or P. The measured minimum yield for axial channeling in the  $\langle 111 \rangle$  direction is identical for both elements while one for  $\langle 110 \rangle$  axial channeling is larger for the light element (P). In addition the normalized

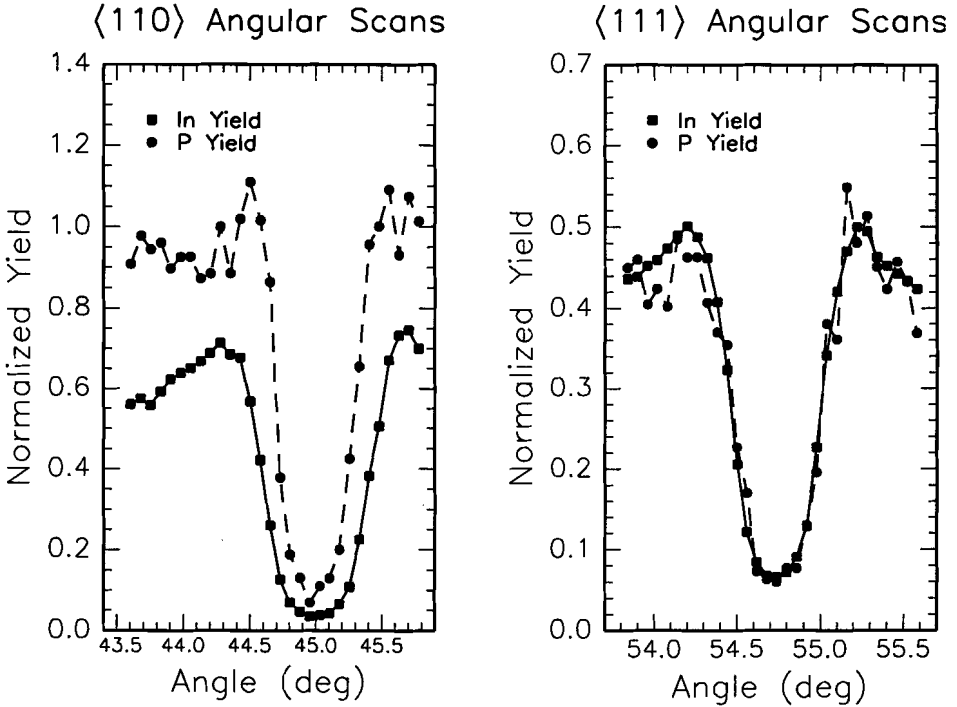


**Figure 6.2:** Angular scans of the In and P yield. Scans have been measured through the  $\langle 110 \rangle$  axis in the (100) plane and through the  $\langle 111 \rangle$  axis in the (110) plane. Sample orientation is with respect to the  $\langle 100 \rangle$  axis. The obtained In and P angular scans are identical for the  $\langle 111 \rangle$  direction while a different minimum yield and scan width is observed for the  $\langle 110 \rangle$  direction.

(100) planar yield, observed at the shoulders of the  $\langle 110 \rangle$  P scan, reaches unity while the normalized In (100) planar yield stays far below unity. This indicates that in-plane channeled ions remain channeled by the In planes but are likely to dechannel by the P planes and scatter from phosphorus as is also qualitatively explained by the model of Bai et al..

#### 6.4 Minimum yield and critical angle for a diatomic lattice

Typical quantities determined in an ion-channeling experiment are minimum yield,  $\chi_{\min}$ , and angular scan half-width,  $\Psi_{1/2}$ . The minimum yield is calculated from the backscattering yield in the aligned spectrum just behind the surface peak, extrapolated to the surface position, with respect to the backscattering yield for a random orientation of the sample. This ratio is defined

as  $\chi_{\min}$ . The concept of calculation of  $\Psi_{1/2}$  and  $\chi_{\min}$  for ions that channel in a diatomic crystal is briefly summarized below.

The quantification of the minimum yield and the half-angle in a diatomic lattice such as InP is understood when the crystallographic orientations are treated as single atomic strings along those directions. The continuum-string potential, as introduced by Lindhard, can be modified by considering those atomic strings of In and P atoms as suggested by Bai and Nicolet. In the  $\langle 111 \rangle$  orientation the projectiles are directed along one type of atomic string, consisting of alternating In and P atoms (InP). In the modified continuum theory the minimum yield and critical angle are calculated using the average atomic number and average lattice spacing along the row. Consequently angular scans obtained from both elements will be identical with the same minimum yield and same half-width. When the projectiles are directed along the  $\langle 110 \rangle$  (or the  $\langle 100 \rangle$ ) orientation two types of atomic strings occur; i.e. strings of In atoms and strings consisting of P atoms. For this orientation a single-column potential approximation for each type of string is required. The distance of closest approach to the In column and the P column are  $r_{\min}^{\text{In}}$  and  $r_{\min}^{\text{P}}$ , respectively, corresponding to critical angles for the different strings,  $\Psi_c^{\text{In}}$  and  $\Psi_c^{\text{P}}$ . Note that  $\Psi_c^{\text{In}} > \Psi_c^{\text{P}}$  since the critical angle is proportional to  $Z^{1/2}$ . Thus the angular scan obtained from the heavy atomic string (In) is wider due to the larger critical angle  $\Psi_c^{\text{In}} > \Psi_c^{\text{P}}$ . The observed difference in half-width is significant due to the large difference in atomic number for In and P.

Ions that initially interact with the P string are steered away and leave this string under an angle  $\Psi$ , smaller or equal to the critical angle for channeling for the P string ( $\Psi \leq \Psi_c^{\text{P}}$ ). Subsequently ions approach the In or P string under this angle. In case the ions subsequently interact with the In string the distance of closest approach is the distance  $r^{\text{In}}$ , which is significantly larger than the critical distance for the P string  $r_{\min}^{\text{P}}$  ( $r^{\text{In}} > r_{\min}^{\text{P}}$ ). Thus the observed blocked area for ions that initially interacted with the P string is equal to  $\pi(r_{\min}^{\text{P}})^2 + \pi(r^{\text{In}})^2$ .

Ions that initially interact with the In atomic string only scatter from an In atom when the critical distance to the string is smaller or equal to  $r_{\min}^{\text{In}}$ . The corresponding blocked area is  $\pi(r_{\min}^{\text{In}})^2$ . In case the ions interact subsequently with the P string the ions might approach within the critical

distance  $r_{\min}^P$  due to the high transverse kinetic energy of the ions which originate from the In string and consequently these ions contribute to the scattering yield of phosphorus. However, the ion will only contribute to the scattering yield of In when entered within the area  $\pi(r_{\min}^{\text{In}})^2$ . Thus the probability for scattering by the heavy (In) atomic string is much smaller than the probability for scattering by the light (P) atomic string and this explains the low minimum yield observed for the heavy (In) element.

Bai and Nicolet explained their observed results in a qualitative manner with this model but circumvented the incorporation of the vibrational amplitudes of the Re and Si atoms. This property needs to be included when detailed comparison of simulated and measured angular scans is desired. Incorporation is essential when angular scans obtained at elevated temperatures are evaluated with help of these trajectory simulations. Hence our measured angular scans are interpreted with LAROSE MC trajectory calculations that incorporated the value of the vibrational amplitude of the distinct elements. For these simulations changes of the standard code needed to be implemented.

## **6.5 LAROSE Modifications**

The original version of LAROSE uses vibrational amplitudes derived from the Debye theory of thermal vibrations [21]. This theory assumes that the individual atoms vibrate independently and that in each of the translational degrees of freedom the probability of a displacement  $x$  has a Gaussian distribution with RMS value  $u_1 = \langle x^2 \rangle^{1/2} = \langle y^2 \rangle^{1/2} = \langle z^2 \rangle^{1/2}$ . The one-dimensional component of the vibrational amplitude must not be confused with the two-dimensional amplitude  $u_2$ . According to Debye theory the magnitude of the thermal-vibration amplitude is a function of the crystal temperature and the Debye temperature  $\Theta_D$ . This Debye temperature is related to the maximum frequency allowed in the solid: the Debye cutoff frequency  $\omega_D = k\Theta_D/\hbar$ . Values for the Debye temperature at  $T=293$  K for most commonly studied elements, having cubic structures, are reported by Gemmel [22] and references therein. At high temperature,  $T \gg \Theta_D$ ,  $\langle u_3^2 \rangle$  is proportional to the absolute temperature. At low temperature  $\langle u_3^2 \rangle$  approaches a constant and finite value corresponding to the zero-point motion of the solid. The Debye model is proven to be valid for monatomic crystals. The validity of this model in diatomic crystals raises



questions on the use of the proper Debye temperature and the subsequent calculation of the magnitude of the vibrational amplitudes of the individual atoms. We therefore modified the program and used the RMS value  $u_j$  as input parameter in the simulations, hereby circumventing the use of the Debye model. This value is treated as a property of the atomic species and is assigned to each element. For each calculated ion-atom interaction a displacement of the atom from its equilibrium site has been selected from a Gaussian distribution with RMS value  $u_j$ . For each atomic species a lookup-table is created with 1000 values for the displacement of the atom from its static-lattice location hereby taking into account that these displacements accumulate a Gaussian distribution with RMS value  $u_j$ .

Due to the ordered structure of the zinc-blende InP lattice the ion interacts with different elements along its trajectory through the crystal. The III-V crystal structure is an altering of atomic species. This order of appearance of the atomic species along the string depends on crystal orientation and has been implemented in the code by redefining the crystalline unit cell for each orientation. The interacting atomic species is administered while calculating the ion-trajectory. In this ion-trajectory calculation, where the ion-atom interaction is treated as a classical binary collision, the atomic position with respect to the static-lattice location is determined from the lookup-table of atomic displacements and the direction of the deflected ion is calculated. Subsequently interaction with the next atom is calculated. That atom might be of different species, depending on the crystallographic orientation under investigation. In this method of ion-trajectory calculation in polyatomic lattices different vibrational amplitudes can be assigned to the different types of atoms because the close-encounter probability is administered per atomic species. Angular scans for In can be distinguished from those of P in the simulations.

## 6.6 Angular-scan properties obtained from LAROSE trajectory simulations

Many simulations of  $\langle 110 \rangle$  and  $\langle 111 \rangle$  angular scans were carried out using different vibrational amplitudes for the In and P atoms. At first the vibrational amplitudes of indium atoms and phosphorus atoms were assumed equal. We used vibrational amplitudes between 5 pm and 20 pm. The minimum yields and the half-angles were determined from the simulated angular scans for both atomic species. The depth interval, chosen in the simulations, is identical with the depth

interval selected in the  $\langle 111 \rangle$  and  $\langle 110 \rangle$  RBS and NRA angular-scan measurements (between 635Å and 2350Å). This enables detailed comparison of the simulations with the experimental data. For analytical purposes, the half-angle  $\theta_{1/2}$  is defined as the full angular width of the scan at the particular height where the normalized yield is exactly half-way between the top of the shoulder of the scan and the minimum yield.

Figure 6.3 depicts the dependence of  $\theta_{1/2}$  and  $\chi_{\min}$  on the vibrational amplitude of the atoms for the  $\langle 110 \rangle$  scan in the (100) plane and the  $\langle 111 \rangle$  scan in the (110) plane. The results of the LAROSE MC calculations show In and P angular-scan widths and minimum yields that differ for the  $\langle 110 \rangle$  direction while these properties are identical for the  $\langle 111 \rangle$  direction. This is in qualitative agreement with the modified continuum theory of Bai for a diatomic crystal.

The observed minimum-yield increase in both the  $\langle 111 \rangle$  and  $\langle 110 \rangle$  directions is almost one order of magnitude while the vibrational amplitude  $u_i$  increases only from 5 pm to 20 pm which shows the extreme sensitivity of the high-energy channeling technique for atomic displacements. For the  $\langle 111 \rangle$  axis the observed dependence of the vibrational amplitude on the minimum yield is in agreement with the dependence proposed by Barrett:  $\chi_{\min} = Nd\pi(3u_2^2 + 0.2a_{TF}^2)$ , when using the (mean) vibrational amplitude ( $u_2 = \sqrt{2} \bar{u}_p$ , and  $\bar{u}_l = u_l^n = u_l^p$ ) and the (mean) Thomas-Fermi screening distance with  $Z_2 = 1/2(Z_2^{\text{In}} + Z_2^{\text{P}})$ . The In minimum yield observed for the  $\langle 110 \rangle$  axis is likely to be met with  $\chi_{\min} = N_{\text{In}}d\pi(r_{\min}^{\text{In}})^2$ , where  $N_{\text{In}}d$  is the density of In strings ( $N_{\text{In}}d = 1/2Nd$ ). When applying the Barrett equation for  $\chi_{\min} \langle 110 \rangle$  we observe that this straight-forward calculation agrees well with the indium minimum yield observed from the simulations. The value of the phosphorus  $\langle 110 \rangle$  minimum yield as is defined by Bai and Nicolet obeys  $\chi_{\min} = N_{\text{P}}d\pi(r_{\min}^{\text{P}})^2 + N_{\text{In}}d\pi(r^{\text{In}})^2$ . We observed that the second term in this equation, the extra contribution of the In strings to the P minimum yield, is not a constant but is a function of the vibrational amplitude. Quantification of the difference must be subject of further study. We suppose that the radius  $r^{\text{In}}$ , where the ion experiences a local potential  $U(r^{\text{In}})$ , must equal the potential  $U(r_{\min}^{\text{P}})$ . Search for a valid expression of a potential was beyond this study. The In and P half-angle of the  $\langle 111 \rangle$  direction is a function of the *average* atomic number of the string. The  $\langle 110 \rangle$  half-angles obtained from P and In differ. The  $\langle 110 \rangle$  angular scan of the In signal is

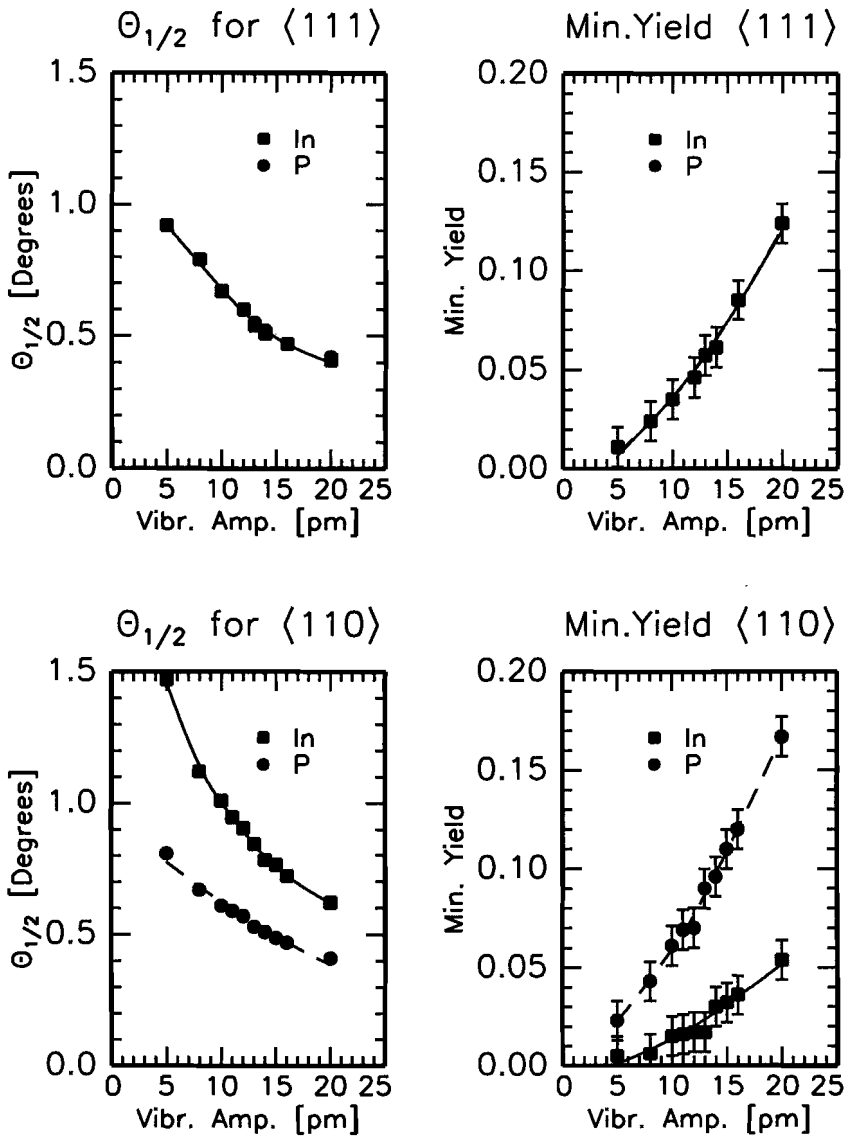


**Figure 6.3:** This figure depicts the dependence of  $\theta_{1/2}$  and  $\chi_{min}$  on the vibrational amplitude of the atoms for the  $\langle 110 \rangle$  scan in the (100) plane and the  $\langle 111 \rangle$  scan in the (110) plane. The close-encounter probability is averaged over a depth interval between 635 Å and 2350 Å. The LAROSE MC calculations show In and P angular widths and minimum yields that differ for the  $\langle 110 \rangle$  direction while these properties are identical for the  $\langle 111 \rangle$  direction. A significant minimum yield increase results from an increasing vibrational amplitude as is observed for both scans.

larger than the half-width of P which can be explained by the difference in atomic number  $Z_2$ . For small vibrational amplitudes (5 pm) a pure  $Z_2^{1/2}$  dependence is observed but for higher vibrational amplitudes the In and P angular-scan widths approach one another.

The simulations of the  $\langle 110 \rangle$  and the  $\langle 111 \rangle$  scans obtained with the incorporation of In and P vibrational amplitudes are plotted in figure 6.4 together with the measured  $\langle 110 \rangle$  and  $\langle 111 \rangle$  data. The best corresponding simulation with the  $\langle 111 \rangle$  measured angular scan is found for a mean vibrational amplitude of 13 pm for both In and P atoms since that simulation fit better than the ones where vibrational amplitudes of 12 pm and 14 pm were used. When mean vibrational amplitudes of 13 pm for both In and P atoms are used for simulation of the  $\langle 110 \rangle$  axis a slight discrepancy between the two scans is observed, the measured P scan was wider and the measured In scan narrower. We therefore modified the individual vibrational amplitudes hereby restricting that the *mean* vibrational amplitude was near 13 pm, since that value fit the  $\langle 111 \rangle$  In and P scans. The simulations of the individual In and P  $\langle 110 \rangle$  angular scans resemble the measurements in detail when RMS vibrational amplitudes of 14 pm for In atoms and 11 pm for P atoms are used. These values are significantly higher than reported in literature mentioned in section 6.1. We found that the light element (P) has a smaller vibrational amplitude than the heavy element (In) in the diatomic matrix. This is in disagreement with MRI calculations of Vetelino where the vibrational amplitude of the light element is significantly higher, especially for low temperatures.

## **6.7 Conclusions**

Combination of NRA and RBS can be used to determine the vibrational amplitudes of In and P atoms in the InP lattice from the measured  $\langle 111 \rangle$  and  $\langle 110 \rangle$  angular scans. The observed widths of the angular scans and minimum yields obey qualitatively the interpretation that proposes the single-string approximation in a continuum theory. However, this model is inadequate to determine the influence of the RMS amplitudes of the individual atoms in the diatomic crystal quantitatively. Interpretation of the measured scans with MC ion-trajectory calculations serves to quantify the RMS vibrational amplitude of the In and P atoms in the zinc-blende InP crystal independently.

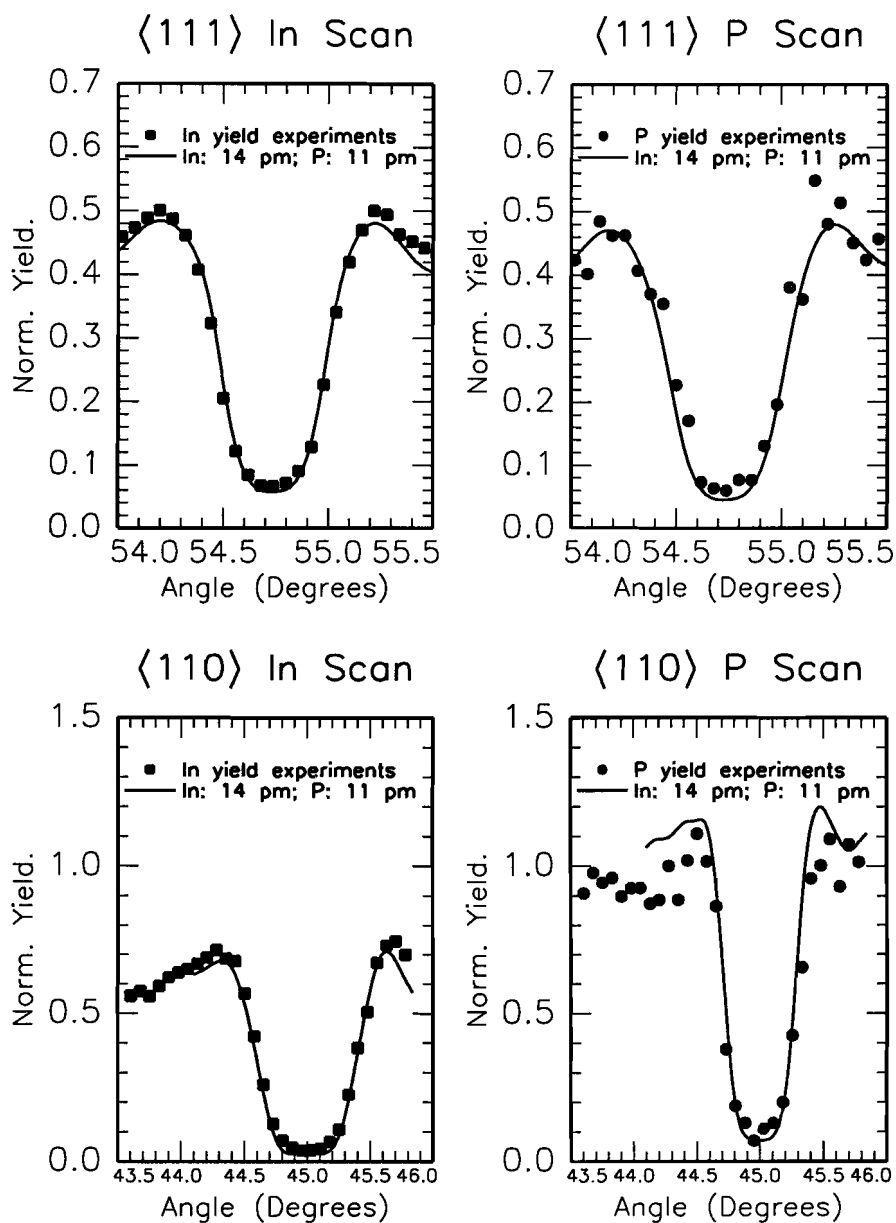


**Figure 6.4:** Comparison of angular-scan measurements with simulations. The simulations of the  $\langle 110 \rangle$  and the  $\langle 111 \rangle$  scans have been obtained with the vibrational amplitudes of 14 pm for the In atoms and 11 pm for P atoms. The depicted simulations are best fits with the measured  $\langle 110 \rangle$  and  $\langle 111 \rangle$  data.

Ion trajectory simulations show that the dependence of the minimum yield on the vibrational amplitude in the  $\langle 111 \rangle$  direction can be calculated using Barrett's equation:  $\chi_{\min} = Nd\pi(3u_2^2 + 0.2a_{TF}^2)$ , where an average  $Z_2$  is used for calculation of the Thomas-Fermi screening distance. Barrett's equation also predicts the In minimum yield for the  $\langle 110 \rangle$  direction. The minimum yield observed for the light (P) element is significantly larger as has been suggested in the theory. We observed that the difference of the P minimum yield with the In minimum yield is rapidly increasing with the vibrational amplitude of the atoms. The In and P half-angles of the  $\langle 111 \rangle$  direction are identical and are determined by the *average* atomic number of the string that consists of alternating In and P atoms. The half-width of the  $\langle 110 \rangle$  angular scan obtained from the In signal is larger than the half-width of P which is due to the difference in atomic number  $Z_2$ . For small vibrational amplitudes (5 pm) a pure  $Z_2^{1/2}$  dependence is observed but for higher vibrational amplitudes the In and P angular-scan widths approach each other.

Interpretation of the measured scans with MC ion-trajectory calculations serves to independently quantify the RMS vibrational amplitude of the In and P atoms in the zinc-blende InP crystal. Comparison of the individually measured  $\langle 111 \rangle$  and  $\langle 110 \rangle$  angular scans with these simulations enables determination of the vibrational amplitudes of both indium (14 pm) and phosphorus (11 pm) atoms with an accuracy of 1 pm.

## References

1. G.P. Agrawal and N.K. Dutta, *Long-wavelength Semiconductor Lasers*, Van Nostrand Reinhold Company Inc., New York, 1986.
2. D.N. Talwar and B.K. Agarwal, *J. Phys. C* 7 (1974) 2981.
3. J.F. Vetelino, S.P. Gaur and S.S. Mitra, *Phys. Rev. B* 5 (1972) 2360.
4. J.S. Reid, *Acta Crystallogr. Sec. A* 39 (1983) 1.
5. O.H. Nielsen et al., *Z. Physik* B52 (1983) 99.
6. V.T. Bublik and S.S. Gorelik, *Krist. Tech.* 12 (1979) 859.
7. M.G. Shumskii, V.T. Bublik, S.S. Grelik, M.A. Gorevich, *Sov. Phys.-Crystallogr.* 16 (1972) 674.

8. P.A. Flinn et al., Phys. Rev. 123 (1961) 809.
9. A. Dygo and A. Tuross, Phys. Rev. B 40 (1989) 7704.
10. W. Segeth, D. Bakema and D.O. Boerma. Proc. Int. Symp. on Three Day in Depth Review on the Nuclear Accelerator Impact in the Interdisciplinary Field. P.Mazzoldi and G Moschini (1984) 66.
11. L.C. McIntyre Jr., L.C. Leavitt, J.A. Dezfouly-Arjomandy and J.Oder, Nucl. Instr. and Meth. B35 (1988) 446.
12. J. Lindhard, Kgl. Danske Videnskab Selskab, Mat. Fys. Medd. 34 (1965) 14.
13. B.R. Appleton, C. Erginsoy and W.M. Gibson, Phys. Rev. 161 (1967) 330.
14. J.U. Andersen, Mat. Fys. Medd.: K.Dan. Vidensk.Selsk. 36 (1967) 7.
9. J.H. Barrett, Phys. Rev. B 3 (1971) 1527.
16. J.A. Davies, J. Denhartog and J.L. Whitton, Phys. Rev. 165 (1967) 345.
17. L. Eriksson and J.A. Davies, Arkiv för Fysik 39 (1969) 439.
18. G.Bai, M. Nicolet, J.E.Mahan and K.M. Geib, Phys. Rev. B 41,(1990) 8603.
19. N.A. Schier et. al., Nucl. Phys. A 254 (1975) 80.
20. J.F. Ziegler, J.P. Biersack and U. Littmark, *The Stopping and Ranges of Ions in Solids*, Vol. 1, Pergamon Press, New York.
21. M. Blackman, *Encyclopedia of Physics*, edited by S. Flügge (Springer, Berlin, 1955), Part I, Vol. 7, p. 377.
22. D.S. Gemmel, Rev. Mod. Phys. 46 (1974) 129.

# 7

## Stopping power of channeled He ions

*In this chapter a detailed study is presented on the stopping of He ions in a silicon crystal, using transmission channeling and Monte-Carlo trajectory calculations. The energy loss per unit path length is correlated to the local electron density in the silicon crystal and is calculated using the free-electron gas model proposed by Lindhard. The spatial charge-density distribution of the valence electrons has been obtained from bandstructure calculations. With the introduction of the spatial valence electron density distribution in Monte-Carlo trajectory calculations we are able to obtain average stopping-power differences in the axial  $\langle 111 \rangle$ ,  $\langle 110 \rangle$  and  $\langle 100 \rangle$  directions for sample thicknesses of several hundreds of nanometers. Transmission-channeling experiments have been carried out to measure energy distributions of transmitted ions for many different orientations resulting in angular scans which reveal the orientation dependence of the ion stopping. Energy-loss distributions for planar-channeled, axial-channeled and non-channeled ions are identified and qualitatively compared to the simulations.*

### 7.1 Introduction

The knowledge of the slowing down of ions when traversing matter is of fundamental importance in methods of materials analysis using beams of charged atomic particles. Depth perception follows directly from the energy loss of the probing particles and the energy loss affects both quantitative and compositional analysis. The physics of the energy-loss phenomena is complex, involving many kinds of interactions between the projectile ion with target nuclei and target electrons. Because of their significance in many fields of physics, these phenomena have been subject to intensive studies since the beginning of the century. The amount of energy loss per distance is often called stopping power or specific energy loss ( $S \equiv dE/dx$ ). The stopping cross section  $\epsilon$  is related to the specific energy loss by  $\epsilon = (1/N)dE/dx$ , where  $N$  is the volume density ( $\text{at}/\text{cm}^3$ ). Thus  $\epsilon = (1/\rho)dE/dx$ , where  $\rho$  is the mass density ( $\text{g}/\text{cm}^3$ ).



The relative importance of the various interaction processes between the ion and the target medium depend mostly on the ion velocity and on the charges of the ion and target atoms. At ion velocities  $v$ , significantly lower than the Bohr velocity  $v_0$  of the atomic electrons, the ion carries its electrons and tends to become neutralized by electron capture. At these velocities elastic collisions with the target atoms, i.e. the nuclear energy loss, dominates. As the ion velocity is increased the nuclear energy loss diminishes as  $1/E$ . The electronic energy loss, i.e., inelastic collisions with the atomic electrons, soon becomes the main interaction. The total energy loss is obtained as a sum of the nuclear and the electronic contributions. At higher velocities  $v \gg v_0$  the charge state of the ion increases and finally it becomes fully stripped of its electrons. At a given velocity the energy loss is proportional to the square of the ion charge. The electronic stopping power reaches a maximum for ion velocities near 0.4 MeV/amu. This is the energy region where Rutherford Backscattering Spectrometry is utilized, using 1.6-2 MeV He ions. For faster ions the stopping power diminishes as  $1/E$  as described by Bohr for the high velocity region. To extrapolate the theoretical treatment to the intermediate region where the ion is only partially stripped, a concept of effective charge has been formulated. As a consequence the effective charge also relates the energy loss of different ions.

Ions that traverse a crystal in a random or non-channeled direction will experience an average electron density of  $NZ_2$  in the crystal and have inelastic collisions with these electrons. Channeled ions follow a trajectory through the crystal, along a main crystalline direction and are deflected away from the atomic strings over small angles by Coulomb repulsion. As a result the interaction with electrons is predominantly with electrons in the channel and the channeled ions will be screened from inner shell electrons that surround the atoms. Thus these ions experience an average electron density smaller than  $NZ_2$ . Consequently the contribution of electronic stopping to the energy loss will be smaller in case of channeled ions. This has a direct effect on the projected range of ions as was observed by Davies and co-workers [1][2] who reported anomalously long ranges for heavy ions slowed down in polycrystalline aluminum and tungsten in 1960. In 1968, Dearnaley et al. [3] reported a broader and deeper implantation profile for 40 keV and 110 keV  $^{32}\text{P}$  ions in case the crystal was aligned along the  $\langle 110 \rangle$  axial direction and this confirmed the earlier observations in ion-implantation-profile studies. Moak et al. [4] observed

that ion channeling in a silicon-crystal based particle detector affects the detector pulse height and the energy resolution for high-energy (100 MeV) iodine and bromine ions. The difference in energy between the two peaks corresponds to the energy loss by nuclear collisions which is largely suppressed for the channeling case. This explains the higher amplitude of the charge pulse for the channeling case. Suppression of the channeling effect in particle detectors has been obtained in the fabrication process by cutting the crystalline semi-conducting material five degrees off-normal such that the crystalline orientation seems random, or at least not aligned with a main crystalline axis. The knowledge of the ranges and distribution profiles of keV ions in ion-implantation applications is inevitable to determine the charge carrier distributions and junction-depth of ion-implanted semi-conducting doped material. The values of these ranges and stopping powers are tabulated for random crystallographic orientation in Ziegler's handbook [5] or can be calculated using the computer program TRIM [6].

The application of theoretical models for the calculation of energy loss of swift ions is specifically interesting for the description of the anomalously-low energy loss of channeled ions. Although Dettmann [7] derived the energy loss of hyper-channeled ions, his approach was based on the impact-parameter formalism with a lattice comprised of independent atoms. The contribution of the valence electrons was treated separately using Lindhard's approximation for high-velocity ions (i.e.  $v_{ion} \gg v_{Fermi}$ ). Melvin and Tombrello [8] used separate contributions of the so called local electrons with characteristic high momentum transfer (close to the ion trajectory), valence electrons using Lindhard's model and core electrons. They compared experiments with calculations in a more phenomenological approach using a distribution of channeled particles according to the continuum approximation. In these calculations the valence electron density was assumed to be constant. Pathak and coworkers [9] derived energy loss along the axial  $\langle 110 \rangle$  direction by introducing explicitly a position-dependent electron density. Using Slater orbitals, the spherically symmetric core electron densities of each atom were averaged over the hexagonal shape of the channel, applying geometrical arguments. The valence electron density was again assumed to be constant.

Smulders and Boerma [10] and Dygo and Tuross [11] introduced (electronic) stopping in Monte-

Carlo trajectory calculations, developed to simulate high-energy backscattering experiments. Electronic stopping was introduced along the lines of Melvin and Tombrello with Dettmann's approach for the core electrons. Simulation of backscattering profiles showed a quite satisfactory agreement with experiments. Murthy and Srinivasan [12] implemented electronic energy loss in the binary-collision-cascade code MARLOWE and used the Fourier components of the Si electron-density distribution obtained from both calculated and measured X-ray structure factor data [13]. They calculated the energy loss of high-energy alpha particles in both channeled and random directions using the energy-loss model of Burenkov, Komarov and Kumakhov [14] that is valid for a non-uniform valence-electron density distribution.

Pioneering work on transmission ion channeling of MeV ions was done by Appleton in 1967 [15] who measured the energy distribution of 3-11 MeV protons through a 33  $\mu\text{m}$  silicon and a 45  $\mu\text{m}$  germanium crystal for both axial  $\langle 110 \rangle$  and  $\langle 111 \rangle$  and the planar (111), (110) and (100) crystal orientations. Eisen [16] measured the anomalously-low energy loss of 7 MeV channeled He ions through a 11.4  $\mu\text{m}$  silicon crystal for the  $\langle 111 \rangle$  and the  $\langle 110 \rangle$  direction. More recent transmission channeling has been published by Boshart and Seiberling [17][18]. They measured energy distributions of planar and axial channeled 625 keV  $\text{H}^+$  ions that were transmitted through thin-etched Si crystals. Experimental energy distributions were obtained in 'dark-field' transmission-channeling experiments, where transmitted ions scattered from a gold layer on the beam-exit side. The obtained energy distributions were interpreted with a modified Monte-Carlo code of Dygo which used the semiclassical approximation model for core electrons and the two-component free-electron-gas model for valence electrons. By adjusting the relative contributions of core and valence electrons to the H ion stopping, a good agreement with the experimental energy distribution was attained. Similar energy-loss distributions were measured using 2.5 MeV  $\text{He}^+$  ions [19], which have the same velocity as 625 keV  $\text{H}^+$  ions. In that work the MC fitting data of the 2.5 MeV experiment has been used to determine the surface location, bond length and vibrational amplitude of Sb surface atoms on Si(100)-2x1 [20].

Since depth perception and compositional analysis obtained from ion scattering experiments highly rely on stopping-power data, quantification of the stopping power along the channeling

directions and its effect on the energy distribution of the penetrated ions has been subject of study. A first principle Monte-Carlo trajectory calculation with incorporation of ion stopping of 4 MeV He<sup>+</sup> ions in silicon will be presented in section 7.3. In addition transmission-channeling experiments have been carried out to measure the energy-loss distribution of 4 MeV He<sup>+</sup> ions channeled, partially channeled and randomly oriented with respect to the crystalline <100> axis of a (100) silicon wafer. The details on sample preparation, the determination of the sample thickness and the experimental procedures will be presented in section 7.4. The energy spectra of the transmission measurements will be presented in section 7.5. Subsequently section 7.6 will show the orientation dependence of the energy-loss components of the channeled ions. Finally section 7.7 will discuss the results of the simulations and the measurements as well as conclusions.

## **7.2 Incorporation of energy loss in MC calculations**

In principle an energy distribution of channeled ions can be obtained from a modified version of the LAROSE MC trajectory calculations in which a model for the ion stopping is implemented. The original version of the program, however, uses a fraction of the random stopping power for all channeled ions. This is insufficient to obtain a detailed fit of the energy distribution of the transmitted ions. Basically, two significantly different stopping-power models can be distinguished. The impact-parameter dependent stopping and the free-electron gas approximation. The first model is successfully used for gases and isolated atoms or material where processes between ions and target atoms are independent of the surrounding target atoms. The framework for the impact-parameter dependent model was set by Bohr [21] who used the impulse approximation for the momentum transfer in a semiclassical treatment. The orbit of the ion was treated classically and the excitations of the electrons at large impact parameters were described by the excitation of a harmonic oscillator. Later, Bethe and Bloch [22] derived the mean energy loss quantummechanically using the impact-parameter formalism. For solid-state media the target atoms can not be treated as isolated atoms and the electrons are distributed throughout the medium due to formation of bonds. Therefore an electron density dependent stopping model is preferred over an impact-parameter dependent model. In addition a difference between the interaction of the ion with valence and core electrons is preferred. The best-

channeled ions will only interact with the valence electrons while the oscillating ions have close interaction with the core electrons. Lindhard's free electron gas model [23] describes the dynamic behaviour of the electron gas exclusively in terms of the electromagnetic properties of the system that can be justified by the idea that the behaviour of the particles is revealed only through the field to which they give rise. The motion of a particle is then no longer determined by the individual interactions with numerous other particles but only by the field. Lindhard noted that this free-electron-gas treatment was particularly useful for the loosely bound electrons in a solid.

The MC program LAROSE has been modified by applying the free-electron gas model in combination with the local-density approximation. The spatial charge-density distribution of the valence electrons in Si has been calculated with the computer code of Denteneer and van Haeringen [24]. The ground-state properties of silicon at  $T=0$  have been used and a spatial distribution of the valence charge density for the conventional unit cell was obtained. In essence their computer code gives the valence electron density for every point in the silicon unit cell. The local electron densities have been implemented in a stopping-power grid, that is closely related to the unit cell as defined in LAROSE. Matrix transformations were obtained for conversion of the stopping-power grid of each particular channeling direction to the conventional Si unit cell. The calculated electron density at the centre of each volume element in the stopping-power grid was taken as the local valence electron density of the corresponding volume element. In order to determine the influence of the interaction with core electrons on the shape of the energy-loss distributions, the spherically averaged core electron density calculated by Herman and Skillman [25] was added to the valence electron density of the band-structure calculations and the energy-loss distribution of the transmitted ions was calculated. The program is organized in such a way that incorporation of the core electron density in the stopping-power grid is treated as an option. Incorporation of the core electron density results in an increased electron density within a radius of 0.7 nm of the target atom positions.

To calculate the energy loss in a channeling direction we proceed as follows. At first the stopping power grid proportions are defined for the channeling direction involved. The valence electron densities are calculated at the centre of each volume element and stored in a one-dimensional

array. The size of the edge of the volume elements in the stopping-power-grid was approximately 0.03 nm. The ion energy loss per unit path length is correlated to the local electron density in the modeled silicon crystal in the local density approximation (LDA) by Lindhard's stopping power formula:

$$\frac{dE}{dx} = -\frac{1}{4\pi\epsilon_0^2 m_e} \left( \frac{Z_1 e^2}{v} \right)^2 \rho L(\rho, v) \quad 7.1$$

where  $m_e$  the electron mass,  $\rho$  the electron density,  $Z_1$  and  $v$  the atomic number and velocity of the ion. The stopping number  $L(\rho, v)$  was determined from a sixth-order polynomial fit of the digitized graphycal representation of  $L(\rho, v)$  at a constant velocity ( $v=1000$  keV/amu) as published by Jafra and Ziegler [26]. The validity of our calculations is therefore limited to ion energies of 4 MeV. The ion trajectories are calculated with the MC code for a given number of incident ions and the energy loss of each ion along the trajectories is obtained by multiplication of local path-lengths with local stopping powers. The sum of the local energy losses resulted in the electronic energy loss of the ion along the trajectory. Note that the calculated local stopping powers are always average values. The electronic energy loss is added to the energy loss originating from deflections along the channeling trajectories i.e. atomic interactions (nuclear energy loss).

### **7.3 Ion trajectory simulations**

Energy-loss spectra have been calculated for 5000 trajectories of 4 MeV He ions traversing through 1100 atomic layers in the  $\langle 111 \rangle$ ,  $\langle 110 \rangle$  and  $\langle 100 \rangle$  axial channeling directions in silicon. In all cases exact alignment with the crystal axes was used and angular beam divergence and energy spread of the incident beam were assumed to be absent. Figures 7.1 and 7.2 show the energy-loss distributions calculated with incorporation of valence electrons only, for Si  $\langle 110 \rangle$  and Si  $\langle 111 \rangle$  axial channeling directions. Note that for the  $\langle 110 \rangle$  and  $\langle 111 \rangle$  axial directions 1100 layers correspond to a thicknesses of 211.2 nm and 517.3 nm respectively.

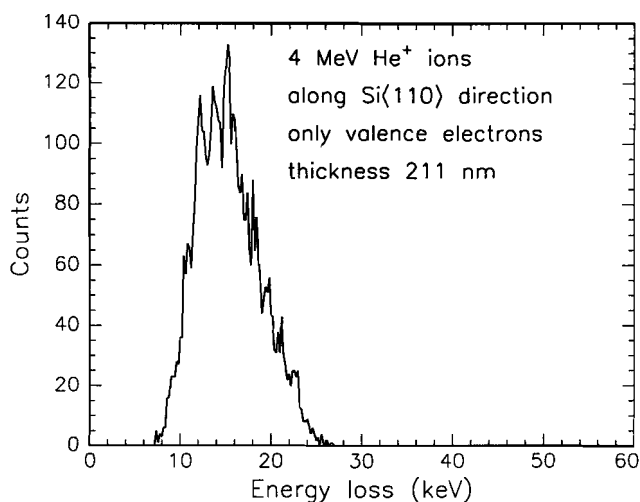


**Figure 7.1:** Energy-loss distribution calculated for 5000 trajectories of channeled  $\text{He}^+$  ions along the  $\langle 110 \rangle$  direction of a silicon crystal using the valence electron density. The initial energy was 4 MeV and 1100 atomic layers have been traversed corresponding to  $\sim 211$  nm. The accumulated counts correspond to energy intervals of 0.2 keV.

Table 7.1 lists the calculated average energy loss due to valence electrons only for the three axial directions and the corresponding channeled-to-random ratio's. Because of the symmetrical distribution the average energy loss is equivalent to the most probable energy-loss defined as the peak value in ref. [27]. The random stopping power was taken from Ziegler [28] to be 162 eV/nm for 4 MeV He ions. Note that the ions channeled in the  $\langle 110 \rangle$  direction have the smallest energy loss. The stopping power for ions in the  $\langle 100 \rangle$  direction is significantly larger than the stopping power for the  $\langle 110 \rangle$  and  $\langle 111 \rangle$  direction. Table 7.1 shows that the implementation of the valence-electron-density distribution in the calculations accounts for the trends in the experimentally observed stopping-power differences. Insertion of a constant valence electron density of 32 electrons per unit cell in formula 7.1 would result in a channeled-to-random ratio of 58% for all three directions. Comparing the differences between the measured and calculated channeled-to-random ratio's, we observe that the difference is significantly larger for the  $\langle 111 \rangle$  direction (11%) than for the  $\langle 110 \rangle$  direction (3%). Assuming that these differences are caused by the neglect of core electrons, it seems plausible that the discrepancy for the  $\langle 110 \rangle$  direction is smallest since from a geometrical point of view, core electrons have the smallest relative

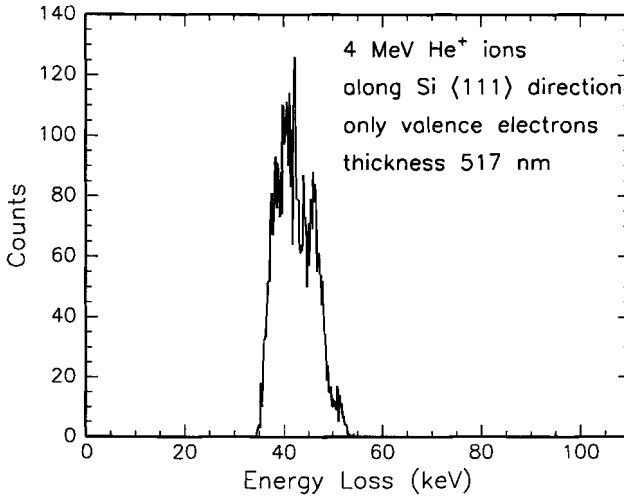


**Figure 7.2:** Energy-loss distribution calculated for 5000 trajectories of channeled  $\text{He}^+$  ions along the  $\langle 111 \rangle$  direction of a silicon crystal using the valence electron density. The initial energy was 4 MeV and 1100 atomic layers have been traversed corresponding to  $\sim 517$  nm. The accumulated counts correspond to energy intervals of 0.2 keV.

contribution to the average stopping power for that direction.

Axial direction	Calculated E-loss	Calculated Channeled/Random	Measured Channeled/Random
$\langle 110 \rangle$	73.1 eV/nm	46%	49%
$\langle 111 \rangle$	82.2 eV/nm	51%	62%
$\langle 100 \rangle$	93.7 eV/nm	58%	-

**Table 7.1:** Calculated average energy loss along the  $\langle 100 \rangle$ ,  $\langle 110 \rangle$  and  $\langle 111 \rangle$  axis in Si using only valence electron density. The measured channeled to random ratio's ( $\epsilon_m$ ) originate from Eisen et al. and correspond to the 'peak values' equivalent to the most-probable energy loss.

The calculated widths of the energy-loss distributions are caused by differences in energy loss for trajectories moving through different regions of the channels and probing different electron densities. The widths we observe in the calculated energy-loss spectra are of the order of the Bohr energy straggling. For instance the straggling as given by the Bohr formula for a He ion travelling 500 nm through silicon is 3.2 keV. If we assume a Gaussian distribution in the energy



loss this will lead to a FWHM in the energy-loss spectrum of 7.5 keV. It would be of interest, to unravel the contributions to the energy-loss distributions of energy straggling (i.e. statistical fluctuations in the actual ion-electron interaction) and energy-loss differences due to variations in electron density. In order to achieve this, a local stopping power distribution has to be defined for each volume element in the stopping power grid rather than only average stopping powers. If we assume these distributions to be Gaussian, we can specify a local straggling per unit length for each volume element. Although implementation of such a procedure introduces another sampling routine and consequently another drastic increase in the necessary computer time, the ever continuing increase in processing speed will bring this within the realm of possibilities soon.

It is important to note that path-length differences between various channeled trajectories do not contribute significantly to the calculated widths in figures 7.1 and 7.2. Relative path-length differences with respect to the total travelled distance are of the order of 0.1%. No correlation is found between the absolute path length and the magnitude of the stopping power which points to the possibility of probing specific area's of the channels keeping the overall path length constant.

In order to determine the influence of the interaction of ions with core electrons on the shape of the energy-loss distributions, the spherically averaged core electron density calculated by Herman and Skillman was added to the valence electron density of the band-structure calculations. This results in an increased electron density within a radius of 0.7 nm of the target atom positions. The spherically symmetric charge density of the core electrons is thus approximated in two surrounding layers of volume elements. The size of the edges of the volume elements in the  $\langle 110 \rangle$  stopping-power grid was  $0.33 \text{ \AA}$ . Figure 7.3 shows the result of a calculation for the axial  $\langle 110 \rangle$  direction without changing the stopping model.

The spectrum shows an asymmetric energy-loss distribution with a high-energy-loss tail which is in qualitative agreement with experimental results of Eisen and Cholewa [29]. The tail is caused by the ions which traverse oscillating trajectories in the channels thus probing the regions with high electron densities near the lattice rows. Although the average energy loss increases

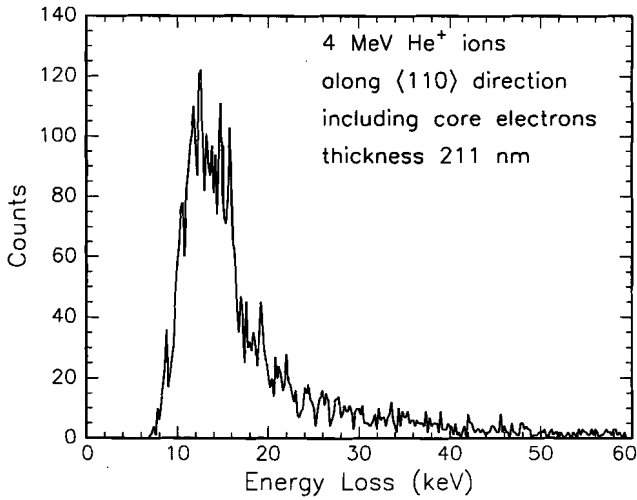


**Figure 7.3:** Energy-loss distribution calculated for 5000 trajectories of channeled He<sup>+</sup> ions along the <110> direction of a silicon crystal with incorporation of the core electron density. The initial energy was 4 MeV and 1100 atomic layers have been traversed corresponding to ~211 nm. The accumulated counts correspond to energy intervals of 0.2 keV.

after addition of the core electron density, the most probable energy loss has not changed significantly. This is in disagreement with our expectation that the incorporation of the core electrons would increase the channeled-to-random ratio to the experimentally observed peak values as listed in the table. This behaviour is most probably due to the limited applicability of the Lindhard free electron gas model for strongly bound electrons. In general, also the question can be raised to what extent Lindhard's formula can be combined with the local density approximation in these calculations. The stopping number  $L$  contains contributions of close collisions and distant collisions and the latter obviously probes the electron density over impact parameters larger than the size of a stopping-power volume element. It might be interesting to evaluate both terms separately where only the close collisions relate to the local electron density. Alternatively, the contribution of the core electrons to the stopping power can be calculated with a second stopping model (e.g. the impact-parameter dependent model of Sigmund [30]). So far addition of core electron densities resulted in a high-energy-loss tail which is in qualitative agreement with experimental data reported in literature.

In order to compare the calculated energy-loss distribution of channeled ions with experiment transmission channeling has been applied on a 5  $\mu\text{m}$  thick (100) oriented Si crystal using a 4 MeV incident  $\text{He}^+$  ion beam. Only qualitative comparison is possible since calculation of the energy loss through 5  $\mu\text{m}$  thick silicon requires excessive computation times. Section 7.5 will present an energy-loss data set measured with the channeling setup. This data set obtained for a Si crystal of 5  $\mu\text{m}$  can be used as a reference for future transmission simulations.

#### 7.4 Target preparation and experimental details

The analyzed Si samples used for transmission-channeling experiments were commercially available thin-etched self-supporting 2 inch wafers obtained from Virginia Semiconductors. The wafer thickness was specified at  $2\pm 2$   $\mu\text{m}$  and its orientation is with the  $\langle 100 \rangle$  axis near the surface normal. The fragile wafer has been cut in  $1\text{cm}^2$  square pieces which were mounted on a target holder using melted Indium as glue. For routine transmission measurements and guaranteed flat-sample preparation we would recommend to consider the use of wafers with thin-etched regions. A chemical etching preparation technique is described in detail by Wampler [31] or Cheung [32] and Ishizaka [33].

The results obtained in the transmission-channeling experiment were carried out using two scattering geometries: a 'dark field' and a 'bright field' geometry. The thickness of the Si foil and the aligned position of the crystal with the ion beam are determined with the detector at a  $45^\circ$  forward angle (dark field). The transmission geometry ( $\Theta=0^\circ$ ) is used to measure the energy distribution of the transmitted ions (bright field). The experiments have been carried out using 4 MeV  $\text{He}^+$  ions from the AVF cyclotron. The angular divergence of the  $\text{He}^+$  beam has been limited by collimator slits and was better than  $0.04^\circ$ . The scattered ions were detected by the 50  $\text{mm}^2$  PIPS backscattering detector at a distance of 120 mm from the target, mounted on a movable detector disk. The overall resolution of the detection system was better than 25 keV. The detector mount on the disk allows to position the detector at a scattering angle between 5 degrees forward, through zero degrees (transmission) and towards 153 degrees backward. The target orientation for parallel alignment of the beam with the main crystalline  $\langle 100 \rangle$  axis was found with the detector positioned at a  $45^\circ$  forward scattering angle using a beam current of 4

nA. The local (100)Si target thickness is derived from the random energy spectrum acquired for this orientation.

The energy-loss distribution of ions through the  $\langle 100 \rangle$  crystalline direction of silicon has been measured in a channeling transmission experiment. To limit the count rate in the transmission detector, the beam current was limited to sufficiently low counting rates in the detector ( $< 10000$  cps) by means of both the collimator slits and the energy-dispersive slits of the beam-guiding system. The spot size was reduced to  $0.6 \times 0.7 \text{ mm}^2$  and the sample was oriented at the position where its  $\langle 100 \rangle$  crystalline direction coincided with the incident beam. In succession the detector position was optimized for the maximum number of detected incident ions. This transmission location was determined using a detector scan in the angular region between  $-5^\circ$  to  $+5^\circ$ .

After proper detector alignment the  $\langle 100 \rangle$  aligned and random energy spectrum were measured. The sample was rotated  $1.5$  degree away from the  $\langle 100 \rangle$  surface normal and tilted an additional  $3$  degrees to obtain the energy distribution for a non-aligned (random) orientation. The angular displacement is sufficient to reduce either planar or axial channeling since the characteristic angle for channeling is significantly smaller ( $\Psi_{\langle 100 \rangle} = 0.35^\circ$ ). Subsequently, the sample was aligned in a way that the (110) plane of the crystal coincided with the horizontal plane and an angular scan in the (110) plane through the  $\langle 100 \rangle$  axis was measured using the goniometer rotation axis. An additional scan through the (110) plane has been measured using the goniometer tilt direction. Energy spectra for different sample orientations have been obtained for  $60$  seconds to allow sufficient statistics. Normalisation of the spectra is carried out with respect to the number of detected ions. This method for normalisation is necessary since the number of ions detected in the rotating-vane detector is negligible due to the small ion dose.

## **7.5 Results**

Figure 7.4 depicts the measured random (normal) and  $\langle 100 \rangle$  channeled energy spectrum obtained at a  $45^\circ$  forward angle. The scattering geometry is shown in the inset and sample front (F) and back (B) are indicated in the figure. Notice that the channeled spectrum shows a tail towards higher ion-energy. This implies a smaller energy loss and thus a reduced stopping power

for channeled ions that have been scattered from the sample back-surface. Ions scattered from the sample front observed a random stopping alike the ions that scattered from the sample surface before  $\langle 100 \rangle$  alignment took place. The sample thickness is derived from the obtained random spectrum and yields  $5.5 \pm 0.2 \mu\text{m}$ , which is significantly higher than the specified thickness ( $2 \pm 2 \mu\text{m}$ ). The detector was moved to the transmission geometry ( $\Theta=0^\circ$ ) and many energy spectra were measured for different crystallographic orientations.

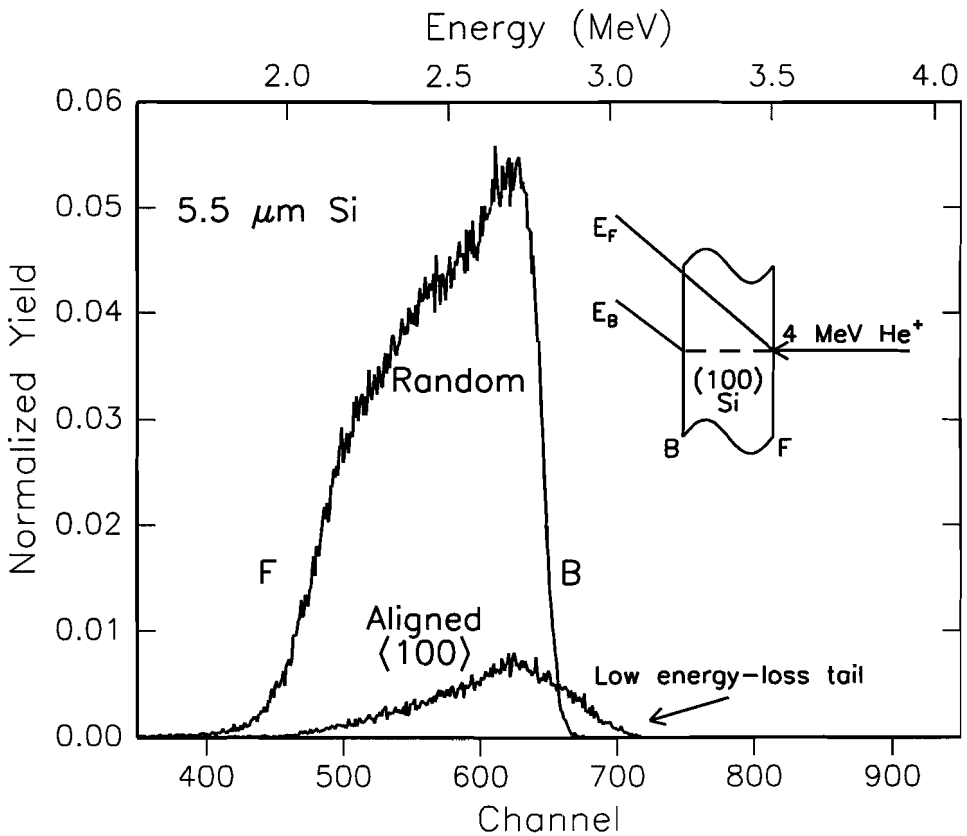


**Figure 7.4:** The measured random (normal) and  $\langle 100 \rangle$  aligned energy spectrum obtained from a self-supporting thin (100) Si sample. The sample front (F) and back (B) are indicated in the figure. Notice that the  $\langle 100 \rangle$  channeled spectrum shows a tail towards higher energy, due to smaller energy loss. The sample thickness is derived from the random spectrum and yields  $5.5 \pm 0.2 \mu\text{m}$ .

Figure 7.5 depicts the energy spectra measured in transmission at random incidence on the (100)Si sample, the  $\langle 100 \rangle$  axial-channeled spectrum, the (110) planar-channeled spectrum and the peak corresponding to the incident beam. The planar spectrum is acquired 2.0 degrees away from the  $\langle 100 \rangle$ -aligned target position. Energy spectra are scaled to enable detailed comparison of the most-probable energy loss. Scaling factors are indicated for each spectrum. The observed differences in the energy-loss distributions for the different target orientations is striking. The width of the energy distribution of the  $\langle 100 \rangle$  channeled ions (FWHM=160 keV) is far larger

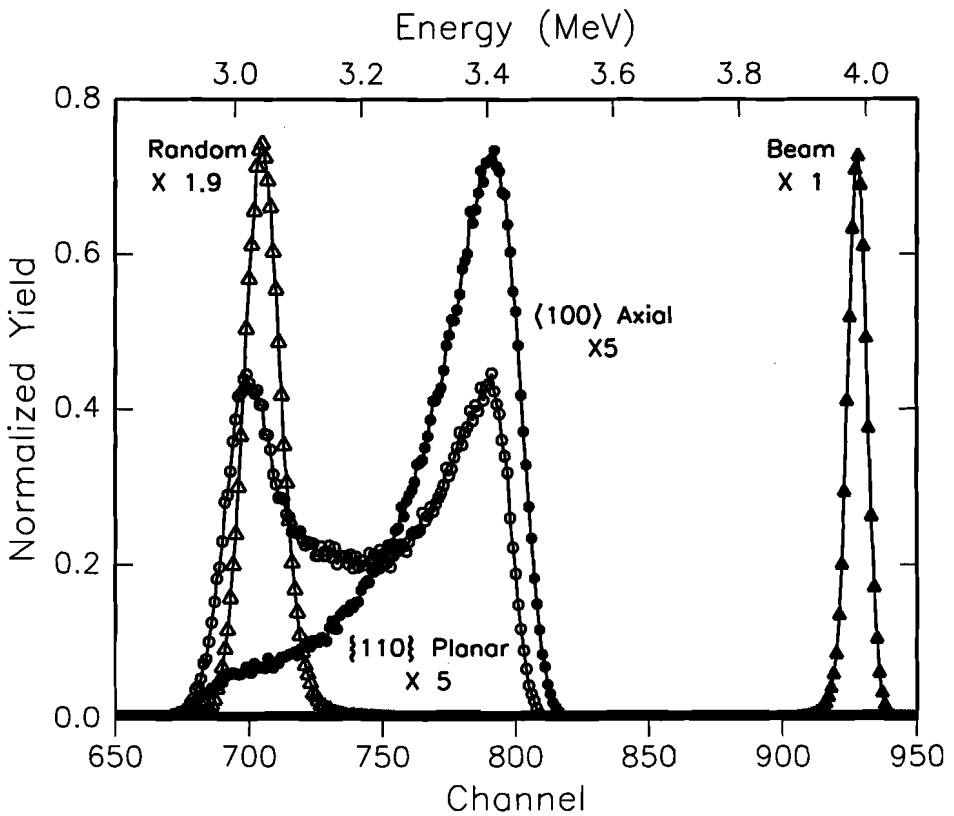


**Figure 7.5:** Transmission energy spectra at random incidence on the (100)Si sample, the  $\langle 100 \rangle$  axial channeled spectrum, the (110) planar channeled spectrum and the energy distribution of the incident beam are depicted in the figure. The planar spectrum is acquired 2.0 degrees away from the  $\langle 100 \rangle$  aligned target position. The spectra are scaled to enable detailed comparison of the most-probable energy loss. Corresponding scaling factors are indicated. Variation of the ion energy loss with target orientations is significant as is the width of the energy distributions.

than the width of the randomly transmitted ions (FWHM=75 keV) and the distribution of the axially channeled ions is highly asymmetric. This is in qualitative agreement with the MC calculations where we incorporated the core electrons and the simulated energy spectrum showed the high-energy loss tail. Thus the observed width is most probably due to the difference in electron density as observed by the highly oscillating trajectories. The ratio  $\epsilon_m$  between (most probable) channeled and random stopping power has been determined for the peak position of the measured  $\langle 100 \rangle$  channeled and random energy distributions with respect to the spectrum of the incident beam and yields:  $\epsilon_m = 0.61$ . This value is significantly larger than  $\epsilon_m$  for the  $\langle 110 \rangle$  direction but of the order of  $\epsilon_m$  of the  $\langle 111 \rangle$  direction, according to table 7.1. The energy distribution in the spectrum of the (110) planar channeled ions shows the contribution of best channeled ions, with small energy-loss, and ions with higher energy-loss which is ascribed to those ions that are deflected from plane to plane that also observed the core-electron density in the vicinity of the planes. Notice that the large-energy-loss part of the aligned spectrum has a more-than-random-energy-loss component, implying a more than average electron density along its trajectory through the crystal.

## 7.6 Angular dependence of energy-loss components

The energy distributions of transmitted ions have been obtained as a function of the angle between the incoming beam and the  $\langle 100 \rangle$  target orientation. This “angular scan” has been carried out in the (110) plane through the  $\langle 100 \rangle$  axis. Energy intervals in the obtained spectra are selected and the fraction of counts in these intervals are plotted as a function of the sample position in figure 7.6. The best-channeled ions lose less energy and leave the sample with a higher energy. Selection of this energy interval will result in an angular scan with a maximum number of ions for the aligned position while this contribution vanishes for randomly penetrated ions. In the obtained transmission spectra 5 different typical energy intervals can be distinguished; the high energy-loss component [670:700] and the low energy-loss component [790:820]. The middle energy-loss component is selected from interval [730:760]. The interval [670:730] is defined as the random loss fraction and interval [760:820] is defined as the channeled loss fraction. Finally this results in 5 typical energy intervals each resulting in a different angular scan. Figure 7.6 depicts the angular dependence of the fraction of the acquired

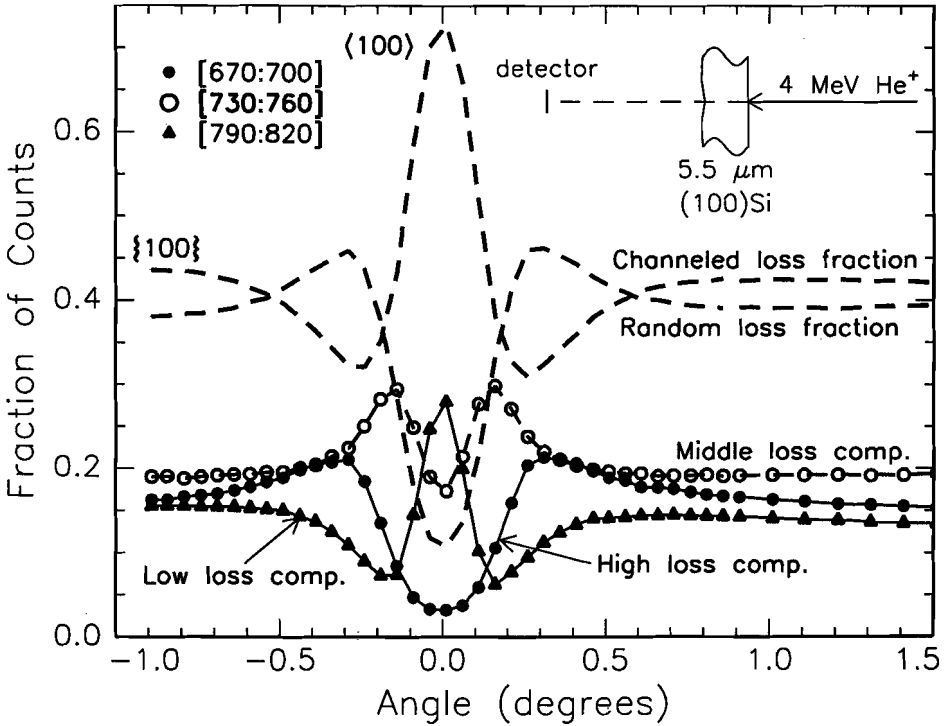


**Figure 7.6:** The angular dependence of the fraction of the acquired counts in typical energy intervals from the transmission spectra for 4 MeV He<sup>+</sup> ions through a 5.5 μm Si crystal. The angular scan has been obtained relative to the <100> axial direction in the (110) plane. Five different typical energy intervals can be distinguished the high energy-loss component [670:700] and the low energy-loss components [790:820]. The middle e-loss component is selected from interval [730:760]: The interval [670:730] is defined as the random loss fraction and interval [760:820] is defined as the channeled loss fraction.

counts in the depicted intervals. The fraction of detected counts in the channeled energy-loss and low energy-loss components are dominant for perfect <100> alignment while the random-loss and the high-loss components contribute minimal. The random loss fraction is very much reduced when the <100> crystalline axis is aligned with respect to the incident ion beam. The sum of three contributions: the channeled energy-loss, random energy-loss and the middle energy-loss components is unity for all angles.

A similar angular scan across the (110) plane has been measured to obtain the energy distribution for planar channeling. The energy distribution of the transmitted ions changes from



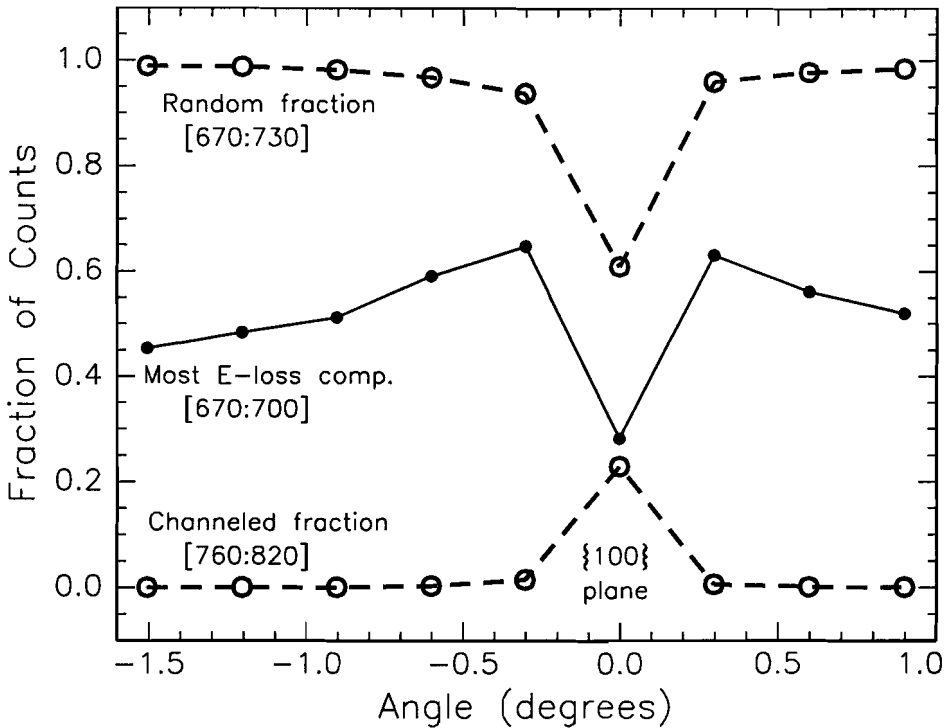


**Figure 7.7:** A transmission angular scan measured through the (110) plane. Three energy intervals were distinguished in the energy spectra. The random fraction is obtained from the fraction of counts in energy interval [670:730] (fig 7.5). The most-energy-loss component is sorted from interval [670:700]. An increase of this component has been observed for nearly planar channeling. The channeled fraction of the energy loss is obtained from interval [760:820] and is only present for the aligned (110) planar spectrum.

a planar distribution, with two distinctive peaks, to a random energy loss distribution where no low-energy-loss component is observed. Figure 7.7 depicts the obtained scan of three energy intervals. The random fraction is obtained from the fraction of counts in energy interval [670:730]. The most energy-loss component is sorted from interval [670:700]. The channeled fraction is obtained from interval [760:820]. Note that the random contribution reaches unity for a ‘random’ sample orientation. The fraction of ions with most energy loss is significantly increased at the shoulders of the scan while the channeled energy-loss contribution only shows up for the aligned (110) planar spectrum. Smaller steps in the region near in-plane alignment should be carried out when a more detailed shape of the individual contributions is required.

## **7.7 Discussion and conclusions**

With the introduction of the spatial valence-electron-density distribution in Monte-Carlo trajectory calculations we are able to reproduce average stopping-power differences in the axial  $\langle 111 \rangle$ ,  $\langle 110 \rangle$  and  $\langle 100 \rangle$  directions for sample thicknesses of several hundreds of nanometers. However, a quantitative comparison of the average energy loss as well as the detailed profile of the energy-loss distribution with experiments can only be expected once the contribution of core electrons to the stopping power has been included properly in the calculations. The natural separation of valence and core electrons introduced by the bandstructure calculations allows a simple addition of the two electron densities. The shape of the energy-loss distribution without core electrons is caused by spatially varying electron densities along different ion trajectories, it is nearly symmetrical and has a width slightly larger than expected from Bohr straggling. The occurrence of the high-energy-loss tail, observed in the simulations that incorporated the core electron densities, confirms that the ions that have close encounters with the atomic strings, but remain channeled, experience a higher energy loss.

The transmission experiments are a detailed energy-loss study on  $\langle 100 \rangle$  channeled ions in a  $(100)$  oriented  $5 \mu\text{m}$  thick silicon crystal. The high-energy-loss tail observed for the  $\langle 100 \rangle$  axially channeled ions confirmed the existence of a high-energy-loss component as was qualitatively predicted by the MC simulations which incorporated the core electron density. This contribution is likely due to the ions with relatively large transverse kinetic energy that just remain channeled but probe the core electron density in the vicinity of the atomic strings. The energy distribution of the transmitted ions has been measured as a function of the target orientation to obtain angular scans of typical energy-loss intervals that show the relative contribution to the energy-loss distribution. The scans are in qualitative agreement with data presented by Appleton and co-workers who studied the energy loss of 3-11 MeV channeled protons. The use of the terminology *most probable* or *average* energy loss is very critical and should not be used for planar channeled ions since these ions have an energy distribution which can not be characterized by one single value for the specific energy loss or stopping power. The measured distributions show that these spectra can be interpreted by distinguishing two different paths through the crystal. A fraction of the incident ions will traverse close to the centre of the

channel and only experience small energy-loss while another fraction has close encounters with the planes and loses more energy due to close interaction with the core electrons in the vicinity of the planes. Fortunately use of MC calculations can provide detailed energy distributions of channeled ions and this can assist in correct interpretation of the measured data. However, since computational times are still relatively long the use of thinner crystals and faster computers will be of great help in future experiments and calculations.

## References

1. J.A. Davies, J. Friesen and J.D. McIntyre, *Can. J. Chem.* 38 (1960) 1526.
2. J.A. Davies, J.D. McIntyre, R.L. Cushing and M. Lounsbury, *Can. J. Chem.* 38 (1960) 1535.
3. G. Dearnaley, J.H. Freeman, G.A. Ward and M.A. Wilkins, *Can. J. Phys.* 46 (1968) 587.
4. C.D. Moak, J.W.T. Dabbs and W.W. Walker, *Bull. Am. Phys. Soc.* 11 (1966) 101.
5. J.F. Ziegler, *Handbook of Stopping Cross-sections for Energetic Ions in all Elements*, Pergamon Press, New York. (1980) and J.F. Ziegler, J.P. Biersack and U. Littmark, *The Stopping and Range of Ions in Solids*, Pergamon Press, New York (1985).
6. J.P. Biersack and J.F. Ziegler, TRIM computer program, IBM, Yorktown Heights, New York. (1991)
7. K. Dettmann and M.T. Robinson, *Phys.Rev. B* 10 (1974) 1.
8. J.D. Melvin and T.A. Tombrello, *Radiat. Eff.* 26 (1975) 113.
9. R. Agnihotri and A.P. Pathak, *Nucl. Instr. and Meth. B* 67 (1992) 39.
10. P.J.M. Smulders and D.O. Boerma, *Nucl. Instr and Meth. B* 29 (1987) 471.
11. A. Dygo and A. Turos, *Phys. Rev. B* 40 (1989) 7704, and A. Dygo and A. Turos, *Phys. Lett. A* 127 (1988) 281.
12. C.S. Murthy and G.R. Srinivasan, *Phys. Rev. B* 47 (1993) 1256.
13. C.M. Bertoni, V. Bortolani, C. Calandra and F. Nizzoli, *J. Phys. C* 6 (1973) 3612.
14. A.F. Burenkov, F.F. Komarov and M.A. Kumakhov, *Sov. Phys. JETP* 51 (1980) 4.
15. B.R. Appleton, C. Erginsoy and W.M. Gibson, *Phys. Rev.* 161 (1967) 330.
16. F.H. Eisen, G.J. Clark, J. Böttiger, J.M. Poate, *Rad. Eff.* 13 (1972) 93.

*Stopping power of channeled He ions*

17. A. Dygo, M.A. Boshart, M.W. Grant and L.E. Seiberling, Nucl. Instr. and Meth. B 93 (1994) 117.
18. A. Dygo, M.A. Boshart, L.E. Seiberling and N.M. Kabachnik, Phys. Rev. A50 (1994) 4979.
19. M.A. Boshart, A. Dygo and L.E. Seiberling, Phys. Rev. A 51 (1995) 2637.
20. M.A. Boshart, A.A. Bailes III, A. Dygo and L.E. Seiberling, J. Vac. Sci. Technol. A 13 (1995) 2764
21. N. Bohr, Phil. Mag. 20 (1913) 10.
22. F. Bloch, Ann. Physik 16 (1933) 285; and H. Bethe, Ann. Physik 5 (1930) 325.
23. J. Lindhard, Kgl. Danske. Videnskab. Selskab., Mat. Fys. Medd. 28 (1954) 1.
24. P.J.H. Denteneer and W. van Haeringen, J. Phys. C 18 (1985) 4127.
25. F. Herman and S. Skillman, *Atomic Structure Calculations*, Prentice-Hall, 1963.
26. G.J. Iafrate and J.F. Ziegler, J. of Appl. Phys. 50 (1979) 5579.
27. F.H. Eisen, G.J.Clark, J. Bottiger, J.M. Poate, Radiat. Eff. 13 (1972) 93.
28. J.F. Ziegler, *Helium Stopping Powers and Ranges in all Elements*, Pergamon press, New York, 1977.
29. M. Cholewa, G. Bench, A. Saint, G.J.F. Legge and L. Wielunski, Nucl. Instr. and Meth. B 56/57 (1991) 795.
30. E.H. Morentsen, H.H. Mikkelsen and P. Sigmund, Nucl. Instr. and Meth. B 61 (1991) 139.
31. W.R. Wampler, Phys. Rev. B 51 (1995) 4998.
32. N.W. Cheung, Rev. Sci. Instrum. 51 , (1980) 1212.
33. A. Ishizaka and Y. Shiraki, J. Electrochem. Soc. 133 (1986) 666.

## Publications

P.W.L. van Dijk, L.J. van IJzendoorn and M.J.A. de Voigt.- *Strained-layer analysis with high-energy ion channeling* - Nucl. Instr. and Meth. in Physics Research B 118 (1996) 97-102, Poster presentation IBA 12 conference, Tempe, Arizona, USA, May 22-26, 1995.

L.J. van IJzendoorn, J.W. Niemantsverdriet, R.J. Severens, P.W.L. van Dijk, M.J.A. de Voigt.- *Applications of cyclotron based ion scattering* - Nucl. Instr. and Meth. in Physics Research B 89 (1994) 114-121.

P.W.L. van Dijk, L.J. van IJzendoorn and M.J.A. de Voigt.- *High-energy ion channeling* - Poster presentation NATO ASI Summerschool Thessaloniki, Greece. "Application of particle and laser beams in materials technology", May 8-21, 1994.

P.W.L. van Dijk, L.J. van IJzendoorn, M.de Koning, P.Bobbert, W. van Haeringen, M.J.A. de Voigt.- *Stopping powers for channeled helium ions in silicon using electron densities from bandstructure calculations* - Nuclear Instr. and meth. in Physics Research B 85 (1994) 551-555. Oral presentation IBA 11 conference, Balatonfured, Hungary, Juli 5-9,1993

P.W.L. van Dijk, L.J. van IJzendoorn, P.Brinkgreve, M. Janszen and M.J.A. de Voigt - *Channeling with high-energy particles using a 3-30 MeV cyclotron* - Poster presentation IBA 11 conference, Balatonfued, Hungary, Juli 5-9, 1993

P.W.L. van Dijk.- *Diepteprofilering van lichte elementen met CERDA-TOF* - NEVAC BLAD 30-3, 1992.

## Summary

The ion-channeling effect, as discovered in the early 1960's, has been used for materials analysis in the last decades and now serves as a tool for the quantification of crystal damage and lattice deformation of epitaxially grown strained layers. Other commonly used applications of the channeling effect in materials characterisation are the studies of ion-implantation profiles and the quantification of implantation induced disorder. Although ion channeling also occurs at relatively high energies (3-30 MeV) the applications of high-energy ion channeling in materials analysis are scarce. A reason for this might be a shortage of accelerators, able to accelerate the ions towards velocities of several MeV/amu. This thesis demonstrates the applicability of high-energy ion channeling for materials characterisation and elemental analysis for a variety of materials. The AVF cyclotron serves as an ion source and produces the low  $Z_2$  ions with relatively high energy. Careful beam handling provides a well-collimated beam of particles and enables ion channeling with sufficient beam current.

Chapter 1 is a general introduction to ion channeling and reviews the discovery of channeling, the early history of the technique and some applications in materials science. The main advantage of the use of high-energy ions in channeling experiments is the decrease of the critical angle for channeling;  $\Psi_c \sim E^{-1/2}$ . Consequently, the sample orientation with respect to the incident ion beam becomes more critical and the channeling experiments with high-energy ions require a goniometer with superior angular accuracy. Such a goniometer has been designed and built by the central technical workshop of the university and has become the heart of the channeling setup. In chapter 2 a detailed description of the high-energy-ion-channeling facility is presented. The vacuum requirements of the UHV setup are evaluated and calibration experiments necessary to characterise the goniometer are presented. In chapter 3 the first results with the new setup are presented, proving the feasibility of ion channeling with ions obtained from a cyclotron. Silicon  $\langle 100 \rangle$  angular scans have been measured in an RBS experiment using 4 MeV, 12.6 MeV and 25 MeV He ions.

In chapter 4 strain analysis of  $\text{Si}_{1-x}\text{Ge}_x$  single-layer heterostructures, with typical Ge fractions between 0.05 and 0.25, has been demonstrated. The tetragonal distortion of the strained layers is determined from the shift of a non-normal principal crystal axis of the strained layer with respect to the position of the corresponding principal crystal axis of the substrate. Strain

measurements obtained with 4 MeV and 12.6 MeV He ions are compared. These measurements show that the use of high-energy ions provides an increased angular resolution in lattice deformation studies and the determination of the strain in the epitaxially grown layer can be carried out extremely accurately when 12.6 MeV He<sup>++</sup> ions are used. To broaden the application of high-energy ion channeling to a variety of targets, strain measurements of Si<sub>1-x-y</sub>Ge<sub>x</sub>C<sub>y</sub> and In<sub>x</sub>Ga<sub>1-x</sub>As heterostructures have been presented in chapter 5. Furthermore, depth profiling of disorder in a Si<sub>1-x</sub>Ge<sub>x</sub> relaxed multi-layered structure has been demonstrated using 6 MeV He ions. The use of these high-energy He ions allows profiling of larger depth ranges in defect depth studies on Si<sub>1-x</sub>Ge<sub>x</sub> based structures.

In chapter 6 a detailed study has been presented on the use of NRA- and RBS-channeling for the determination of the vibrational amplitude of In and P atoms in a diatomic InP crystal. The phosphorus signal was obtained from detected protons, created by the exothermal <sup>31</sup>P( $\alpha$ ,p)<sup>34</sup>S nuclear reaction while the yield of elastically scattered alpha particles from the indium target atoms served as a probe for those atoms. Vibrational amplitudes of the individual In and P atoms have been obtained from a combination of <110> and <111> angular-scan measurements and Monte-Carlo trajectory calculations.

Finally, in chapter 7 the energy loss of 4 MeV He ions in a silicon crystal at channeling conditions is studied. The incident beam is transmitted through the thin crystal and ions only lose part of their energy. For the transmitted particles the energy distribution is strongly dependent on the crystallographic orientation with respect to the incident ion beam. The energy loss of the 4 MeV He ions has been subject of study in both Monte-Carlo simulations and transmission experiments. With the introduction of the spatial valence-electron-density distribution in Monte-Carlo trajectory calculations we are able to obtain average stopping-power differences in the axial <111>, <110> and <100> directions for sample thicknesses of several hundreds of nanometres. Transmission-channeling experiments have been carried out to measure energy distributions of transmitted ions for many different orientations resulting in angular scans which reveal the orientation dependence of the ion stopping. Energy-loss distributions for planar channeled, axial channeled and non-channeled ions are identified and qualitatively compared with the simulations.

## Samenvatting

Het ionen channeling effect, zoals dat ontdekt is in het begin van de zestiger jaren, is gebruikt voor materiaalanalyse in de afgelopen decennia en kan gebruikt worden voor de kwantificatie van kristalschade en de roostervervorming van epitaxiaal gegroeide gestraalde lagen. Andere veel gebruikte toepassingen van het channeling effect in materiaal onderzoek zijn de studies van ionen-implantatie-profielen en de kwantificatie van de door de implantatie geïnduceerde defecten. Hoewel ionen channeling ook optreedt bij relatief hoge energieën (3-30 MeV) zijn toepassingen van channeling met hoog energetische ionen relatief schaars. Een reden hiervoor zou een tekort aan versnellers, die de ionen tot snelheden van enkele MeV/amu kunnen versnellen, kunnen zijn. Dit proefschrift toont enkele mogelijkheden voor de toepasbaarheid van channeling met hoog energetische ionen voor materiaalkarakterisatie en elementaire analyse voor verschillende materialen. Het AVF cyclotron dient hierbij als ionenbron en produceert de ionen met lage  $Z_2$  en relatief hoge energie. Een goede controleerbaarheid van de bundel maakt het mogelijk om een goed gecollimeerde bundel van deeltjes te verkrijgen en maakt zo uitvoer van ionen channeling mogelijk met voldoende bundelstroom.

Hoofdstuk 1 is een algemene inleiding over ionen channeling en blikt terug op de ontdekking van channeling, de prille historie van de techniek en enkele toepassingen in materiaalonderzoek. Het grootste voordeel van het gebruik van hoog energetische ionen in channeling experimenten is de verkleining van de kritische hoek voor channeling;  $\Psi_c \sim E^{-1/2}$ . Dientengevolge wordt de uitlijning van het preparaat ten opzichte van de inkomende ionenbundel kritischer en vereisen de channeling experimenten met hoog energetische ionen een goniometer met superieure hoeknauwkeurigheid. Zo'n goniometer is ontworpen en vervaardigd in de centrale technische werkplaats van de universiteit en dit is het hart van de channeling opstelling geworden. In hoofdstuk 2 is een gedetailleerde beschrijving van de hoge-energie-channeling-opstelling getoond. De vacuumvereisten met betrekking tot de UHV opstelling zijn geëvalueerd en calibratie-experimenten, noodzakelijk voor de karakterisatie van de goniometer, zijn beschreven. In hoofdstuk 3 zijn de eerste resultaten, verkregen met de opstelling, gepresenteerd waarmee de toepasbaarheid van channeling met gebruik van ionen, die versneld zijn door een cyclotron, is bewezen. De hoekafhankelijke opbrengst metingen, uitgevoerd aan een silicium  $\langle 100 \rangle$  kristal, zijn verkregen in een RBS experiment waarbij gebruik is gemaakt van 4 MeV, 12.6 MeV en 25



MeV He ionen.

In hoofdstuk 4 zijn roostervormingsanalyses van  $\text{Si}_{1-x}\text{Ge}_x$  enkellaags heterostructuren met typische Ge fracties tussen 0.05 en 0.25 getoond. De tetragonale vervorming van de *gestrainte* lagen is bepaald aan de hand van de verschuiving van een niet-normale hoofdkristal van de gestrainte laag ten opzichte van de positie van de corresponderende hoofdkristal van het substraat. Strainmetingen uitgevoerd met 4 MeV en 12.6 MeV ionen zijn met elkaar vergeleken. Deze metingen tonen aan dat met het gebruik van hoog energetische ionen een verhoogde hoeknauwkeurigheid in studies aan roostervorming bereikt kan worden en dat de bepaling van de strain in de epitaxiaal gegroeide laag extreem nauwkeurig kan worden uitgevoerd als gebruik wordt gemaakt van 12.6 MeV  $\text{He}^{++}$  ionen. Om het toepassingsgebied voor channeling met hoog energetische ionen te verbreden naar een variëteit aan preparaten zijn strain metingen uitgevoerd aan  $\text{Si}_{1-x-y}\text{Ge}_x\text{C}_y$  en  $\text{In}_x\text{Ga}_{1-x}\text{As}$  heterostructuren, welke zijn gepresenteerd in hoofdstuk 5. Eveneens is de diepteprofilering van roosterfouten in een  $\text{Si}_{1-x}\text{Ge}_x$  gerelaxeerde multilaag gedemonstreerd, waarbij gebruik werd gemaakt van 6 MeV He ionen. Het gebruik van deze hoog-energetische helium ionen maakt de profilering van defecten in  $\text{Si}_{1-x}\text{Ge}_x$  gebaseerde structuren tot op grotere diepte mogelijk.

In hoofdstuk 6 is een gedetailleerde beschrijving gegeven voor het gebruik van NRA- en RBS-channeling voor de bepaling van de vibratie-amplitudes van In en P atomen in een diatomig InP kristal. Het fosfor signaal is verkregen van gedetecteerde protonen die ontstaan zijn bij de exotherme  $^{31}\text{P}(\alpha, p)^{34}\text{S}$  nucleaire reactie terwijl de opbrengst van elastisch aan indium verstrooide alfa deeltjes dient als een signaal voor deze In atomen. De Vibratie-amplitudes van de individuele In en P atomen zijn verkregen uit een combinatie van  $\langle 110 \rangle$  en  $\langle 111 \rangle$  hoekverstrooiings-experimenten en Monte-Carlo baanberekeningen.

Tot slot is in hoofdstuk 7 het energieverlies van 4 MeV He ionen in een silicium kristal onder channeling condities bestudeerd. De inkomende bundel wordt doorgelaten door het dunne kristal en de ionen verliezen slechts een deel van hun energie. Voor deze doorgelaten ionen is de energieverdeling sterk afhankelijk van de kristalorientatie ten opzichte van de inkomende ionenbundel. Het energieverlies van de 4 MeV He ionen is bestudeerd in zowel Monte-Carlo simulaties alsook in transmissie-experimenten. Met de introductie van de plaatsafhankelijke valentie-elektronendichtheidverdeling in Monte-Carlo baanberekeningen zijn we in staat om de verschillen in het gemiddelde energieverlies in de axiale  $\langle 111 \rangle$ ,  $\langle 110 \rangle$  en  $\langle 100 \rangle$  richtingen te

verkrijgen voor substraatdiktes van enkele honderden nanometers. Transmissie channeling experimenten zijn uitgevoerd om de energieverdeling van doorgelaten ionen voor verschillende orientaties te meten hetgeen geresulteerd heeft in hoekafhankelijke-opbrengst-metingen welke de orientatie-afhankelijkheid van de afremming van de ionen weergeven. Verdelingen van het energieverlies voor planair gechannelde, axiaal gechannelde en niet-gechannelde ionen zijn geïdentificeerd en kwalitatief vergeleken met de waarden verkregen uit de simulaties.

## Dankwoord

Na ruim vier jaar zwoegen zit het er dan op. Het proefschrift dat hier voor je ligt is echt niet het werk van mij alleen maar ook van vele studenten, stageaires, afstudeerders, collega's en vrienden. Ik wil dan ook in een persoonlijk woordje graag iedereen bedanken voor hun bijdrage en enthousiasme wat mij aan de gang hield en wat uiteindelijk geresulteerd heeft in het voltooiën van dit proefschrift. In het kort wil ik toch even schetsen hoe dit manuscript ontstaan is en wat de bijdragen van verschillende personen is geweest.

Mijn interesse in de ionenverstrooiing is eigenlijk al ontstaan in mijn studieperiode aan de TU in Eindhoven. In mijn vierde jaar heb ik dankzij Hidde Brongersma een stageplaats aangeboden gekregen op Cornell University NY. De fax die ik in handen kreeg van hem was zoets als "Your student is welcome and can arrive next Monday, greetings Jim Mayer". Kort maar duidelijk. Nadat ik enkele tentamens had gedaan dus snel in het vliegtuig, op naar New York. In de groep van professor James Mayer heb ik daar een geweldige tijd gehad waarin ik in vier maanden enorm veel heb opgestoken. Samen met de studenten Robert Dunlap en Sheryl Geimer heb ik daar met behulp van ionenverstrooiing de samenstelling en echtheid van Griekse Drachmens onderzocht. Bij terugkomst in Nederland wist ik dat dit gebied mij wel lag en weldra ben ik toen ook gaan afstuderen in de groep van professor Martien de Voigt. Ik kan wel zeggen dat mijn directe begeleider Herbert Rijken in die tijd een goed voorbeeld voor mij is geweest en de onderzoeker in mij heeft aangewakkerd. Tijdens mijn afstudeerperiode werd er al hard gewerkt aan een nieuw te bouwen opstelling waar channeling experimenten zouden kunnen worden uitgevoerd. Hoite Tolsma, Rob Bergman, Peter Mutsaers en Frans Munnik hadden daar al de hand in het opstellen van een eisenpakket voor de te realiseren opstelling. De Centrale Technische werkplaats van de TUE heeft, onder de bezielende leiding van Peer Brinkgreve, een geweldig stukje vakmanschap neergezet in de vorm van een 3-assige goniometer, die eigenlijk het hart vormt van de huidige channeling opstelling. De fijnmechanicawerkplaats heeft een knap staaltje werk geleverd. Tijdens de installatie zijn de puntjes op de i gezet door Mijndert Janszen. Toen ikzelf aangaf dat ik dat wel een heel interessant project vond om te gaan doen was ik toch blij verrast dat Martien eens met mij wilde 'babbelen'. Vervolgens ben ik als een speer aan het werk gegaan om af te studeren en de dag na mijn afstuderen meteen begonnen met het opbouwen van de nieuwe channeling-opstelling hetgeen uiteindelijk geresulteerd heeft in realisatie en

metingen die gepresenteerd zijn in dit proefschrift.

Veel hands-on hulp heb ik in de beginperiode gekregen van Henk Heller. We hebben samen dat bundelgeleidingssysteem netjes uitgelijnd, hetgeen een vereiste is om nog enige bundel achterin de opstelling over te houden. Hoewel ik de PLC-electronica nagenoeg helemaal zelf heb aangelegd moet ik toch 'Flits' Frits van Hirtum en Janus Castelijns bedanken voor hun adviezen en hulp. Ad Kemper en Jack Graus, bedankt voor het uitdenken en bouwen van de gecompliceerde electronica waarmee de goniometer nu feilloos wordt aangestuurd. Dan natuurlijk Rinus Queens bedankt dat jij altijd muziek kreeg uit het cyclotron, ook als het mij niet 1-2-3 lukte. Ook de hele bedrijfsgroep, Jan, Erik, Gerrie, Ad, Wim, bedankt dat ik altijd kon werken in een lollige sfeer, ook als de beursberichten eens een keer minder waren.

Vanaf het moment dat de opstelling werkte is het snel gegaan. Martien, de eerste metingen met een flesje wijn en een sigaar erbij zal ik nooit vergeten. Gedurende mijn hele promotieperiode heb ik veel geleerd van Leo van IJzendoorn. Ik waardeer het erg dat je altijd zo zorgvuldig bent geweest en dat ook hebt vol gehouden tot mijn proefschrift af was. Wat betreft de Monte-Carlo simulaties heb ik veel hulp gehad van afstudeerder Maurice de Koning, met recht 'The KING of LAROSE'. Ook Olaf Surewaard wil ik bedanken voor de gedrevenheid waarmee hij zijn afstudeeropdracht heeft voltooid. Het denk- en programmeerwerk met betrekking tot de aansturing van de goniometer is vakkundig gebeurd door afstudeerder Laurens van Beurden. Stageaires Thomas Schenk, Sjef Tempelaars, Ruud van Eeghem en Michiel Schok bedankt voor de prettige samenwerking. Wim Verseijden wil ik via deze weg bedanken voor het verhelpen van alle computerproblemen voor zover die mogelijkheid binnen zijn bereik lag. Speciaal wil ik collega Jos Maas bedanken voor de leerzame en gezellige tijden in Eindhoven maar vooral ook op de door Shell en NWO mede-gefinancierde buitenlandse studiereizen waar mede onder bezielende leiding van (inmiddels Dr.) Nuno Barradas veel bestudeerd werd. Jos, succes met het afronden van je promotie. Zonder direkt namen te noemen wil ik ook alle overige Aio's, studenten, medewerkers van Amersham-Cygné en mede-cyclotronbewoners bedanken voor de gemoedelijke sfeer waaronder ik mijn werk heb kunnen doen.

Zelf heb ik het laatste jaar erg veel profijt gehad van het strakke werkritme waarmee ik door Paulien ben geconfronteerd. Bedankt sch@. Tot slot wil ik ook mijn ouders en vrienden bedanken die altijd klaar stonden als ik even stoom af moest blazen of lekker *socializen*. Die afwisseling was voor mij echt noodzakelijk. Allemaal veel plezier bij het lezen van dit boekje.....

## **Curriculum Vitae**

Paul van Dijk werd geboren op 24 januari 1968 in Tilburg. Na het behalen van het VWO diploma aan de Katholieke Scholengemeenschap in Etten-Leur is hij in 1986 begonnen aan de studie Technische Natuurkunde aan de Technische Universiteit te Eindhoven. Tijdens zijn afstudeerproject in de groep van prof.dr. M.J.A. de Voigt onderzocht hij de toepasbaarheid van de coincidente elastische verstrooiingstechniek bij de diepteprofilering van lichte elementen zoals koolstof, stikstof en zuurstof. Het in kaart brengen van de individuele bijdragen, die de te behalen diepteresolutie beperken, was hierbij van groot belang. Nadat hij zijn doctoraal diploma behaalde op 19 februari 1992 is hij als assistent in opleiding in dienst getreden bij de technische universiteit. Binnen de vakgroep van professor de Voigt verrichtte hij, onder leiding van zijn co-promotor Dr. L.J. van IJendoorn, zijn onderzoek naar de toepasbaarheid van hoog-energetische ionenverstrooiing in combinatie met ionen channeling. De belangrijkste resultaten van dit onderzoek zijn beschreven in dit proefschrift.

# Stellingen

behorende bij het proefschrift

**A High-Energy Ion Channeling Facility and its Applications**

door

**Paulus Wilhelmus Leonardus van Dijk**

3 februari 1997

1. Ondanks de beperkte helderheid van het Eindhovense AVF cyclotron is het toch goed mogelijk om ionenverstrooiingsexperimenten in combinatie met channeling uit te voeren wanneer gebruik wordt gemaakt van ionen die versneld zijn door dit cyclotron. (Dit proefschrift)
2. Het gebruik van hoog-energetische helium ionen ( $> 10$  MeV) maakt het mogelijk de roostervorming van epitaxiale lagen met een hogere nauwkeurigheid te bepalen dan met het gebruik van laag-energetische ionen mogelijk is. (Dit proefschrift hoofdstuk 4)
3. Het gebruik van 6 MeV-heliumionen maakt diepteprofilering en kwantificatie van roosterdefecten mogelijk in een kristallijne  $\text{Si}_{1-x}\text{Ge}_x$  laag tot op een diepte van 4 micrometer. (Dit proefschrift hoofdstuk 5)
4. Gebruikmakend van de combinatie van ionenverstrooiing en nucleaire reactieanalyse kan een uitspraak gedaan worden over de waarde van de vibratie-amplitudes van indium en fosfor atomen in een diatomair InP-kristal. (Dit proefschrift hoofdstuk 6)
5. Het ontmantelen van een kernreactor is in het algemeen sterk af te raden.

6. Het is niet ondenkbaar dat het gebruik van hoog-energetische ionen ten behoeve van materiaalanalyse na het verschijnen van dit proefschrift vaker zal gaan plaatsvinden.
  
7. Het gebruik van synchrotronstraling, om het interstellaire stralingsveld te simuleren, kan nuttig zijn om een beter inzicht te krijgen in de fotochemie in interstellaire stofmantels.
  
8. Het is opmerkelijk dat bij het gebruik van de woorden *ionisch* en *dorisch* zelden aan muziek wordt gedacht, terwijl deze termen als aanduiding voor toonsoorten reeds vanaf de middeleeuwen gebruikt worden.
  
9. Dankzij het fiscale stelsel in Nederland en de door de Partij van de Arbeid geïnitieerde uitbreiding van de spaarmogelijkheden voor werknemers, kan sinds 1 januari 1994 een werknemer met een topinkomen netto geld toe krijgen als hij/zij een lijfrente afsluit terwijl een werknemer met een modaal inkomen netto geld moet betalen.
  
10. Bij het stimuleren van de belangstelling voor de natuurkunde bij VWO leerlingen kan het interactieve 'Natuurkunde Circus' een belangrijke rol spelen.